Doctoral Thesis

Study of the Characteristics of Magnetic Field in the Flaring Active Regions Based on the Nonlinear Force-Free Field Extrapolation and Magnetohydrodynamic Simulations

(非線形フォースフリー磁場外挿法と電磁流体力学

シミュレーションに基づいた、

太陽フレアを引き起こす活動領域磁場の研究)

By:

Johan Muhamad

Supervisor:
Prof. Kanya Kusano

Nagoya University

February 2019

Abstract

Solar flares release magnetic energy stored in the active regions (ARs) of the Sun to the interplanetary space by means of the magnetohydrodynamic (MHD) instabilities and magnetic reconnection in the solar corona. Although the basic morphological structure of solar flares has been well explained by the standard flare model, what kind of ARs can produce large solar flare is still unclear. The characteristics of the flaring AR are the crucial problems to understand the mechanism of solar flares. This is strongly related to the flare triggering process and the instability of the magnetic field in the AR. Therefore, studying these two fundamental processes is very important to improve our understanding about the onset mechanism of solar flares. Numerical simulations by Kusano et al. (2012) revealed that two small emerging magnetic structures, which are opposite polarity (OP) and reversed shear (RS) structure, are effective to trigger solar flares. Although simulation by Kusano et al. (2012) is very important and useful to understand the basic properties of flare trigger structures, the result of the simulations needs to be examined for more realistic magnetic field. On the other hand, Ishiguro and Kusano (2017) recently investigated the instability of the double-arc magnetic structure, which can be formed by the tether cutting reconnection. They proposed κ parameter that can represent the critical condition for the double-arc instability (DAI) to occur. However, this κ parameter has never been investigated for the real flare event in the Sun. In this study, we focus on investigating the feasibilities of applying the triggering mechanism proposed in the numerical simulations by Kusano et al. (2012) and the theory of the DAI by Ishiguro and Kusano (2017) for the real observational data. We employed magnetic relaxation method by Inoue et al. (2014b) to extrapolate coronal magnetic field as a non-linear force-free field (NLFFF). We investigated the possible mechanism that can trigger a solar flare through the modeling of an AR and parametric ensemble

simulations based on the data observed by Hinode satellite. From our simulations, we found that the trigger scenarios proposed by Kusano et al. (2012) could also work on more realistic magnetic field derived from the observational data to drive a flare. This was confirmed by the similarities of the synthetic flare ribbon created in the simulation and the observed one. Moreover, we proposed the new parameter κ^* as a proxy of κ, and we applied it on real ARs. As the result of the analysis, we found that κ^* evolutions of the flaring ARs were consistent with the critical instability condition derived in the DAI theory. Our result suggests that solar flare can occur when the amount of reconnected flux that increases the number of highly twisted field lines becomes large enough compared to the total flux within the core of the AR. These results show that the NLFFF extrapolation constructed from the photospheric magnetic field data significantly works to help our understanding of the process that determines the onset of a flare. Proper parameters derived from NLFFF can be useful to evaluate the possibility of the upcoming flare. We suggest that the use of κ^* and additional information of trigger structure in the AR can be beneficial for the better solar flare forecasting.

Acknowledgements

"*Innal Hamda Lillah...*"

I would extend my sincerest gratitude to my supervisor, Prof. Kanya Kusano, for his supervision, encouragement, help, and support during my study and life in Japan. His dedication and vision always motivate me to do better research and complete my study in Nagoya University.

I am also very grateful to my collaborators Dr. Satoshi Inoue, Dr. Daikou Shiota, Dr. Yumi Bamba for fruitful comments, discussions, and supports that improved my research. I thank to Assoc. Prof. Satoshi Masuda, Dr. Shinsuke Imada, Dr. Sung-Hong Park, and Dr. Takuma Matsumoto for their supports and helps during my research and study in Nagoya University. I would like to thank Dr. Bernhard Kliem and Dr. K.D. Leka for their valuable comments that improved the manuscript for the publications. I thank to all my fellow doctoral students, especially Takuya Shibayama and Naoyuki Ishiguro for the discussions and help during my study. I thank to all my fellow students in ISEE for the valuable moments and supports as a student. I also thank to all secretaries in Integrated Studies group in ISEE, especially Ms. Motoko Kunieda who help me a lot for the administrative works during my study. I also thank to Ms. Tae Torii in ISEE office for her help in managing academic procedures and paperworks during my study.

I would like to acknowledge Indonesian Endowment Fund for Education (LPDP) for giving scholarship and other financial supports during my doctoral course in Nagoya University. Part of the work in this thesis was supported by JSPS/MEXT KAKENHI Grant Nos. 23340045 and 15H05- 814, and MEXT/JSPS KAKENHI Grant Numbers JP15H05814, and by MEXT as "Exploratory Challenge on Post-K Computer" (Environmental Variations of Planets in the Solar System).

I would like to express my gratitude to my home institute, Indonesian National Institute of Aeronautics and Space (LAPAN), especially to Prof. Thomas Djamaluddin and Ms. Clara Yatini who gave me permission and supports for my study in Japan. I also thank to all my fellow colleagues in LAPAN, especially X-Matsa team for their help in LAPAN.

Finally, I would like to express my sincere gratitude to my parents and brothers in Indonesia for all their continous love and supports. I am very grateful to my beloved wife, Mila, and my wonderful son, Naja, who always be my great inspiration and encourage me through all situations. I thank to all my friends and families in Japan and Indonesia whom I cannot mention all their names here for their helps and supports so that I can finish my study.

Contents

List of Figures

List of Tables

Abbreviations

AR	**A**ctive **R**egion
AIA	**A**tmospheric **I**maging **A**ssembly
CME	**C**oronal **M**ass **E**jection
HMI	**H**elioseismic and **M**agnetic **I**mager
LFFF	**L**inear **F**orce **F**ree **F**ield
MHD	**M**agnetoydrodynamics
NLFFF	**N**on-Linear **F**orce **F**ree **F**ield
PIL	**P**olarity **I**nversion **L**ine
SDO	**S**olar **D**ynamics **O**bservatory
SHARP	**S**paceweather **H**MI **A**ctive **R**egion **P**atch
SOT	**S**olar **O**ptical **T**elescope
SP	**S**pectropolarimeter
XRT	**X**-ray **T**elescope

Chapter 1

Introduction

The Sun is the primary star and the center of gravity of our solar system. In addition to that, the Sun is also the main energy source in our life on the Earth. Apart from the energy that we can consume to support our life, the Sun can also release large amount of energy that may have severe impacts to our society. Observations of the Sun using advanced multi-instruments for decades have revealed that huge amount of energy released from the Sun through solar flares and coronal mass ejections (CMEs). Although a lot of progress have been achieved in our understanding of solar flares, there are several issues that are still unclear about solar flares that we need to clarify. Before going into the more detail discussion of solar flare problems, it is important to review the basic and general knowledge of solar flares.

In this chapter, we present the overview of solar flares and the standard solar flare model. We also present some general concepts of solar magnetic field and several theories of solar eruption. We briefly discuss the basic idea of the trigger mechanism proposed by Kusano et al. (2012) and the double-arc instability theory by Ishiguro and Kusano (2017) as the main subjects in this thesis. Finally, we address the main problem and the main objective of this thesis.

1.1 Solar Flare

Solar flare is a sudden enhancement of wide electromagnetic (EM) spectrum emission from the Sun as a result of release of magnetic energy. The estimated energy released from a solar flare can vary from 10^{28} – 10^{32} erg and can possibly reach 10^{33} erg for the largest event (Shibata and Magara, 2011; Aulanier et al., 2013). Apart from the intense emission of EM wave from radio wave to gamma rays, particles such as protons and electrons are also accelerated and emitted from the Sun to the interplanetary space. The accelerated particles can interact with the magnetic field of planets and affect the condition of magnetosphere and ionosphere of the planets. Huge energy released in the form of rapid increase of radiation and acceleration of particles from a flare can disturb space environment and solar system in general. Large solar flare events can disrupt space technology systems such as satellites, spacecrafts, satellite-based navigation systems, and endanger astronaut life in space. The solar system environment and interplanetary space affected by the activities in the Sun such as solar flare is known as space weather.

Solar flare was first reported by Carrington (1859) and Hodgson (1859), who observed the rapid burst of white-light emission from the region of sunspot in September 1st, 1859. Since then, solar flares have been reported to be observed in almost entire EM spectrum. It is commonly accepted now to classify the solar flare size based on the peak of its soft X-rays (SXR) flux at 1-8 Å observed by the Geostationary Orbiting Environmental Satellites (GOES). The classification of the flare based on this GOES SXR observation is shown on table 1.1. Statistical studies of the temporal aspects of flares revealed that the duration of flares in SXR are varied in the order of 10^2 – 10^3 s with the median of about 10, 12, 24, and 30 minutes for B, C, M, and X, class flares, respectively (Veronig et al., 2002). Although most of the flares are observed coming from active regions, where magnetic field are relatively strong to the surrounding area, there are also some flares observed in the "spotless" region (Altas, 1994) or from the quiescent filament eruptions (e.g. Jing et al. (1994)).

TABLE 1.1: Classification of solar flares based on the GOES SXR flux 1-8 Å.

Class	**Peak Flux** (erg $cm^{-2}s^{-1}$)	**Peak Flux** (W m^{-2})
X10	10^{0}	10^{-3}
X	10^{-1}	10^{-4}
M	10^{-2}	10^{-5}
C	10^{-3}	10^{-6}
B	10^{-4}	10^{-7}
A	10^{-5}	10^{-8}

During flare process, several phases have been defined corresponding to the characteristics of the flare intensities as its function of time. These phases are preflare or precursor phase, impulsive phase, and decay phase (Benz, 2008). The schematic profiles of flare intensities in multi wavelength observations are shown in figure 1.1. During the preflare phase, the coronal plasma slowly heats up and becomes visible in SXR and extreme ultra violet (EUV). In the impulsive phase, large amount of electrons and ions are accelerated. This is the main phase of flare when most of the energy is released. The decay phase happens when lower part of coronal plasma returns almost to the initial state. In the typical flare, preflare phase last for several minutes, impulsive phase to about 10 minutes, and decay phase can last for an hour or more (Benz, 2008).

Since Hale first measured the magnetic field in sunspot in 1908 (Hale, 1908), it became apparent that magnetic field has important role in sunspot or active region dynamics. From the simple energy estimation, it can be estimated that it is only magnetic energy in the Sun that can sufficiently supply the energy required for a flare, while thermal energy will not be sufficient (Warwick, 1962). This leads to the further problem regarding the mechanism to convert the magnetic energy to the thermal and kinetic energy that released during a flare. The most possible mechanism that can explain the energy conversion of magnetic energy to the thermal and kinetic energy is magnetic reconnection (Gold and Hoyle, 1960; Parker, 1963).

Magnetic reconnection happens when two regions of plasma containing oppositely

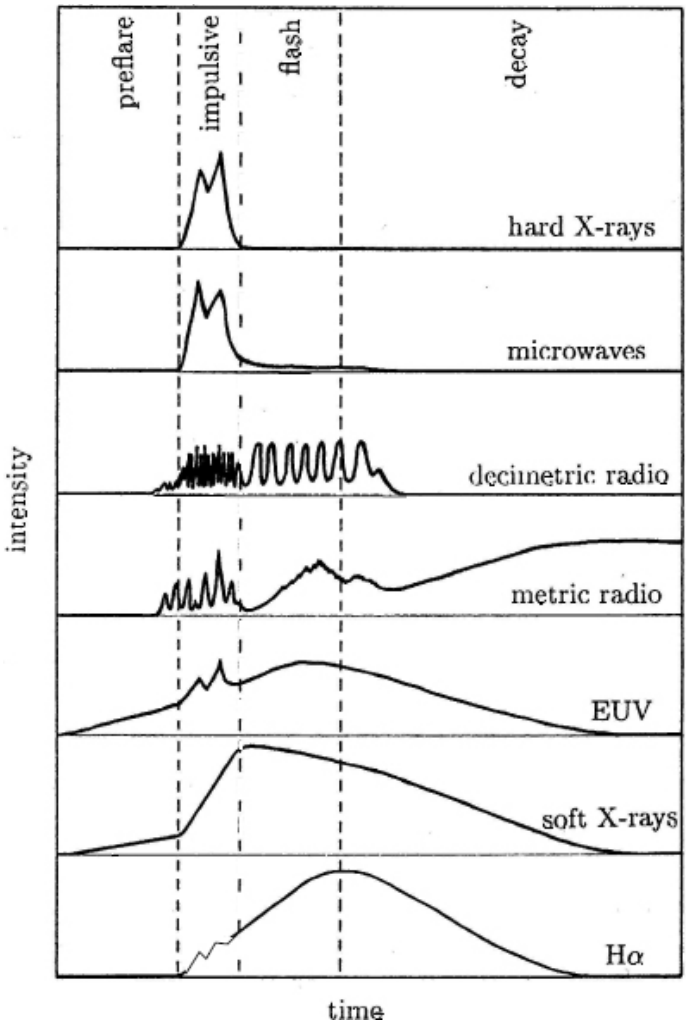

FIGURE 1.1: Schematic diagram of flare intensities as a function of time and flare phases (reprinted from Benz (2008)).

directed magnetic fields are placed in contact and reconnect in a tiny diffusion region where the two magnetic fields annihilate by electric current dissipation and convert the magnetic energy to other forms. The schematic diagram of magnetic reconnection is shown in figure 1.2. In the magnetic reconnection process, plasma that coming into the diffusion region with speed v_i will come out from the diffusion region with different speed, v_A, which is the Alfven speed in the inflow region. The reconnection rate is defined as the Alfven Mach number of the inflow region, $M_A = v_i/v_A$. In the diffusion region, intensive current flows due to a finite resistivity that causes Ohmic dissipation and creates a current sheet. If the length of the current sheet is L, and

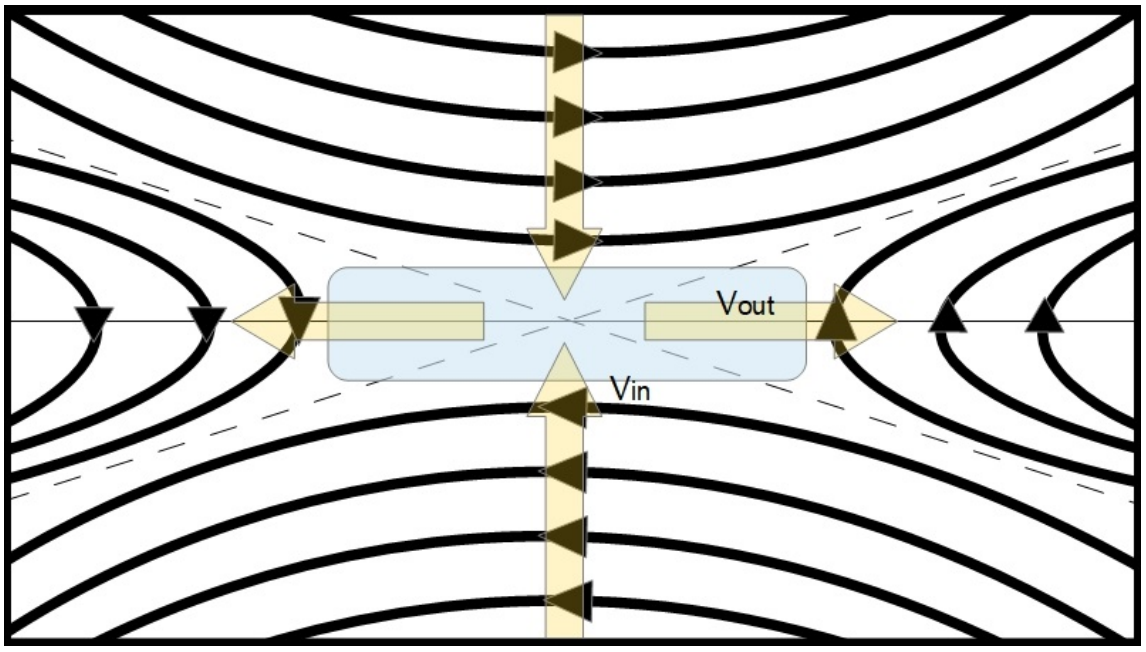

FIGURE 1.2: Schematic diagram of magnetic reconnection.

the Alfven transit time, $t_A = L/v_A$, then we can define reconnection time,

$$t_r = \frac{L}{v_i} = \frac{t_A}{M_A}, \tag{1.1}$$

Typical Alfven transit time, Alfven speed, and magnetic Reynolds number ($R_m = v_A L/\eta$) in the corona is something between 10 to 100 s, 1000 km/s, and 10^{14}, respectively (Shibata and Magara, 2011). As a consequence of magnetic reconnection, magnetic topology in the outflow region should differ from the inflow region. Therefore, magnetic reconnection that happens in the corona should change the coronal magnetic structure before and after the reconnection. Some of the coronal structure that have been inferred as evidences of magnetic reconnection are cusp-shaped structure (Tsuneta et al., 1992), current sheet (Sui et al., 2004), plasma flows (Lui et al., 2013; Yokoyama et al., 2001), and plasmoid ejection (Shibata et al., 1995). Some evidences from Yohkoh (e.g.Tsuneta (1996); Masuda et al. (1994)), RHESSI (Sui et al., 2004; Su et al., 2013), and Solar Dynamics Observatory (SDO) (Su et al.,

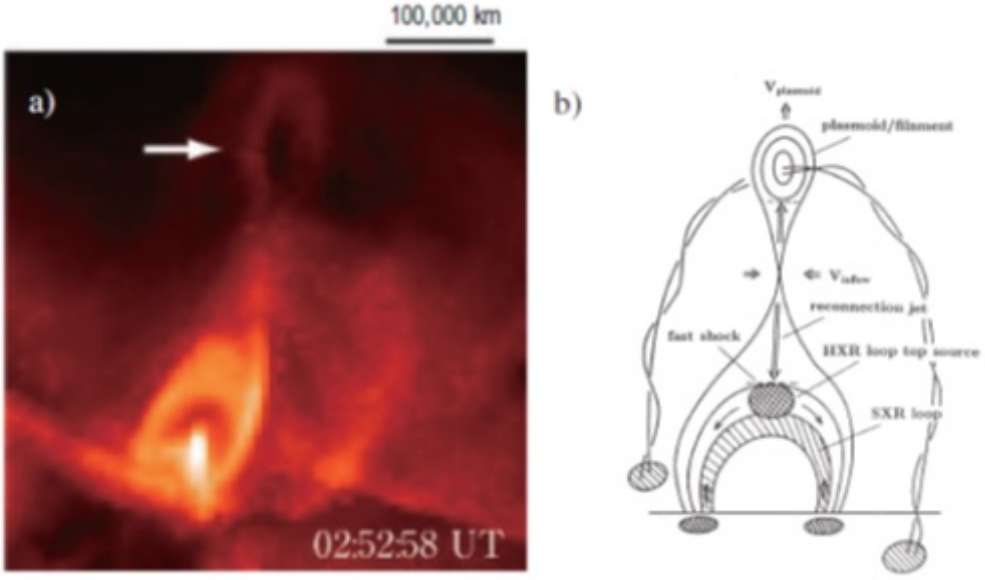

FIGURE 1.3: Solar flare observed by Yohkoh satellite and the corresponding schematic of the modified CSHKP model (reprinted from Shibata and Magara (2011)). White arrow shows the location of plasmoid.

2013; Yan et al., 2018) observations proved that magnetic reconnection really took place when flares happened.

1.2 Solar Flare Model

What appears to be the standard flare model today is the concept of magnetic field configuration, reconnection, and physical processes that happen during a flare, which was developed by some main contributors of the model (Carmichael, 1964; Sturrock, 1966; Hirayama, 1974; Kopp and Pneuman, 1976), or known as "CSHKP model". In this model, flares happen due to a reconnection of magnetic field in the corona that will lead to the formation of post flare loop below the reconnection point and a plasmoid on top of it. This reconnection will heat the plasma and accelerate electrons and ions along the magnetic loop to the thermal and non-thermal energy range.

Some of the electrons in the magnetic loop will emit SXR through the free-free (Brehmstrahlung) emission, and may also propagate to the dense chromosphere and heat the materials there (Benz, 2008). Hard X-ray (HXR) emission, therefore, can be observed from the location of the footpoint of the loop, where high energy particles interact with high density materials in the chromosphere. Strong emissions from H-α and various wavelengths (UV and EUV) also appear in the footpoint of the loop, particularly during the main impulsive phase of the flare. Unlike the HXR emission that is usually compact in a limited footpoint location, H-α and EUV emissions are usually extended to the more distance footpoint locations creating what is known as flare ribbon (Fletcher et al., 2011). Loop-top or coronal HXR sources were also observed in several flares, e.g. Masuda et al. (1994), which suggested that there was an indication of the presence of thick target in the corona (Wheatland and Melrose, 1995). The schematic solar flare model and the comparison with the observed flare is shown in figure 1.3.

Solar flare model has been developed in the more complex 3-D configuration (Priest and Forbes, 2002) as it is shown in figure 1.4. Post-flare loop then can be viewed as a series of loops making the post-flare arcade, where on the top of it a reconnection point is elongated in the lateral direction. The plasmoid can now be viewed as a flux rope, where strong twist magnetic field lines with same axis are formed. This flux rope can also help us to infer the existence and location of a filament that usually lies in the lower part of the flux rope. It can be generally said that the shape of the magnetic arcade and flux rope follow the polarity inversion line (PIL), where two different magnetic polarities dramatically change. Moreover, since the location and shape of flare ribbon mark the footpoint locations of the magnetic arcade, morphology of the ribbon becomes more important in the 3-D framework to indicate the signature of the coronal magnetic structure in an AR. This property can be useful in the analysis of the magnetic field of flaring AR as we show in this thesis.

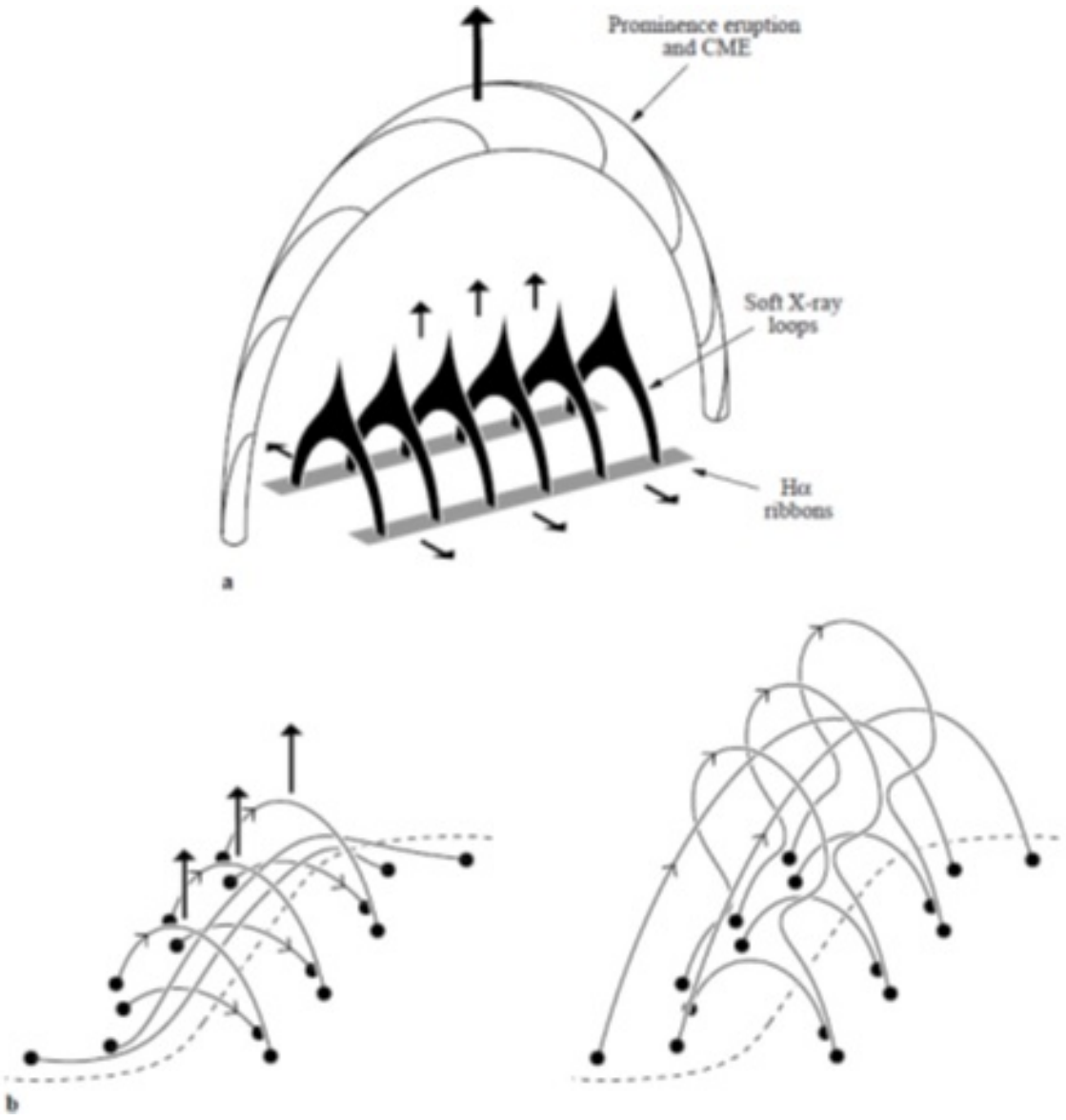

FIGURE 1.4: 3-D solar flare model (reprinted from Priest and Forbes (2002)).

1.3 Solar Force-Free Magnetic Field

As it has been mentioned before, magnetic field plays important role in the flare process since magnetic energy is the main contributor of the energy source in a solar flare. Moreover, energy conversion via magnetic reconnection depends on the configuration of magnetic structure in the AR and the topology of field lines involved in the reconnection process. Therefore, understanding magnetic field of the Sun,

particularly in the AR prior to a flare is crucial to reveal the mechanism and the precursor of flares. To accurately study the magnetic field of an AR, one should analyze the magnetic field on the photosphere, chromosphere, corona, or even in the subsurface region. However, since a flare releases magnetic energy from the corona, it is useful to emphasize the study of coronal magnetic field in order to understand the stability of the magnetic structure that will eventually produce a flare. Unfortunately, coronal magnetic field cannot be directly observed by the present technology. Therefore, we need to find a way to infer magnetic field in the corona, mostly by the information we obtained from the photosphere.

Solar magnetic field in an AR can be assumed to be in an equilibrium state before the onset of a flare. This equilibrium state can be achieved when the net force acting on the field is zero. In the ideal coronal environment, since we can assume that plasma pressure is infinitesimal compared to magnetic pressure and gravity is neglected, the equilibrium can be achieved simply by the condition that the Lorentz force in the system is zero. One parameter that is useful to represent the ratio of plasma pressure and magnetic pressure in a plasma is the plasma beta (β), which is defined as:

$$\beta = 2\mu_0 \frac{p}{B^2}. \tag{1.2}$$

Here, p is the plasma pressure, B is the magnetic flux density, and μ_0 is the permeability of vacuum. In the environment where $\beta = 0$, one can consider that only magnetic field plays a role in the plasma motion. Plasma-beta in the solar corona is considered to be very small $\beta << 1$, while in the chromosphere it is in the order of unity, and even higher in the photosphere (Gary, 2001). Figure 1.5 shows the estimation of plasma beta in the Sun for different heights. Due to the condition of small plasma beta in the corona, the zero-beta approach can be used to easily understand the coronal magnetic field dynamics before and after a flare.

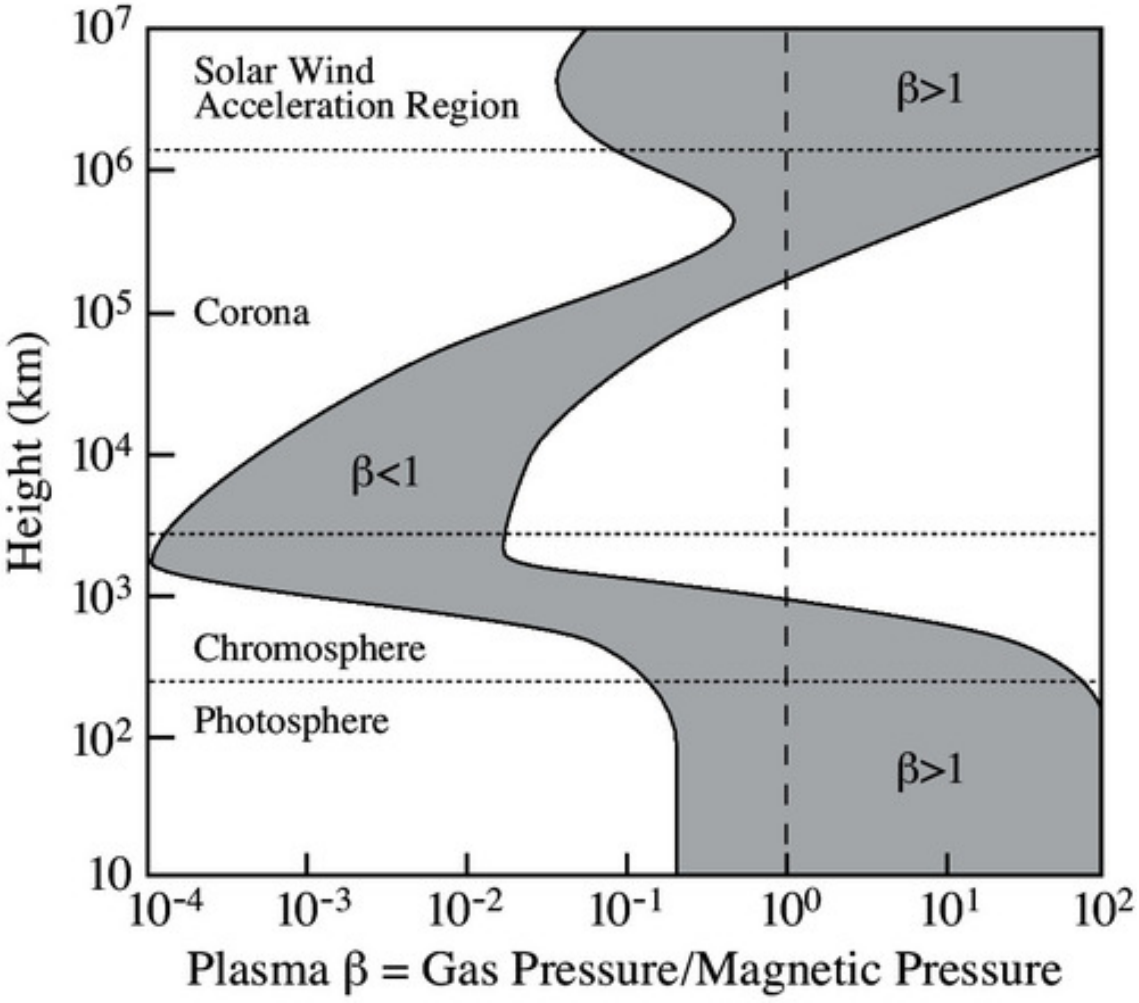

FIGURE 1.5: Plasma beta as a function of height above the photopshere (reprinted from Gary (2001)).

In the zero plasma beta environment, if the Lorentz force vanishes,

$$\boldsymbol{J} \times \boldsymbol{B} = 0, \tag{1.3}$$

where the current density $\boldsymbol{J} = \frac{\boldsymbol{\nabla} \times \boldsymbol{B}}{\mu_0}$, then

$$(\boldsymbol{\nabla} \times \boldsymbol{B}) \times \boldsymbol{B} = 0. \tag{1.4}$$

The equation 1.3 can be satisfied if the current is zero, $\boldsymbol{J} = 0$, or $\boldsymbol{J} || \boldsymbol{B}$.

The former solution is called as potential field or current-free field solution. This solution can be solved analytically by using Green function (Sakurai, 1982) or Fourier method (Alissandrakis, 1981). Potential field is the simplest approach to model the corona. By using vertical component of photospheric vector magnetogram data, one can extrapolate the potential field. However, since potential field does not fit the observational form of the corona seen from the EUV and X-ray emissions, potential field can only give coarse view of the coronal field.

The latter solution implies that

$$\boldsymbol{\nabla} \times \boldsymbol{B} = \alpha \boldsymbol{B}, \tag{1.5}$$

where α is a scalar function so called force-free parameter. Note when α is zero then it implies that the current is also zero, which means this condition is the same as potential field.

Taking the divergence to equation 1.5 and using the vector identity to the left hand side term

$$\boldsymbol{\nabla} \cdot (\boldsymbol{\nabla} \times \boldsymbol{B}) = 0, \tag{1.6}$$

then the right hand side will give

$$\boldsymbol{\nabla} \cdot (\alpha \boldsymbol{B}) = 0, \tag{1.7}$$

$$\alpha \boldsymbol{\nabla} \cdot \boldsymbol{B} + \boldsymbol{B} \cdot \nabla \alpha = 0, \tag{1.8}$$

$$\boldsymbol{B} \cdot \nabla \alpha = 0, \tag{1.9}$$

due to the solenoidal condition $\boldsymbol{\nabla} \cdot \boldsymbol{B} = 0$. Equation 1.9 infers that α should be constant along the field line.

Taking the curl to equation 1.5 we will have

$$\boldsymbol{\nabla} \times (\boldsymbol{\nabla} \times \boldsymbol{B}) = \boldsymbol{\nabla} \times (\alpha \boldsymbol{B}). \tag{1.10}$$

If α is constant everywhere, then equation 1.10 will be

$$\nabla(\boldsymbol{\nabla} \cdot \boldsymbol{B}) - \boldsymbol{\nabla}^2 \boldsymbol{B} = \alpha \boldsymbol{\nabla} \times \boldsymbol{B}. \tag{1.11}$$

By considering the solenoidal condition and equation 1.5, then equation 1.11 becomes

$$-\boldsymbol{\nabla}^2 \boldsymbol{B} = \alpha^2 \boldsymbol{B}. \tag{1.12}$$

This solution, in which α is constant everywhere in the calculation domain, is called the linear force-free field (LFFF). This can also be solved by using Green function (Chiu and Hilton, 1977) and the Fourier method (Alissandrakis, 1981) as it is reviewed by Wiegelmann and Sakurai (2012).

If the force-free parameter α is not constant, but is a function of position, then equation 1.10 will give us

$$\boldsymbol{\nabla}^2 \boldsymbol{B} + \alpha^2 \boldsymbol{B} = \boldsymbol{B} \times \nabla \alpha, \tag{1.13}$$

due to the solenoidal condition. This case is called as non-linear force-free field (NLFFF) that α changes as a function of its position, but remains constant along the field line.

1.4 Nonlinear Force-Free Field

When the same boundary condition is given, the potential field, LFFF, and NLFFF will produce different topological structure of coronal field. It is easy to find that among different solutions of force-free field that have been described earlier, NLFFF provides the closest topological agreement with observations since it can reproduce even complex structure. The magnetic energy comparison of the system can also be used to determine which solution is more reasonable to model the coronal field.

Theoretically, potential field provides the lowest energy state among the solutions (Sakurai, 1989). Free energy, which is the excess between the total energy and the potential field energy that can be released in a flare, can be calculated by subtracting the LFFF or NLFFF magnetic energy with the potential magnetic energy. From the aspect of topology of magnetic field, NLFFF is more preferable to model coronal magnetic field than potential field and LFFF. However, due to the non-linearity of the NLFFF equation in 1.9, the analytical solution for this problem cannot be solved in most cases. Fortunately, however, there are several numerical methods to solve NLFFF problem by given photospheric magnetogram data as the boundary condition. Reviews of various NLFFF methods can be viewed in the papers by Wiegelmann and Sakurai (2012) and Inoue (2016). In the following paragraphs, we briefly introduce the several NLFFF methods that have been developed.

One of the first method to extrapolate the NLFFF of the solar corona is the upward integration method (Nakagawa, 1974). In this method, coronal magnetic field is directly integrated from the the bottom boundary by the force-free α information obtained in the photosphere. Once the α is obtained, horizontal components of the current density in the photosphere are calculated, and then finally magnetic field is vertically integrated to obtain the 3-D coronal field (Wu et al., 1989). This method has been found to be mathematically ill-posed and unstable due to the possibility of the exponential growth of magnetic field during the integration (Wiegelmann and Sakurai, 2012). Another famous method to solve NLFFF is the Grad-Rubin method. Sakurai (1981) was the first in applying the Grad-Rubin technique to extrapolate coronal field before it was later developed by Amari et al. (1997), Wheatland and Régnier (2009), and Gilchrist and Wheatland (2012). In this method, potential field is extrapolated from the vertical component of the magnetic field in the solar surface (i.e. bottom boundary). The force-free alpha in the surface is then measured by $\alpha = J_z/B_z$. The α is then distributed from one polarity on the photosphere following the field line using equation 1.9. Therefore, this method requires only α from one polarity, whether it is positive or negative. The magnetic field is then

updated by solving:

$$\boldsymbol{\nabla} \times \boldsymbol{B}^{k+1} = \alpha^k \boldsymbol{B}^k, \tag{1.14}$$

where k is the iteration number, until the magnetic field does not change. This method can give a solution for NLFFF as a well-posed boundary value problem. However, it is often that the solution derived from one polarity can be different from another polarity. The solution of NLFFF is also sometimes does not well match with the coronal field inferred from the optical observation.

Another way, which is widely used, to find the solution of the NLFFF is by relaxing the unstable magnetic field towards the stable state with the constraint of maintaining the boundary conditions to be consistent with the observations. Usually, this kind of method solves MHD (or MHD-like) equations for the zero-beta condition during the relaxation time. The initial condition is set from the potential field calculated from the vertical component of magnetogram data in the photosphere. The bottom boundary for the horizontal component is then adjusted to be consistent with the observations and finally the magnetic field relaxes to the stable state. Several methods have been developed to solve the NLFFF for this relaxation. Mikić and McClymont (1994) applied voltages on the bottom boundary to drive currents to the corona until it reaches the desired current density by solving resistive MHD equations. Inoue et al. (2014b) solved resistive MHD-like equations with simplified plasma density and applied numerical correction to reduce numerical remnants in the divergence $\mathbf{B}$ that make it closer to the supposed solenoidal condition. Yang et al. (1986) and Klimchuk and Sturrock (1992) applied the method known as the "magneto-friction" in which they introduced an artificial force complementing the Lorentz force in the relaxation phase. Valori et al. (2005) later developed the magneto-friction method, which is able to produce high-twist field lines. Roumeliotis (1996) used the same technique but in such a way that the process alternate between changing the boundary condition and the relaxation until the boundary matched the observations. This alternation will make the stress and relax phases happen consecutively, so that it is known as "stress and relax" method. On the other hand,

Wheatland et al. (2000) developed an optimization method. In this method, instead of solving the induction equation directly during the relaxation process, it solves a set of equations to minimize a new function (L), which contains the Lorentz force and the divergence of magnetic field. Therefore, the NLFFF is achieved when the function L reaches a certain threshold. Wiegelmann and Inhester (2010) developed this method by adding another function that takes into account the reliability of the data.

The use of all components of photospheric vector magnetic field data in the MHD relaxation techniques carries a problem in the NLFFF extrapolation. This is because the photospheric field itself is not force-free. Therefore, applying the non force-free data for the force-free approach will result in the inconsistency with the coronal field observations. MHD relaxation solutions also usually converge to a finite Lorentz force and do not satisfy solenoidal condition. In order to verify the result of coronal modeling, comparison between the model and observations is needed. The model that has more agreement with coronal image from the observation can be considered as the more reasonable model (Wiegelmann and Sakurai, 2012). In this sense, incorporating coronal images to improve the reconstructed coronal field can be useful. The use of coronal images for reconstructing coronal field has been applied in the flux insertion method (van Ballegooijen, 2004). In this method, potential field is initially calculated from the normal component of magnetic field in the bottom boundary. Artificial current is then introduced in such a way that a flux rope is created to model observed filament by implementing magnetofriction technique. This method can be useful to reproduce a filament or sigmoid, especially in the weak field region, which is difficult to reproduce in the MHD relaxation techniques. Other methods are also developed by incorporating the magnetic field data and the topology of observed coronal loops (Aschwanden et al., 2012; Malanushenko et al., 2014).

The comparison of these numerical methods was studied extensively by Schrijver et al. (2008) and DeRosa et al. (2009, 2015). Essentially, they found that the different

methods applied for the same boundary condition do not reproduce unique NLFFF in term of the geometry, magnetic energy, and force-freeness. DeRosa et al. (2015) found that the magnetic energy calculated from almost all NLFFF extrapolation methods for a given high-resolution data converge to a certain value except the optimization method. They found that the calculation of magnetic energy from different method more converges for the smaller binning factor of the reduced vector magnetogram data. Therefore, NLFFF will generally work better to capture the coronal magnetic field energy when the full resolution of magnetogram data is used. Although NLFFF can capture the topology and connectivity in the corona, the calculated magnetic energy may not be too reliable especially when the plasma beta (β) is still in the order of the relative free-energy, which is the ratio of the excess energy compared to the total energy (Peter et al., 2015).

We will focus on the use of the MHD relaxation method by Inoue et al. (2014b) in our study for several reasons. First, the MHD relaxation method in Inoue et al. (2014b) prescribes all components (i.e. normal and tangential) of vector magnetogram data obtained in the photosphere. The use of all components of vector magnetic field data will be a very good constraint to ensure that the NLFFF is reconstructed based on the observations. The full high-resolution photospheric vector magnetic field data obtained by space-based observations is very useful for improving our understanding on the solar flare process. Second, the MHD relaxation method (Inoue et al., 2014b) has been extensively used to extrapolate coronal fields of many ARs (e.g. AR 10930, 11158, 12192, 12673, 12017) and the extrapolated coronal fields have good agreement with the observed coronal images (Inoue et al., 2011, 2013, 2014a, 2016, 2018; Woods et al., 2018). The NLFFF models reconstructed by this method have also shown to be able to reproduce high-twist coronal field or flux rope (Inoue et al., 2011, 2014a) as well as can work as a powerful tool to study the trigger process of solar flares (Inoue et al., 2015, 2018). Third, this method can be easily applied with simple treatment and limited computational resource. We will explain the detail of the MHD relaxation method used in this study in Chapter 2.

1.5 MHD Instabilities

Solar flare and solar eruption (CME) can happen in the Sun when magnetic field in the corona lose its equilibrium state. The lowest energy state of magnetic system of an AR is given by the potential field. During its lifetime, this magnetic field may grow in size in the early phase and can become more complex. The complex structure of the magnetic field configuration in the corona often appears as twisted magnetic field that forms an S-shape or inverse S-shape, which is known as sigmoid. This indicates that some free magnetic energy is stored before a flare, which can be recognized by the deviation of magnetic field configuration from the simple potential field configuration. When free magnetic energy stored in the corona is continuously accumulated due to some shearing motion in the photosphere or strongly-twist emerging flux, magnetic system can be more unstable than before. At certain point, magnetic system can experience the "loss-of -equilibrium".

The instability can be achieved mainly by two different mechanisms, which are ideal MHD instability and non-ideal (resistive) MHD instability. The term "ideal" here refers to the condition that the electric resistivity is neglected. Therefore, in this ideal condition, no dissipation process can happen. All mechanisms that can bring the magnetic system to the unstable state without any role of resistivity is classified as the ideal MHD instability mechanisms. On the other hand, in the non-ideal MHD system, the dissipation of electric current can happen due to the presence of electric resistivity. As a consequence, a non-ideal MHD instability process involves magnetic reconnection to drive the eruption. There are several flare models have been developed to explain solar eruption, which can be classified as ideal or nonideal MHD instability, based on the physical driver in the early phase of the eruption. We will explain some of them that are mainly related to our studies.

1.5.1 Non-Ideal MHD Instabilities

When the trigger of a flare is related to the dissipation process via magnetic reconnection due to the presence of electric resistivity, the mechanism is considered as the nonideal MHD instability. One of the famous resistive MHD theories explaining the trigger of a solar flare is the magnetic breakout model (Antiochos et al., 1999). In this model, magnetic reconnection happens between the low-lying magnetic arcades and the overlying field. This model requires quadrupolar field in the photosphere that forms two bipole arcades and the overlying field with same polarity, and one arcade with opposite direction located in between the two low lying arcade. The schematic cartoon for the magnetic breakout model is shown in figure 1.6. When a shear motion happens near the PIL of the low lying opposite arcade, this arcade starts to rise, overlying field weakens and reconnection happens in the null point that is located in between the low and overlying field. This will allow the low lying arcade to expand and the eruption will happen. The scenario of the magnetic breakout model can happen in the complex AR when there is an new flux that emerges within this AR (Chen et al., 2016). Because this scenario is also thought to appear in the small scale system, this model is also proposed to explain the occurrence of coronal jets (Wyper et al., 2017).

Another theory that is proposed to explain the mechanism of a solar flare or solar eruption is the tether cutting mechanism (Moore et al., 2001). If the reconnection in the magnetic breakout model happens between the sheared magnetic arcade and the external overlying arcade, the reconnection in the tether cutting model happens between the internal field lines within the sheared arcade. Figure 1.7 shows the overall scenario for the tether cutting model. Suppose there is a sheared arcade in the vicinity of the PIL. When there is some internal perturbation within this arcade, some magnetic field lines somehow can reconnect each other and create a flux rope. This flux rope will be unstable and the upward eruption can happen. A low lying arcade can occur below the reconnection points and flare ribbon can be

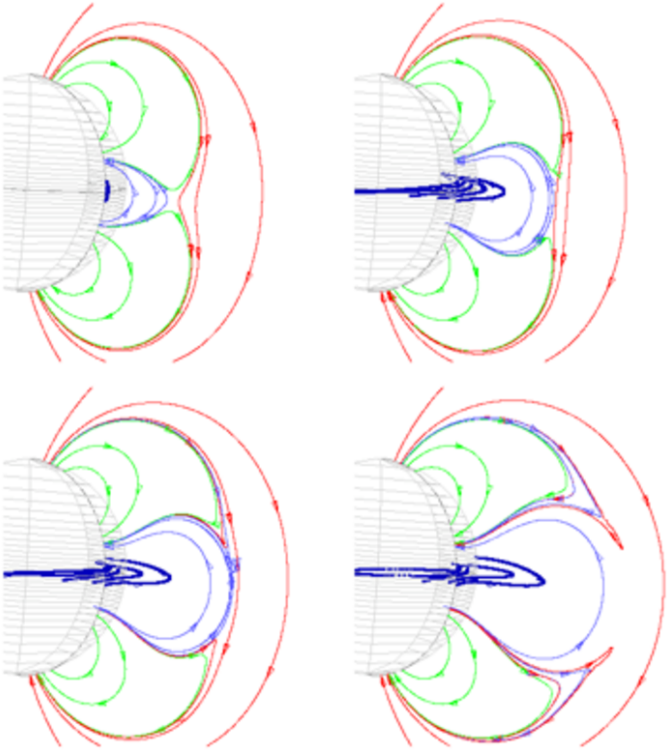

FIGURE 1.6: Schematic diagram of the magnetic breakout model (reprinted from Antiochos et al. (1999)).

observed in the footpoints of the arcade and the flux rope. This scenario can well explain the occurrence of many features in a solar flare. However, it is not clear how the internal reconnection can happen in the beginning of the process. Some observational evidences by using SDO/AIA data have been presented to show that tether cutting reconnection happen in several flares (Liu et al., 2013; Chen et al., 2014; Xue et al., 2017).

1.5.2 Ideal MHD Instabilities

Electric current can be assumed to appear in the corona at the height h, where ambient coronal field (B_{ex}) exists. To satisfy the the boundary condition on the photosphere, one can place a virtual mirror current with opposite direction at a distance h below the surface (van Tend and Kuperus, 1978). The equilibrium of the system can be achieved by the balance of downward Lorentz force coming from B_{ex}

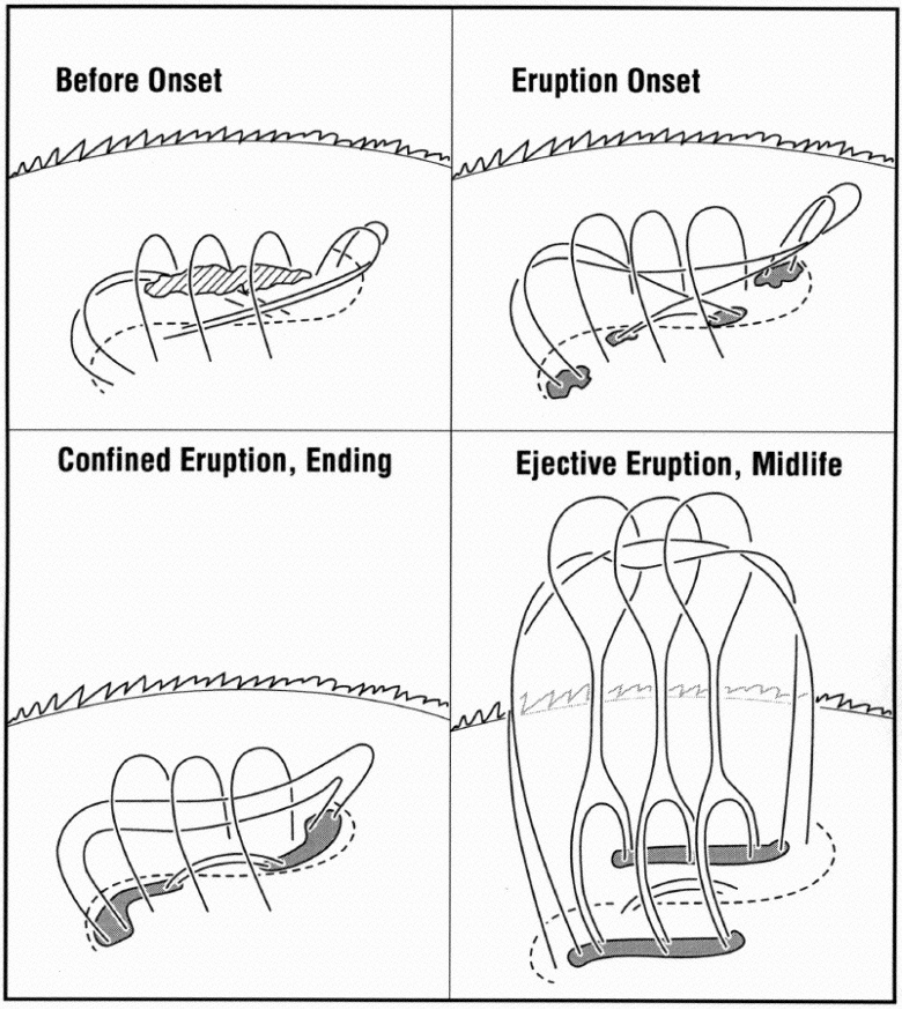

FIGURE 1.7: Schematic diagram of the tether cutting model (reprinted from Moore et al. (2001)).

acting on the current and the upward force generated by the repulsion of the two opposite line currents.

In the corona, one can also consider a current carrying loop that has a form like a torus. This ring current flows from one point to another point on the photosphere with a symmetric shape of a half torus in the corona (Kliem and Török, 2006; Démoulin and Aulanier, 2010). One can also put an half-torus as an image current below the photosphere to conserve the normal component of magnetic field on the photosphere. Figure 1.8 shows the Titov-Demoulin equilibrium which represents a flux rope and the overlying field. In this kind of system, one should consider the hoop

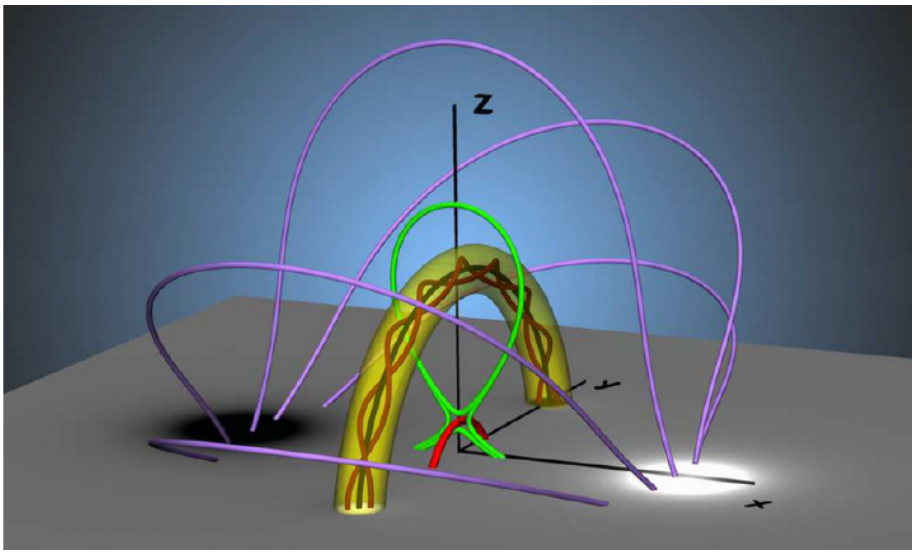

FIGURE 1.8: Titov-Demoulin bipole AR model with current channel and overlying field (reprinted from Kliem et al. (2014)).

(repulsive) force due to the curvature of the ring current. This repulsive force can also be balanced by the force acting from the external field B_{ex} of the coronal arcade surrounding the loop (Titov and Démoulin, 1999). The instability of this system can happen when the external field reduce with height so fast that the restoring force is weaker than the hoop force. This is known as the torus instability (TI). Since this instability can be achieved without any dissipation related to electric resistivity, this instability belongs to the ideal MHD instability. The instability parameter is given by n-index, which shows how fast the external field decreases with height (Bateman, 1978). The critical threshold of the torus instability for the external field is given by $n > 1.5$ (Bateman, 1978; Kliem and Török, 2006), where n is defined as:

$$n = -R\frac{d\ln B_{ex}}{dR}. \tag{1.15}$$

In order to verify the importance of torus instability in the solar eruption, several attempts have been done to analyze the relation between the decay index and eruption. One can extrapolate the potential field of an AR and derive the decay index of the AR to evaluate the relation between the coronal magnetic topology and the

eruptive behaviour. By using this method, torus instability have been proposed as possible mechanism to drive CMEs or filament eruptions, e.g. Zuccarello et al. (2014); Woods et al. (2018). The critical decay index of the eruption can vary between 1.1 - 1.5 depending on flux rope (Zuccarello et al., 2016). However, it is still not clear how to analyze the decay index of the AR accurately since the decay index is usually measured by the potential field, which is not realistic enough to model the real coronal field.

Another ideal MHD instability that commonly used to explain the solar eruption is the kink instability (KI). Solar flares are usually generated from the regions in the photosphere with horizontal component of magnetic field almost parallel to the magnetic PILs. Conservation of magnetic helicity suggests that the shearing motion and the emerging of sheared magnetic field in the photosphere can carry the helicity to the chromosphere and the corona to form high-twist field lines or flux rope (Hagyard et al., 1984; Priest et al., 2016). The magnetic twist as a component of magnetic helicity can be important since a highly twisted magnetic field can be subject to the helical kink instability (Hood and Priest, 1979). When the twist of a flux rope exceeds a critical instability state, flux rope can erupt. In the ideal line-tying condition, the critical threshold for the twist of a flux rope is $\sim$1.25 turns or $\sim 2.5\pi$ radians (Hood and Priest, 1979). Based on the simulation using the Titov and Démoulin (1999) equilibrium, Török et al. (2004) found the threshold to be $\sim 3.5\pi$ radians. Figure 1.9 shows the consistency between the eruption features in the simulation and observation.

Several authors have tried to determine the twist via various techniques i.e. Rust and Kumar (1996) used the ratio of length to width, Leka et al. (2005) employed the best-fit of linear force-free fields to the observations, Leka and Barnes (2007) examined moments of a twist parameter. Bobra and Ilonidis (2016) used the mean value of force-free parameter (α) as a proxy for the twist in their prediction method using machine learning, but they found that it was not a significant predictor for CME. Leamon et al. (2003) argued that the pre-flare coronal fields in ARs rarely have

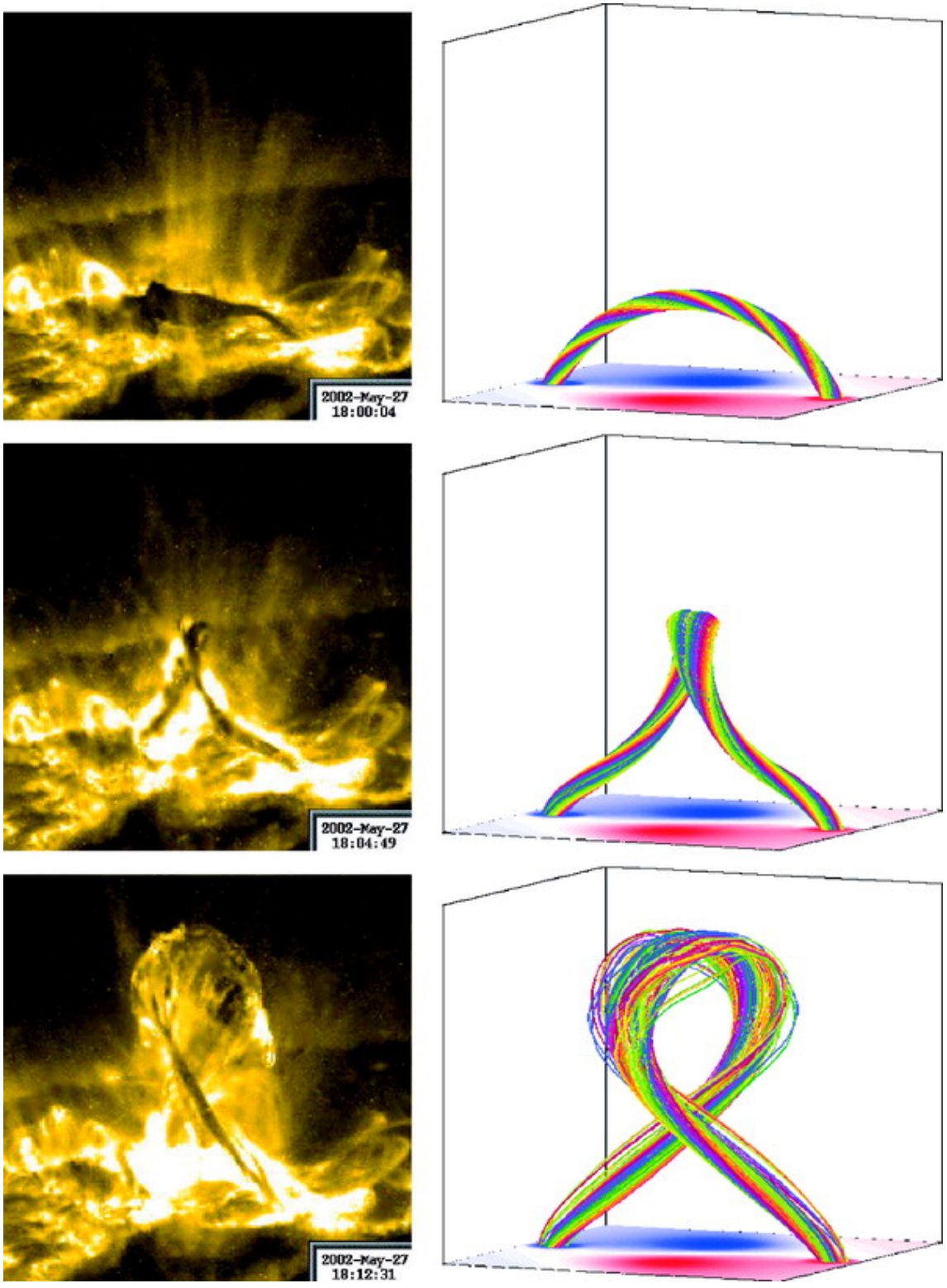

FIGURE 1.9: Simulation of the kink instability in the Sun (left panels) and the observations by Trace 195 Å (right panels). Reprinted from Török and Kliem (2005).

sufficient twist for the kink instability. However, from their study of many sigmoids, Rust and LaBonte (2005) showed observational evidence for the kink instability in solar filament eruptions.

Recent studies have attempted to calculate the twist of the field lines from a NLFFF model based on the photospheric magnetic field data (Inoue et al., 2011, 2013; Guo et al., 2013; Liu et al., 2013). With a NLFFF model, one can calculate the twist of each field line to determine the distribution of twist for the whole AR. However, it is still debatable how to define the twist of a flux rope that consists of many field lines (Liu et al., 2016). Pevtsov et al. (2014) suggested that a proper definition of magnetic twist for an AR should be normalized by the magnetic flux, since the number of field lines is infinite. Liu et al. (2016) showed that an NLFFF model can reconstruct a high-twist magnetic flux rope that exceeds the kink instability threshold before a flare. They suggested that the twist of the flux rope axis can be used as a parameter in forecasting solar eruption. Several studies based on the NLFFF models for different ARs have shown that the pre-flare coronal fields are weakly twisted (Bobra et al., 2008; Inoue et al., 2014a, 2015). Inoue et al. (2014a) pointed out that a triggering mechanism associated with magnetic reconnection may make it possible for a magnetic structure with a twist less than the kink instability threshold to produce a flare. Therefore, it may not be necessary for a magnetic structure in an AR to have a twist greater than 1.25 turns in order to produce a flare, even if the kink instability works as the driver for the main phase of the flare.

1.6 Double-Arc Instability

Recently, Ishiguro and Kusano (2017) introduced a new type of instability, so called the double-arc instability (DAI). Their motivation was to define a criteria of the instability of a sigmoid, which can be assumed in its simple form as a double-arc structure. In this scenario, suppose there is a structure of current-carrying loop

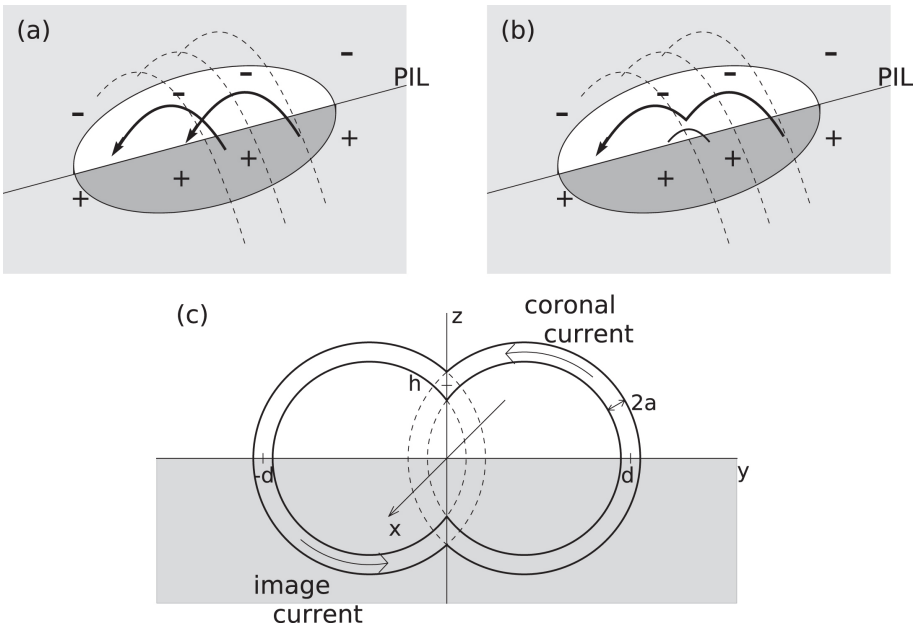

FIGURE 1.10: Schematic process of the formation of the double-arc structure in the solar corona (a,b) and the double-arc current loop with its image current (c) (reprinted from Ishiguro and Kusano (2017)).

as a combination of two joined symmetric loops that interact so that the current flowing in a double-arc shape loop. The shape of the double-arc structure depends on the distance between the two circular loops. The schematic of the formaton of the double-arc loop and its variation are shown in figure 1.10 and 1.11. The joint height is denoted as h, while d represents the distance between the farthest footpoints of the double-arc loop. The double-arc structure is controlled by the joint height (h) that can vary from $h = 0$ to $h = d$, while the distance between the two farthest footpoints is fixed. The double-arc loop can be formed as a result of an internal (tether-cutting) reconnection between the field lines in the force-free magnetic arcade.

Similar to its counterpart, torus instability, the equilibrium state of the double-arc structure can be achieved when the restoring force due to the external magnetic field is strong enough to compensate the repulsive force because of the curvature of the double-arc loop. Since the TI and DAI work under the same consideration of the hoop force, these two instabilities can be classified as the hoop-force-instability scenario. From their numerical analysis of this double-arc structure, Ishiguro and

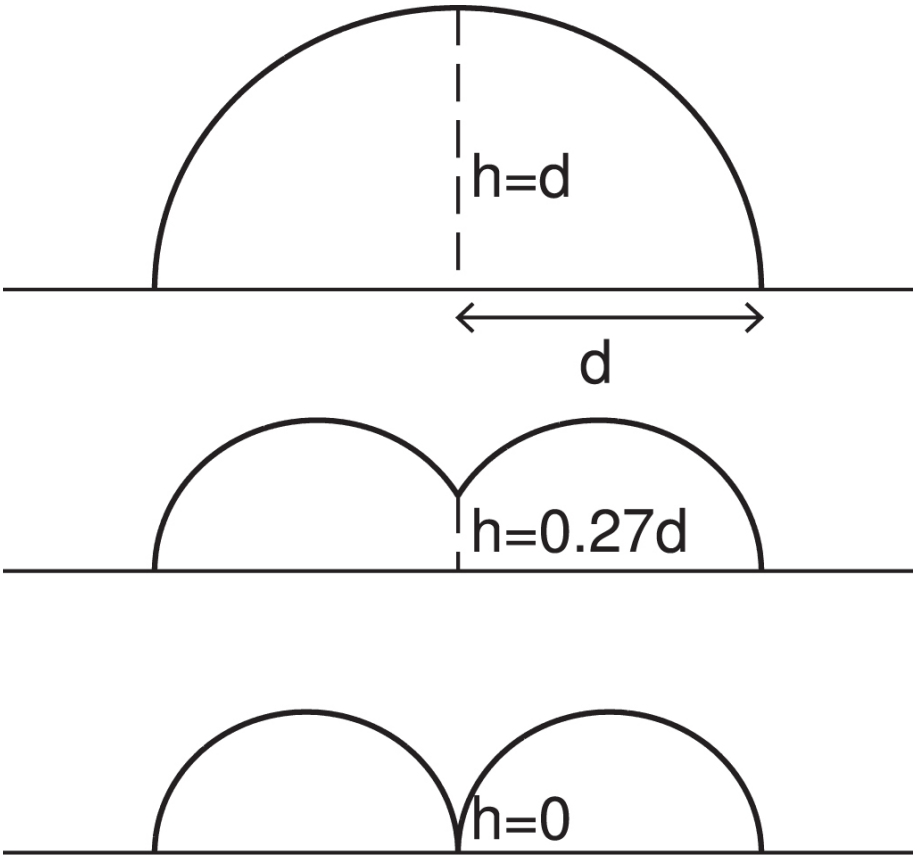

FIGURE 1.11: Schematic diagram of double-arc structure with joint height and distance between the footpoints (reprinted from Ishiguro and Kusano (2017)).

Kusano (2017) found that it is more easily unstable than the torus structure. They also found that the DAI can even grow in the circumstance that the decay index is zero,where there is no change of the external field with height. These two properties, which are caused by the more complex configuration of the double-arc structure, mainly differentiate the DAI and the TI.

In order to analyze the critical condition of the DAI, Ishiguro and Kusano (2017) introduced a new parameter, κ. In the following paragraphs, we will explain what is κ and how this is derived from the double-arc loop model as it described by Ishiguro and Kusano (2017).

Recall equation 1.5 and the current density in the force-free field, we know that $\boldsymbol{J} \propto \boldsymbol{B}$, which implies that the current (I) flowing on the double arc loop can be

presented as,

$$I = \frac{\alpha}{\mu_0}\phi_{rec}. \tag{1.16}$$

According to the numerical analysis by Ishiguro and Kusano (2017), for the double arc loop located within the point source external field, the critical current for DAI to grow should be

$$I \geq \frac{4\phi}{\mu_0 d}, \tag{1.17}$$

therefore, using the definition of I in equation 1.16, equation 1.17 can be rewritten as

$$\alpha d \geq \frac{4\phi}{\phi_{rec}}. \tag{1.18}$$

Here, ϕ is the point source magnetic flux that represents the bipole sunspot with distance $2d$ between the poles, adopting the same configuration of external magnetic field in Démoulin and Aulanier (2010). This bipole spot is located in such a place that the magnetic field is perpendicular to the current flowing on the double arc loop. The total flux is defined as $\phi_{tot} = 4\pi\phi$. By defining the twist of a magnetic field line following Berger and Prior (2006) as

$$T_w = \int \frac{\alpha}{4\pi} dl, \tag{1.19}$$

we can estimate the twist of a single arc with radius $d/2$ by

$$T_w = \frac{\alpha d}{8}. \tag{1.20}$$

By assuming that the tether cutting reconnection happens near the footpoint of the field lines with twist T_w, the total twist for the double arc will be

$$T_w = \frac{\alpha d}{4}. \tag{1.21}$$

Using the definition of twist of the double arc in equation 1.21 and the definition of total flux, we can rearrange equation 1.18 of the critical current for the DAI as

$$T_w \frac{\phi_{rec}}{\phi_{tot}} \geq \frac{1}{4\pi}. \tag{1.22}$$

Here, the left hand term in equation 1.22 is defined as

$$\kappa = T_w \frac{\phi_{rec}}{\phi_{tot}}. \tag{1.23}$$

From numerical analysis of different external fields variation, they found that the critical conditions occur when:

$$\kappa > 0.125, \tag{1.24}$$

for the exponentially decayed external field, and

$$\kappa > 0.175, \tag{1.25}$$

for the uniform external field.

In general, Ishiguro and Kusano (2017) suggested that the critical condition for the DAI can happen when κ exceeds its critical threshold, which is determined by the the external field configuration. Furthermore, since κ consists of the elements of twist and reconnected flux, it can be interpreted that the eruption of a double arc will take place when there is enough amount of flux that is reconnected as well as strong magnetic twist. In the context of eruption in the Sun, the DAI analysis implies that the flux rope in the core of an AR (i.e. high free energy region), which can be responsible for a solar flare, may be unstable against the DAI when the magnetic twist of this flux rope is strong or there is a big portion of the magnetic flux that is reconnected. Note that since the DAI is analyzed with the constraint of limited height of double arc loop, this means that the DAI can only explain the early phase of eruption. In other words, the DAI may only be applied to explain the occurrence

of a solar flare, but it cannot be used to determine whether the structure will be succesfully erupted (i.e. becomes CME) or not. This is because the DAI may work to drive an eruption of a double arc loop, but when the structure becomes more like a single torus, then other mechanisms should be taken into account (e.g. torus instability).

Although Ishiguro and Kusano (2017) showed a rough estimation of reconnected flux derived from the observational study by Bamba et al. (2013) to verify their result, there is still no further study that tries to verify the critical condition of the DAI. Because the reconnected flux before the onset of a flare is very difficult to measure, the calculatoin of κ for real flare event is somewhat difficult to do. Therefore, it is very important to find a way to estimate κ more carefully, so that the DAI scenario can be verified for a real flare event.

1.7 Flare Trigger Model

Tether cutting mechanism, as has been described before, can well explain the flare process as well as many features observed in a flare. This scenario has also been observed directly from the multi-wavelength analysis using SDO/AIA data and H-α observation. However, this model lacks to provide the trigger mechanism of the internal reconnection before the onset of the flare. Since tether cutting reconnection serves as an essential mechanism to form a double-arc structure (sigmoid) from a magnetic arcade, revealing the possible trigger for internal reconnection is very crucial to create a complete scenario for a solar flare.

In order to provide such an alternative explanation of trigger for the tether cutting mechanism, a parametric simulations study has been performed by Kusano et al. (2012). In their simulations, a simple large-scale LFFF was used as a test magnetic structure that various orientation of small-scale magnetic bipole fields were imposed from the bottom boundary of the simulation box. The schematic simulation set-up

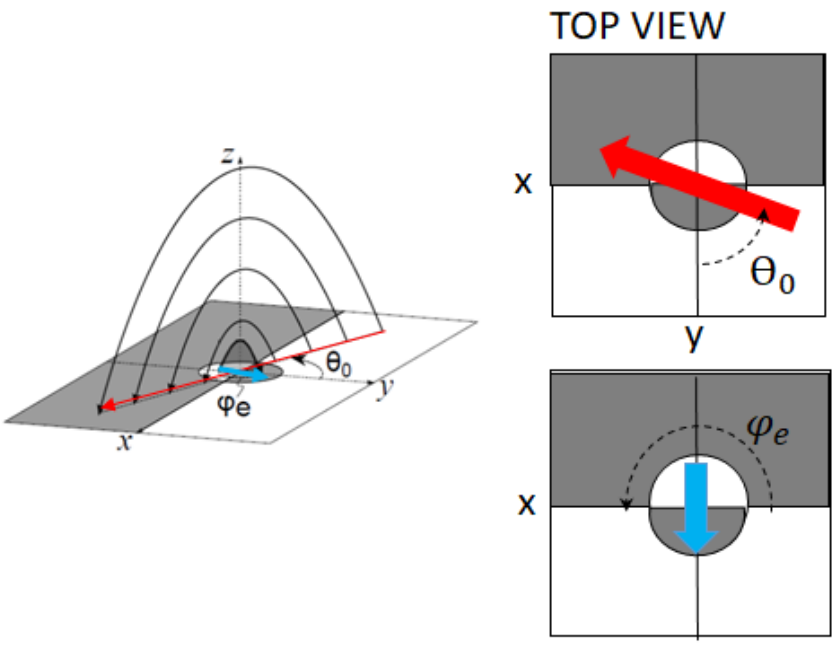

FIGURE 1.12: Schematic diagram of the simulation performed by Kusano et al. (2012).

of their simulations is shown in figure 1.12. By varying the azimuth angle (θ_0) of the large-scale structure with respect to the PIL, one can get different shear angle as well as different magnetic energy level contained in the system. Several runs of simulation for different orientations (ϕ_e) of emerging flux were performed to survey the effective trigger structure and magnetic configuration to produce a solar flare. The result of their simulation is presented in figure 1.13.

Based on their simulations, the LFFF that has horizontal components almost parallel to the PIL is more easily to be destabilized by the small perturbation. This indicates that an AR whose strong horizontal components are more parallel to the PIL has more chance to produce a flare. Moreover, there are two main categories of bipole structures that can effectively trigger a flare when these bipoles are injected to the highly sheared LFFF. These two categories are: opposite polarity (OP) and the reversed shear (RS) structures. Opposite polarity refers to the small bipole structure whose polarity is opposite with respect to the polarity of the large-scale field structure at the PIL. Reversed shear polarity refers to the small bipole structure

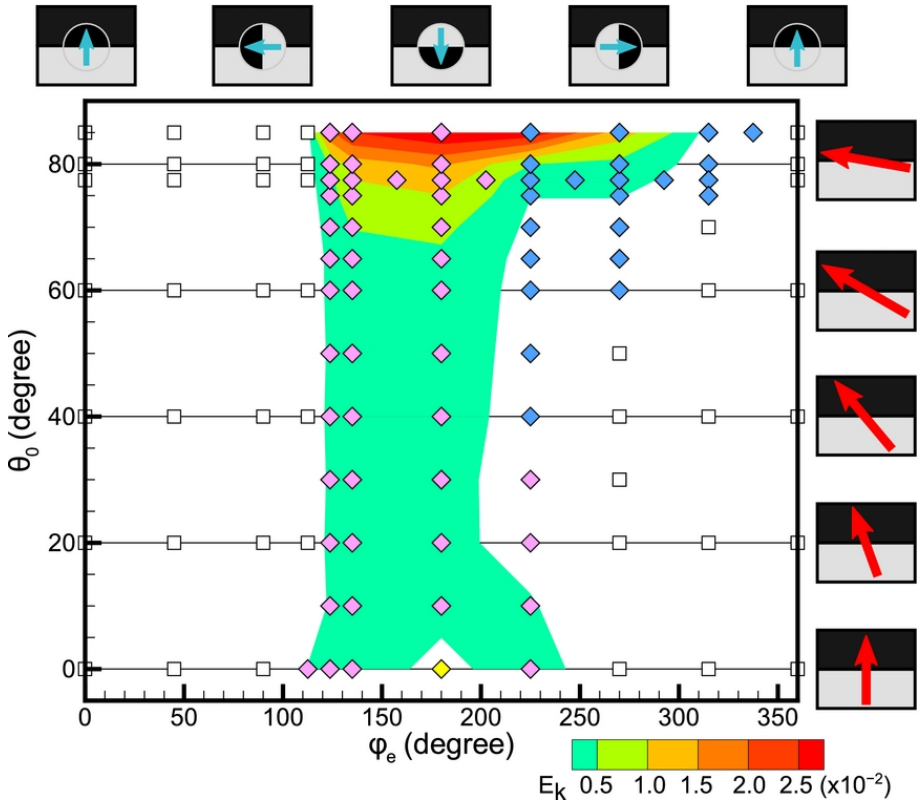

FIGURE 1.13: Results summary of the simulation performed by Kusano et al. (2012) (reprinted from Kusano et al. (2012)).

which is directed nearly opposite to the shear component of the field.

The detail comparison between OP-type and RS-type structures in the simulation was described by Kusano et al. (2012) and shown here in figure 1.14 and 1.15. Based on the relation between flare reconnection and flux rope formation that happen, the eruption cases in their simulations can be categorized into two distinct groups, which are "eruption-induced reconnections" and "reconnection-induced eruptions". The former is the case when the flux rope is formed before the flare reconnection occurs. In this case, the emerging bipole flux triggers the creation of an unstable flux rope through pre-flare reconnection. Subsequently, the flare reconnection is generated below the flux rope during its eruption. As for the latter, the role of the emerging bipole is to trigger the reconnection between pre-existing magnetic field by reducing the shear of the overlying field which then creates an unstable flux rope. The "eruption-induced reconnections" process is clearly observed in the

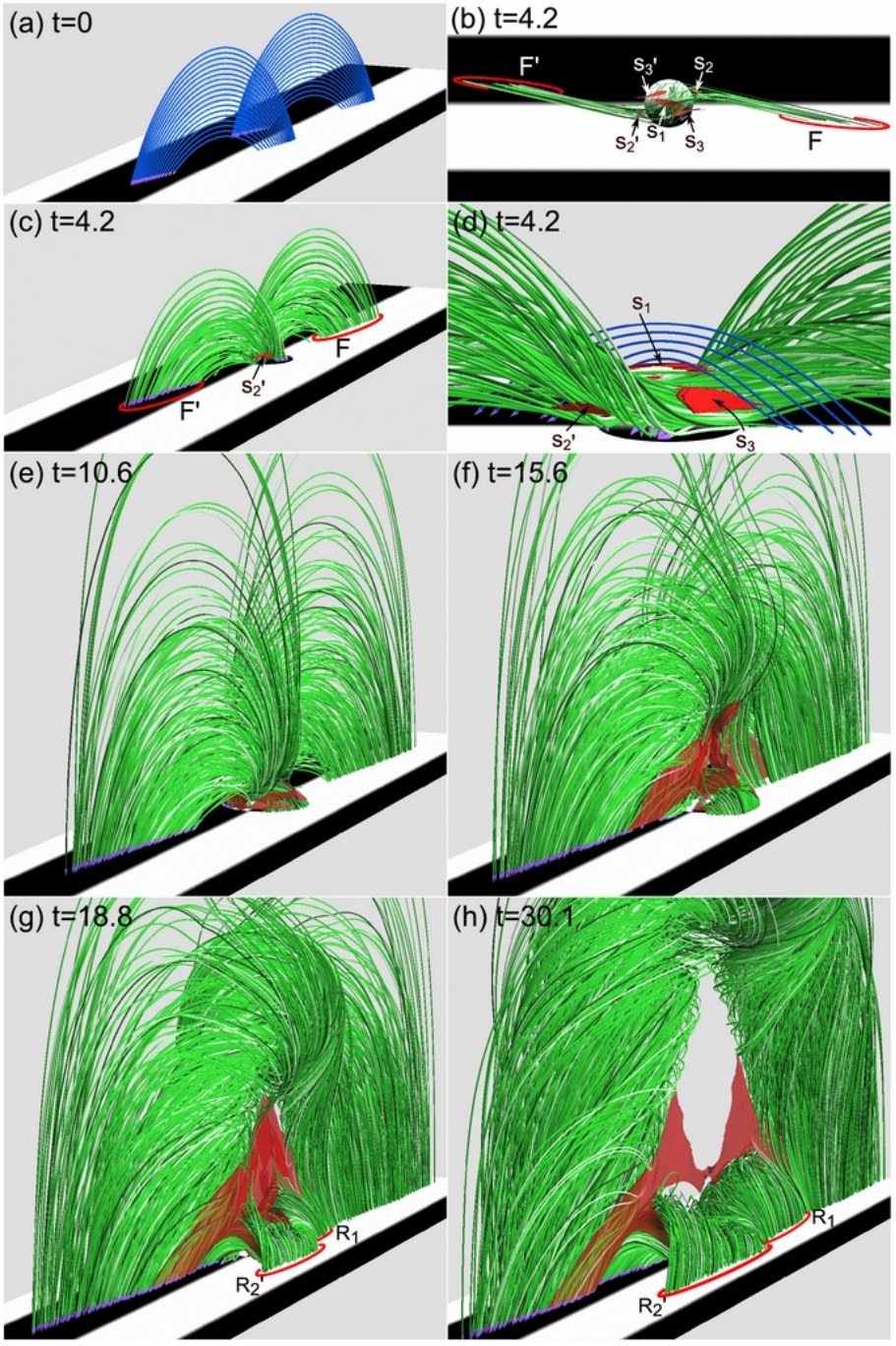

FIGURE 1.14: Eruption-induced reconnection process in the simulation where OP-type emerging flux was imposed to the LFFF structure (reprinted from Kusano et al. (2012)).

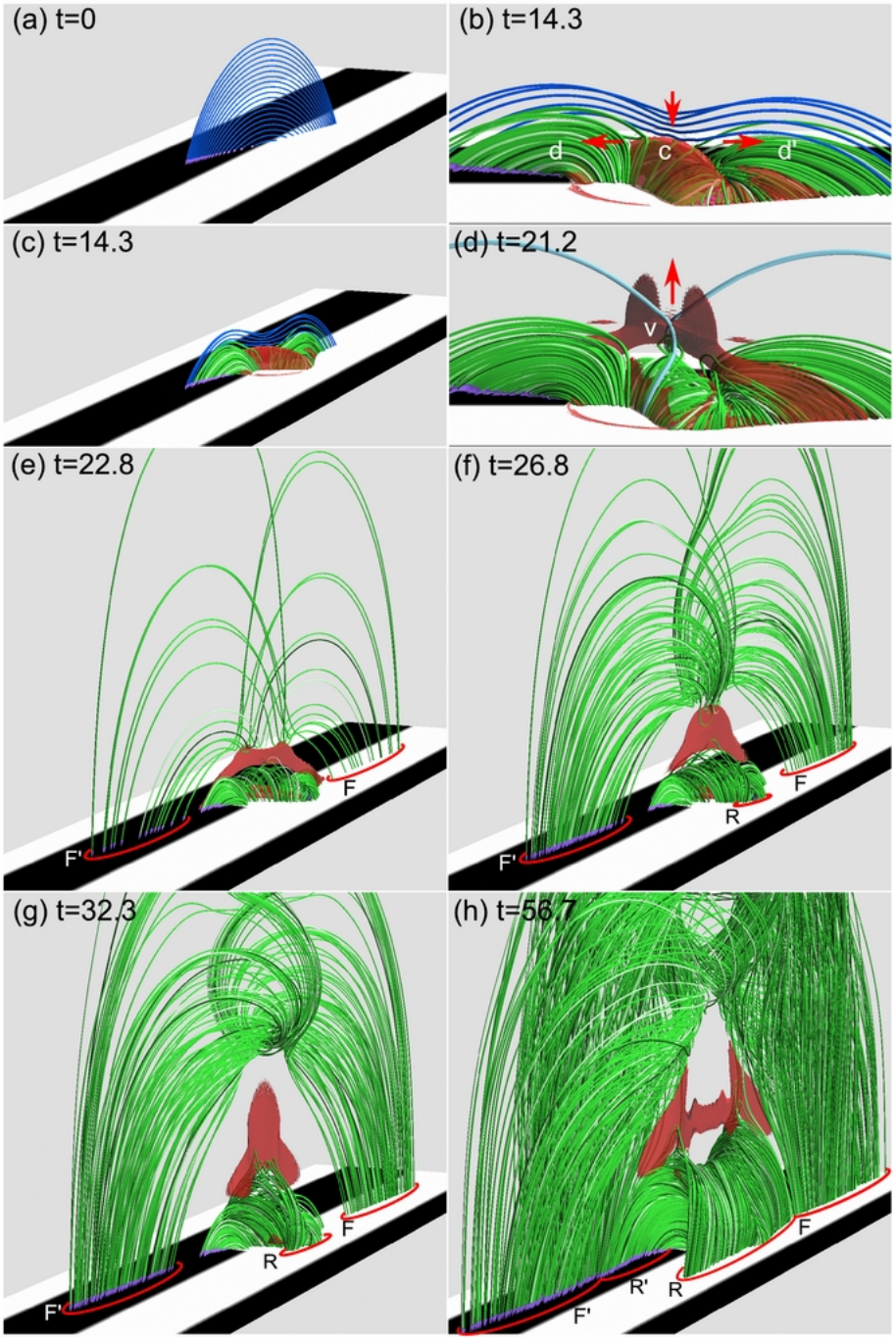

FIGURE 1.15: Reconnection-induced eruption process in the simulation where RS-type emerging flux was imposed to the LFFF structure (reprinted from Kusano et al. (2012)).

OP-type emerging flux cases, while the "reconnection-induced eruptions" happen in the RS-type cases.

In order to examine the model of solar flare trigger mechanism proposed by Kusano et al. (2012), several observational analysis of flare events have been conducted by using Hinode (Kusano et al., 2012; Bamba et al., 2013; Toriumi et al., 2013) and SDO data Bamba et al. (2014). From their results, several flare events can be explained to occur as a result of the flare trigger mechanism proposed in the Kusano et al. (2012). These results also suggested that the magnetic shear angle in the flaring regions should exceed 70° to erupt prior to the flare onset. However, in the real solar environment, the critical size of the flare trigger field may varies among the flare events Bamba et al. (2013). Moreover, observational study shows that the flare trigger may not only occur in the form of emerging flux as it studied in the simulation, but also can be achieved through a variety of dynamic process, while the essential of magnetic configuration can be classified as OP and RS (Toriumi et al., 2013). Although the simulations by Kusano et al. (2012) provide important characteristics of the trigger structures and magnetic configurations that are able to produce large flares, the simulations were performed in the simple magnetic structure, which is not the case in the real Sun. Therefore it is important to verify the scenario of their trigger mechanism in the more realistic magnetic field structure.

1.8 Scientific Objective

We have mentioned many theories proposed in previous papers to explain how the magnetic energy is built-up in the corona and how the flare process can take place. In general, it is well known that large AR with strong magnetic shear near the PIL will store more energy than small AR that is weakly sheared. However, it is still not clear how the initial mechanism that allows the AR with high magnetic energy work

to release the energy as a solar flare. We have shown that the tether-cutting mechanism can conceptually explain many features in the Sun and has been convincingly observed in several flares. Therefore, we adopt the tether-cutting mechanism as the main scenario in our study. To explain the initial perturbation that will cause the tether-cutting reconnection, the trigger mechanism by Kusano et al. (2012) is used. This trigger mechanism can work in the various conditions of magnetic field observed in the Sun and is consistent with the conceptual idea of tether-cutting scenario. Furthermore, the DAI theory can provide suitable explanation of the instability of magnetic structure formed by the tether-cutting reconnection. In summary, the flare trigger mechanism proposed by Kusano et al. (2012) that is complemented by the DAI theory can well explain the initial process of solar flares, which is important to understand the onset of a flare. However, these scenarios have only been applied in the theoretical model of coronal field.

Since the real coronal field is much more complex than the symmetrical and ideal theoretical model used in the Kusano et al. (2012) and Ishiguro and Kusano (2017), it is important to extend their works and to implement their theory in more practical situation. This step is very important to verify the validity of their theories as well as to implement the theories for the real forecasting of flares. Therefore, in our study, we aim to implement the trigger mechanism proposed by Kusano et al. (2012) and the DAI theory by Ishiguro and Kusano (2017) in a more realistic coronal field. For this purpose, we define the main subjects of our study as follow: First, to extend the flare trigger model by Kusano et al. (2012) for the more realistic coronal field reconstructed from the observed magnetogram data provided by Hinode satellite. The goal of this study is to reveal which magnetic field configurations are effective for triggering a flare. Second, to explore the new method of implementing DAI analysis for more realistic coronal field reconstructed from the observed magnetogram data provided by SDO. Our goal is to find a parameter that can be used to study the capability to produce a solar flare by implementing such a DAI analysis for a real AR. We study the spatial and temporal evolution of the twist distribution of the

AR based on the NLFFF model. After that, we calculate a parameter to enable us to extract information about the twist and to determine the reconnected flux. Next, we show how our proposed parameter can be used as a possible forewarning for the likelihood of flare occurrence in an AR.

Finally, we expect to provide a more comprehensive view of flare trigger mechanism that covers the effective trigger structure as well as the stability of a magnetic structure prior to a flare. This is conducted by combining the analysis of flare trigger structure proposed by Kusano et al. (2012) and the DAI analysis proposed by Ishiguro and Kusano (2017) for real observational data. Through this study, we aim at contributing to the improvement of flare prediction for space weather forecast.

Chapter 2

Data and Methods

2.1 Observational Data

Coronal magnetic field is important since it contains the energy to be released in a flare. Flare onset is also determined by the instability of the magnetic field in the corona. Therefore, understanding the coronal magnetic field of the Sun prior to a flare is very crucial in order to know the possibility of flare occurrence. Unfortunately, obtaining information of coronal magnetic field is very difficult, since the emission from the corona is too low for the spectroscopic observation of magnetic field sensitive line. However, one can obtain the information of the magnetic field in the photosphere and infer the coronal field from this. In this context, photospheric magnetic field data is very essential in the study of flare prediction.

Information of the photospheric magnetic field is given by the magnetogram data. There are plenty of ground-based and space-based instruments that can provide magnetogram data, two of them are Solar Optical Telescope (SOT) onboard Hinode satellite and Heliospheric Magnetic Imager (HMI) onboard SDO satellite. These two instruments can produce vector magnetic field data of the photosphere that make us able to obtain the line-of-sight component of magnetic field as well as the

tangential components. This vector magnetic field can be very useful to provide the required inputs for the coronal field extraplation. SOT can produce the highest spatial resolution magnetogram data that ever exist today coming from a space-based observation. This is very important for the accurate reconstruction of coronal field and for the study of flare trigger. On the other hand, HMI can provide the highest temporal resolution of full-disk magnetogram data. This is very useful to provide the almost continuous observation that will give comprehensive evolution of an active region in the Earthward side of the Sun. In this thesis, we use the magnetogram data from the Hinode/SOT and SDO/HMI to reconstruct the coronal magnetic field as well as to analyze the flare trigger mechanism.

In order to confirm the coronal field models and the simulation results, it is important to have imaging observation of plasma in the corona. Since magnetic field is frozen in the coronal plasma, the shape of the coronal loop observed in the EM spectrum can be used to infer the shape of the magnetic field. The good coronal model should be at least in a good agreement with the shape of coronal loop observed from the observation. In addition to that, flare ribbon that can be considered as the imprint of the footpoints of a flux rope during a flare is well observed in the observation. Therefore, using the data from observation is very essential to verify the coronal model and also to confirm the simulation results. For this reason, we used several instruments in this study, which are X-Ray Telescope (XRT) onboard the Hinode satellite and Atmospheric Imaging Assembly (AIA) onboard SDO. The detailed description of the instruments used in this study is presented in the following subsections.

2.1.1 Hinode Spacecraft

Hinode (formerly Solar-B) is a Japanese mission developed and launched by ISAS/-JAXA, collaborating with NAOJ as a domestic partner, NASA and STFC (UK) as

international partners. Hinode model with the three main instruments aboard Hinode is shown in figure 2.1. The Hinode spacecraft was launched on September 2006 into an elliptical polar orbit that makes Hinode can observe the Sun continuously for a duration of nine months each year (Kosugi et al., 2007). The main objective of Hinode mission is to investigate magnetic activity of the Sun including its generation, energy transfer, and release of magnetic energy (Kosugi et al., 2007). The scientific payload consists of SOT, Extreme Ultra Violet Imaging Spectrometer (EIS), and X-Ray Telescope (XRT). SOT consists of Optical Telescope Assembly (OTA) and its Focal Plane Package (FPP). The FPP has four optical channels, which are the Narrowband Filter Imager (NFI), the Broadband Filter Imager (BFI), the Spectro Polarimeter (SP), and the Correlation Tracker (CT). The scientific goals that intended to be studied by SOT are coronal heating, reconnection, coronal waves, active regions, sunspots, flux tubes, quiet-Sun magnetic fields, data-driven simulation of coronal dynamics, and chromospheric heating (Tsuneta et al., 2008). The vector magnetogram data are produced by the SP instrument by obtaining line profiles of two magnetically sensitive Fe lines at 630.15 and 630.25 nm and the nearby continuum by using a 0.16×151 arcsec slit. The solar image can be reconstructed by combining all data scanned by the slit to map an area up to the full 320-arcsec-wide field of view (FOV) (Tsuneta et al., 2008).

XRT onboard Hinode contains total nine X-ray analysis filters, which are Al-mesh, Al-poly, C-poly, Ti-poly, Be-thin, Al-med, Be-med, Al-thick, and Be-thick (Golub et al., 2007). These filters pass wavelength bands with different lower cutoff energy (Kosugi et al., 2007). Each of the analysis filters has different temperature response. The ratio between two different filters can give the coronal-temperature-diagnostic, which is very useful for solar flare study. The whole coronal-temperature of the XRT observation range from less than 1 MK to more than 10 MK (Narukage et al., 2014). The XRT has field of view 34×34 arcmin^2 that can cover whole solar disk when the spacecraft is pointed at the Sun center (Kosugi et al., 2007)). In this thesis, we used XRT observation to compare the result of the NLFFF extrapolation for AR 10930.

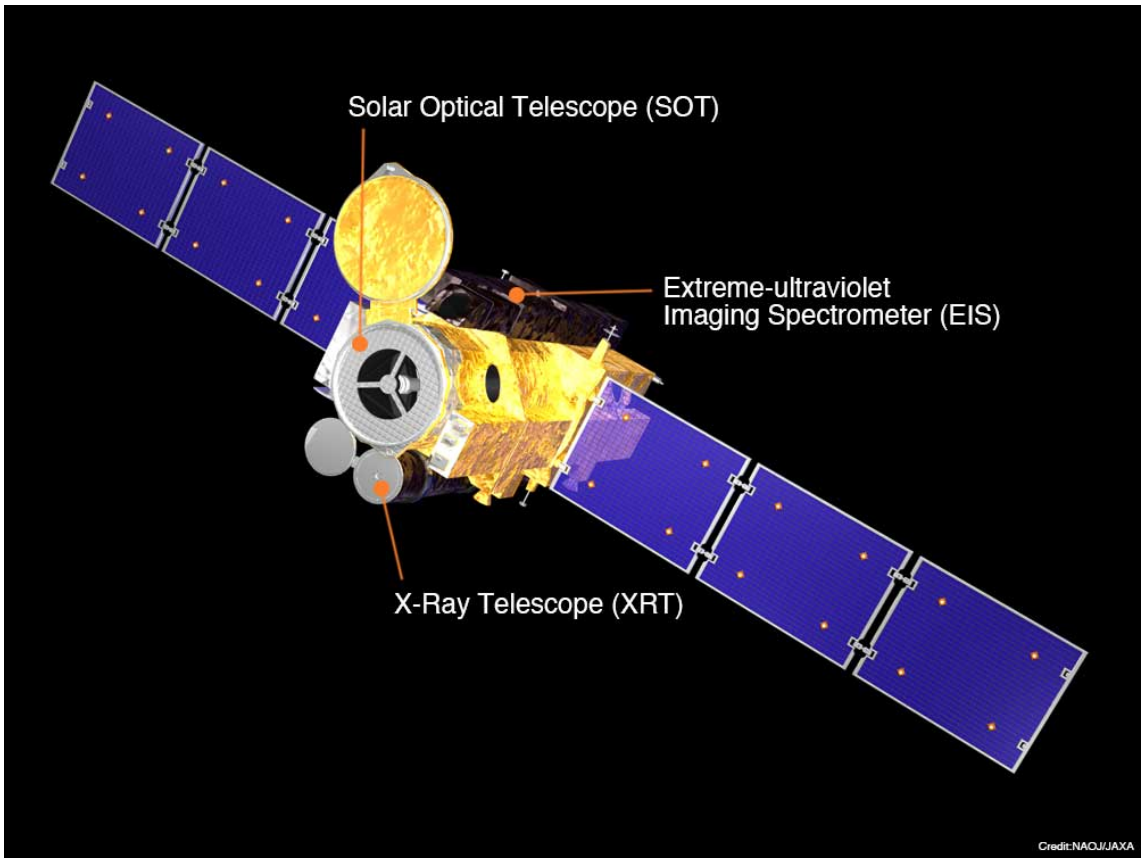

FIGURE 2.1: Hinode spacecraft (Credit: NAOJ/JAXA).

We used Ca II H line (3968.5 Å) data from the Broadband Filter Instrument (BFI) in the SOT for the purpose of examining the NLFFF and MHD simulations results with the appearances of the flare ribbons. BFI can cover the area on the Sun over a 218 × 109 arcsec FOV (Tsuneta et al., 2008). The data are available in the Hinode Science Center at National Astronomical Observatory of Japan (NAOJ) and Nagoya University. The data are processed through some procedures following SOT data analysis procedures given in the Hinode Solar Optical Telescope Data Analysis Guide document. The procedures were carried out with the SolarSoftware (SSW) IDL packages in the Solar Data Analysis System (SDAS) at NAOJ and Hinode Science Center system in Nagoya University.

The X-ray images for the AR 10930 in this thesis were obtained from the XRT instrument. These images are important to compare the agreement of the NLFFF

results with the observed coronal magnetic field lines. We carefully selected the image corresponding with the field of view of the SP magnetogram data in order to overlay the field lines with the field lines of NLFFF. We followed the procedures from SolarSoft XRT Analysis Guide to obtain the XRT image. Image processing was also conducted in the Solar Data Analysis System (SDAS) at NAOJ and Hinode Science Center System in Nagoya University.

2.1.2 SDO Spacecraft

SDO is a solar science mission launched by NASA in February, 2010, and continuously observes the Sun since then from the geosynchronous orbit. SDO was designed to study various aspects of solar variability, especially that affect the space weather or earth environment (Scherrer et al., 2012). SDO carries three instruments, which are Helioseismic and Magnetic Imager (HMI), Atmospheric Imaging Assembly (AIA), and EUV Variability Experiment (EVE). SDO satellite model is shown in figure 2.2. HMI covers full-disk observations of vector magnetic field with high time cadence. AIA observes solar atmosphere and produces images of the solar atmospheres in multiple wavelengths with high spatial and temporal resolution. EVE measures the solar EUV irradiance with high spectral and temporal resolution. In this thesis, we particularly used vector magnetic field data taken by HMI, as well as some optical observations taken by AIA in EUV wavelength.

HMI has primary goal to investigate the origin of solar variability and to understand the solar interior and various aspects of the Sun related its magnetic activity (Scherrer et al., 2012). It was designed to measure the Doppler shift, intensity, and vector magnetic field at the solar surface using 6173 Å Fe I absorption line (Schou et al., 2012). HMI can produce full disk magnetogram data with 1 arcsec spatial resolution. One photopsheric line-of-sight (LOS) component is collected every 45 seconds with the HMI Doppler camera and the other is computed every 720 seconds using filtergrams recorded by vector field camera. HMI produces vector magnetic

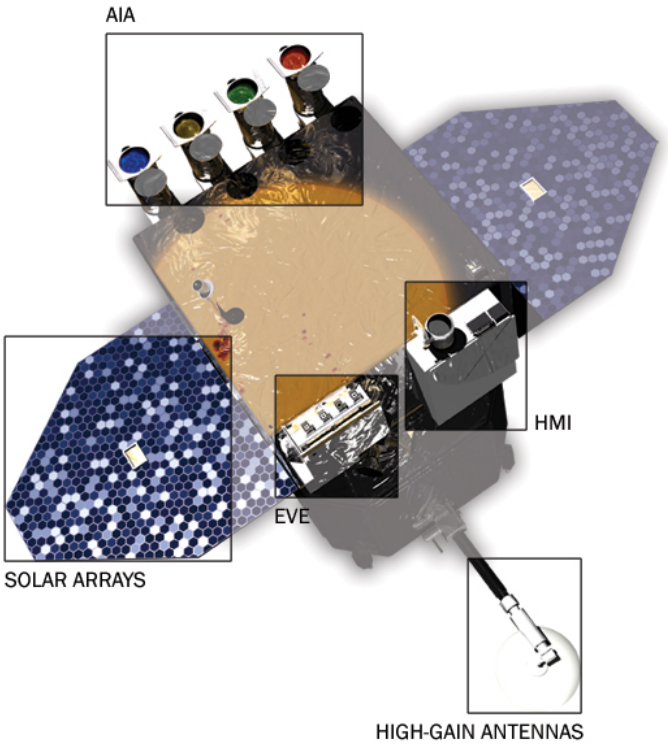

FIGURE 2.2: Solar Dynamics Observatory spacecraft (Credit: NASA).

field data in the spherical coordinate with 45 seconds (hmi.M_45s) and 12 minutes (hmi.M_720s) cadences.

We have used SDO/HMI observations of the vector magnetic field from the Spaceweather HMI Active Region Patch (SHARP) (Bobra et al., 2014). SHARP data have a 12-minute cadence of observations, in which the magnetic flux has been remapped to a Lambert Cylindrical Equal-Area (CEA) projection[1]. These data contain the three components of the vector magnetic field (B_r, B_ϕ, B_θ) obtained from a very fast inversion of the Stokes vector using Milne-Eddington model for the solar atmosphere (Borrero et al., 2011). SHARP data enable us to obtain the vector magnetic field data in radial direction instead of LOS component that is more suitable for the data analysis in cartesian coordinate.

[1]The SHARP (CEA) data (hmi.sharp_cea_720s) is available on the Joint Science Operation Center (JSOC), Stanford University (http://jsoc.stanford.edu/).

AIA instrument has its scientific focus on the investigation of the magnetic environment of solar atmosphere and its interaction with surrounding plasma. AIA consists of four 20-cm telescopes, which observe 41-arcmin field of view, that can provide 10 images of the Sun in 10 different wavelengths within 10 seconds (Lemen et al., 2012). The complete description of 10 wavelength channels observed by AIA and its corresponding primary ions and region of atmosphere is shown in table 2.1. In this thesis, we have used particularly the AIA observation of the ARs for 1600 Å and 171 Å channels. These data were used to identify the flare ribbons as well as coronal structure during the flares.

TABLE 2.1: Channels of observations in the AIA instrument onboard SDO.

Channel	**Primary ions**	**Characteristic temperature** log(T) (K)
4500 Å	continuum	3.7
1700 Å	continuum	3.7
304 Å	He II	4.7
1600 Å	C IV + cont	5.0
171 Å	Fe IX	5.8
193 Å	Fe XII, XXIV	6.2, 7.3
211 Å	Fe XIV	6.3
335 Å	Fe XVI	6.4
94 Å	Fe XVIII	6.8
131 Å	Fe XVIII,XXI	5.6, 7.0

2.2 NLFFF Method

2.2.1 Vector Magnetic Field

Vector magnetic fields of the solar photosphere used in this thesis were derived from the SOT/SP and SDO/HMI data. SP instrument measures several quantities as degrees of the polarization light, which can be interpreted as Stokes vectors (I, Q, U, and V). These Stokes vectors are then inverted to derive magnetic field strength,

inclination, and azimuth (Wiegelmann and Sakurai, 2012). Synthetic Stokes profiles can be derived by using Unno-Rachkovsky solution for the Milne-Eddington model of atmosphere to do the inversion (Wiegelmann and Sakurai, 2012). From this inversion, line-of-sight (LOS) and horizontal components of magnetic field on the solar photosphere can be derived. Once the LOS and horizontal components are obtained, three components of the magnetic field (B_x, B_y, B_z) can be derived by using transformation function considering the geometry of the Sun (Gary and Hagyard, 1990).

Before using the vector magnetic field for coronal extrapolation, one needs to resolve azimuth-ambiguity of the perpendicular magnetic field components with respect to the line-of-sight component. This azimuth-ambiguity is 180° of ambiguity in azimuth that makes the B_x and B_y components of the vector magnetic field cannot be uniquely derived (Wiegelmann and Sakurai, 2012). Some assumptions of the solar magnetic fields have to be made, since there is no method has been found to resolve this ambiguity by direct observation (Metcalf et al., 2006). There are some algorithms have been developed to resolve the azimuth-ambiguity with different techniques. Based on the tests for the different algorithm solutions using synthetic data, it was found that minimum energy method might be considered as the best method for resolving azimuth-ambiguity (Metcalf et al., 2006; Leka et al., 2009). Minimum energy method, based its algorithm for resolving the azimuth-ambiguity on the minimizing the current density, $\mathbf{J}$, and the field divergence $|\boldsymbol{\nabla} \cdot \boldsymbol{B}|$. This method has been developed by Metcalf et al. (2006) and Leka et al. (2009) and implemented for the Hinode SP data (DeRosa et al., 2009).

In this thesis, we used minimum energy method to resolve the azimuth-ambiguity of the active region NOAA 10930. Full inversion for three components of vector magnetic fields of the AR 10930 were obtained in the pixel size of 1000×512. This pixel size image corresponds to the field-of-view of 297×163 arcsec and covers the area of the Sun equal to 214×118 Mm. The three components of the vector magnetic

fields were used for extrapolating coronal magnetic field by using NLFFF method as it will be described in the following subsections.

2.2.2 Potential Field Extrapolation Method

The first step of reconstructing the coronal magnetic fields of the ARs in this thesis is by applying potential field extrapolation. The potential field will be used as the initial condition in the NLFFF extrapolation that can produce more realistic coronal field. In this thesis, we used Fourier method to extrapolate the potential field (Alissandrakis, 1981). Suppose that ψ is the scalar potential of the magnetic field,

$$\boldsymbol{B} = -\boldsymbol{\nabla}\psi. \tag{2.1}$$

Since the solenoidal condition should be satisfied, then

$$\boldsymbol{\nabla} \cdot \boldsymbol{B} = \boldsymbol{\nabla}^2\psi = 0. \tag{2.2}$$

The scalar potential, ψ can be expressed in the Fourier expansion as

$$\psi = \sum \tilde{\psi}(z) e^{(ik_x x + ik_y y)}. \tag{2.3}$$

Applying 2.2 to the 2.3, the general solution can be obtained as,

$$\tilde{\psi}(z) = \sum \tilde{\psi}_0 e^{-k_z z}, \tag{2.4}$$

where

$$k_z = \sqrt{k_x^2 + k_y^2}. \tag{2.5}$$

Note that $B_x = \partial_x\psi$, $B_y = \partial_y\psi$, and $B_z = \partial_z\psi$, all components of the potential field can be derived as,

$$B_x = \sum \tilde{B_{x0}} e^{(ik_x x + ik_y y - k_z z)}, \tag{2.6}$$

$$B_y = \sum \tilde{B_{y0}} e^{(ik_x x + ik_y y - k_z z)}, \tag{2.7}$$

$$B_z = \sum \tilde{B_{z0}} e^{(ik_x x + ik_y y - k_z z)}. \tag{2.8}$$

The $\tilde{B_{x0}}, \tilde{B_{y0}}$, and $\tilde{B_{z0}}$ is the Fourier component of the magnetic field on the surface of the Sun, B_{x0}, B_{y0}, and B_{z0}, respectively. Here, only B_{z0} information is needed from the observation taken from the line-of-sight (LOS) or normal component of vector magnetogram, while B_{x0} and B_{y0} can be derived from $\tilde{B_{z0}}$,

$$\tilde{B_{x0}} = \frac{-ik_x}{k_z} \tilde{B_{z0}}, \tag{2.9}$$

$$\tilde{B_{y0}} = \frac{-ik_y}{k_z} \tilde{B_{z0}}. \tag{2.10}$$

Since the Fourier method was used in this study to extrapolate potential field, the side boundaries in the computational box will be periodic. It should be noted that this periodic boundary will be better to be applied to the magnetogram data with wide FOV, where AR is located in the center of the FOV and far from all the side boundaries. The surrounding field near the boundaries is also need to be weak to make sure that the potential field well captures the AR field and does not have essential connectivity with strong field near the boundaries. This assumption implies that the magnetic field lines that have connectivities across the side boundary walls are not reliable to be included in the analysis. Since we focus only in the AR field, particularly in the core region, we prefer to use such data in our study to fulfil the proper quality of the extrapolated field.

2.2.3 MHD Relaxation Method

We follow the MHD relaxation method of Inoue et al. (2014b) to reconstruct the coronal field of the active region we are interested in. We use vector magnetic field data obtained from the Hinode/SP magnetogram and SDO/HMI to reconstruct the coronal magnetic field. The potential field of the active region is calculated as an

initial condition from the normal component B_z of the vector magnetic field on the photosphere by using the Fourier method (Alissandrakis, 1981). The initial density is chosen to be uniform. After inserting the observed tangential components (B_x and B_y) into the bottom boundary, the magnetic field in the whole domain is then evolved towards the force-free state. This evolution process is governed by the set of equations for zero plasma beta,

$$\rho = \rho_0 \frac{|\mathbf{B}|}{B_0} \tag{2.11}$$

$$\frac{\partial \boldsymbol{v}}{\partial t} = -(\boldsymbol{v} \cdot \boldsymbol{\nabla})\boldsymbol{v} + \frac{1}{\rho}\boldsymbol{J} \times \boldsymbol{B} + \nu \boldsymbol{\nabla}^2 \boldsymbol{v}, \tag{2.12}$$

$$\frac{\partial \boldsymbol{B}}{\partial t} = -\boldsymbol{\nabla} \times (-\boldsymbol{v} \times \boldsymbol{B}) + \eta_{NLFF} \boldsymbol{\nabla}^2 \boldsymbol{B} - \nabla \phi, \tag{2.13}$$

$$\frac{\partial \phi}{\partial t} + c_h^2 \boldsymbol{\nabla} \cdot \boldsymbol{B} = -\frac{c_h^2}{c_p^2}\phi, \tag{2.14}$$

$$\boldsymbol{J} = \boldsymbol{\nabla} \times \boldsymbol{B}, \tag{2.15}$$

where ρ is the plasma density, $\boldsymbol{v}$ is the plasma velocity, $\boldsymbol{J}$ is the current density, and $\boldsymbol{B}$ is the magnetic flux density. In this method, Equation 2.11 defines a pseudo-density (ρ), which is proportional to $\mid \boldsymbol{B} \mid$, in order to ease the relaxation by maintaining the Alfvén speed in space (Inoue et al., 2013). Equation 2.12 is the equation of motion for the zero plasma beta condition neglecting gravity. The last term in the induction equation 2.13 includes the $\boldsymbol{\nabla} \cdot \boldsymbol{B}$ cleaning potential (ϕ). The cleaning potential equation 2.14 was introduced by Dedner et al. (2002) to reduce deviation from the solenoidal condition $\boldsymbol{\nabla} \cdot \boldsymbol{B} = 0$, where c_h and c_p are the coefficients related to advection and diffusion of $\boldsymbol{\nabla} \cdot \boldsymbol{B}$, respectively.

The magnetic field ($\boldsymbol{B}$) in the calculation is normalized by B_0, which equals to 4000 G. Velocity, time, and electric current density are normalized by $V_A \equiv B_0/(\mu_0\rho_0)^{(1/2)}$, $\tau_A \equiv L/V_A$, and $J_0 = B_0/\mu_0 L$, respectively. In the typical AR, $\rho_0 = 1.67 \times 10^{-12}$ kg/m^3, so that $V_A \approx 275$ Mm/s, $\tau_A \approx 0.8$ s, and $J_0 \approx 15$ μA/m^2. We set the coefficients following Inoue et al. (2014b), where c_p^2 and c_h^2 are 0.1 and 0.04, respectively. The non-dimensional viscosity (ν) in equation 2.12 is set as a constant (1.0×10^{-3}). Magnetic diffusivity (η) in equation 2.13 is defined as

$$\eta_{NLFF} = \eta_0 + \eta_1 \frac{\mid \boldsymbol{J} \times \boldsymbol{B} \mid\mid \boldsymbol{v} \mid^2}{\mid \boldsymbol{B} \mid^2}, \tag{2.16}$$

where $\eta_0 = 5.0 \times 10^{-4}$ and $\eta_1 = 1.0 \times 10^{-3}$ are non-dimensional parameters in the units of $\mu_0 V_A L$ and $(\mu_0 L)^2/V_A$, respectively.

At the bottom boundary, once we run the program, the tangential components from the potential field are incrementally changed into the observed tangential components. After the bottom boundary values of magnetic vector field are completely changed into the observed values, we set all the physical values for the bottom boundary to be fixed during the calculation. For the side boundaries, we fix all the physical parameters in the y-direction while periodic in the x-direction. The method for the NLFFF extrapolation and parameter setting in this work are little different to the NLFFF method by Inoue et al. (2014a), which all the boundaries are fixed and the initial potential field was reconstructed using Green's function method. The visualizations of NLFFF and simulation fields were produced by VAPOR (Clyne et al., 2007; Clyne and Rast, 2005).

Chapter 3

MHD Simulation of X3.4 Flare Trigger Mechanism in AR 10930

3.1 Introduction

Solar flare has been generally thought since a long time to be a result of the release of free magnetic energy contained in the active region (Gold and Hoyle, 1960; Parker, 1963; Aly, 1985). The free energy can be stored as a result of the shear or twist of magnetic field near the PILs (Moore et al., 2012; Falconer et al., 2008). It is also observed in many eruptive active regions that some sigmoidal structures formed across the active region before a flare or CME occurred (Canfield et al., 1999; Gibson et al., 2006). The sigmoidal structure basically shows that strong shear and twist exist in the active region. When an active region with high shear or twist occurs in the Sun, a small perturbation is likely to trigger the eruption of the sheared or twisted magnetic structures in this active region.

[2]This chapter has been published in the Astrophysical Journal, 842:86 (11pp), 2017 June 20, and available in http://doi.org/10.3847/1538-4357/aa750e. Some modifications have been made to adjust the format and content of this thesis.

Several theories have been proposed to explain the triggering of solar flares. It is possible that the trigger process is related with converging flows (Inhester et al., 1992), emerging flux (Heyvaerts et al., 1977; Choudary et al., 1998; Louis et al., 2015), or reverse-shear magnetic field (Kusano et al., 2004), which can affect the stability of the coronal magnetic field. Flare is also related to the formation and eruption of a large scale flux rope that can be caused by converging and shearing motion (van Ballegooijen and Martens, 1989), flux cancellation (Wang and Shi, 1993), or current carrying emerging flux (Wang et al., 1994).

In the tether cutting scenario, reconnection of strongly sheared field below the magnetic arcades can trigger the eruption (Moore et al., 2001). Kusano et al. (2012) proposed that two particular types of emerging fluxes can initiate the reconnection in the tether cutting scenario. On the other hand, Antiochos et al. (1999) proposed the magnetic breakout model where reconnection occurs due to the interaction of the magnetic field with the overlying arcades at the null points (Aulanier et al., 2000; Sun et al., 2013) or at bald patches (Wang et al., 2002). By using data-driven simulation, Jiang et al. (2016) suggests that some jet-like reconnection can trigger the eruption, which corresponds to the breakout model. Moreover, according to MHD theory, solar flare can be thought to be triggered by the MHD instabilities, e.g., by torus instability (Kliem and Török, 2006; Démoulin and Aulanier, 2010) or kink instability (Hood and Priest, 1979; Török et al., 2004) when the critical condition for the instability is obtained. These theories provide the mechanism for the free magnetic energy to be released as the kinetic energy and heat energy.

The understanding of the flare trigger mechanism is crucially important to realize better prediction of when, where, and how flares will occur. However, in order to do that, one needs to be able to measure how stable the active region is, to determine whether it has enough free energy to be released, and to define the probability of flare. Therefore, it is necessary to study the flare trigger mechanism based on the observation and simulation. Previous flare simulation studies have been conducted to reveal the physical mechanism of solar flares, e.g. Yokoyama and Shibata (1998);

Aulanier et al. (2010); Fan et al. (2011); Kliem et al. (2010); Amari et al. (2014). From the MHD simulation in 2-D, Yokoyama and Shibata (1998) suggested that magnetic reconnection in a flare can lead to a chromospheric evaporation. By using zero-β MHD simulation Aulanier et al. (2010) and Kliem et al. (2010) showed that solar flares can happen due to the ideal MHD instability. Fan et al. (2011) performed MHD simulation of the X3.4 solar flare from the AR NOAA 10930 using highly smoothed observed magnetogram data of the AR obtained by Hinode satellite. Recently, Amari et al. (2014) performed data-constrained MHD simulation to the same AR with higher spatial resolution and found that MHD simulation can be a powerful tool to study the flare trigger mechanism.

Systematic studies of the flare trigger mechanisms have been performed by Kusano et al. (2012). They carried out ensemble MHD simulations with different LFFFs and small bipole structures with different orientations imposed onto the LFFF. From their study, magnetic structures as well as the orientation of the bipoles which are effective in triggering a flare can be identified. They found that solar eruptions can occur as a result of both strong shear of the large-scale magnetic field near the PIL and the proper disturbance of the magnetic fields. The proper disturbances proposed in their study are the opposite polarity (OP) and the reversed shear (RS) structures. Opposite polarity refers to the small bipole structure whose polarity is opposite with respect to the polarity of the large-scale field structure at the PIL. Reversed shear polarity refers to the small bipole structure which is directed nearly opposite to the shear component of the field. In order to examine the model of the solar flare trigger mechanism proposed by Kusano et al. (2012), several observational analyses of flare events have been conducted by using Hinode (Kusano et al., 2012; Bamba et al., 2013; Toriumi et al., 2013), SDO (Bamba et al., 2014), SOHO/MDI (Park et al., 2013), and New Solar Telescope (NST) data (Wang et al., 2017). From their results, several flare events can be explained to occur as a result of the flare trigger mechanism proposed in Kusano et al. (2012).

However, the configurations of magnetic fields in the Sun are much more complex

than the LFFF structures used in the study by Kusano et al. (2012). Due to the complexity of their structure, actual solar magnetic fields are very difficult to be reconstructed by this approach. For enabling this idea of solar flare trigger in the practical use of space weather forecasting, we need to use the concept of the solar flare trigger in more realistic coronal structure. For this purpose, here we study the flare trigger mechanism by Kusano et al. (2012) with more realistic NLFFF magnetic field structures based on the observational data. Moreover, the goal of this study is to reveal which magnetic field configurations are effective for triggering a flare. Through this study, we aim at contributing to the improvement of flare prediction for space weather forecast.

Here we show and discuss the results of the MHD simulations for different configuration of small magnetic structures imposing in the NLFFF model of active region (AR) NOAA 10930 prior to the eruption of X3.4 flare in 2006 December 13. The NLFFF extrapolation method has been described in Chapter 2. The overview of AR 10930, MHD simulation scheme, and results are described in the following sections, respectively. We also discuss and conclude how the reconstructed flare ribbon can be used to determine the flare trigger structure by comparing it with the observations.

3.2 Overview of AR 10930

In this work, we used AR NOAA 10930 as a case study for our simulation. This active region was bipolar with the negative polarity spot larger than the positive polarity spot. It was very active since it produced at least 113 X-ray flares of different energy from 2006 December 4 to 2006 December 18 (Gopasyuk, 2015). Here, we focus on the X3.4 class solar flare which occurred at 02:14 UT on 2006 December 13. Many studies of this active region have been extensively conducted on various aspects, i.e. sheared field (Kubo et al., 2007; Su et al., 2007), helicity and twist (Magara and Tsuneta, 2008; Inoue et al., 2011; Su et al., 2009), rotating sunspot (Min and

Chae, 2009; Gopasyuk, 2015), NLFFF extrapolation (Schrijver et al., 2008; Inoue et al., 2012), and MHD simulation (Fan et al., 2011; Amari et al., 2014). Sigmoidal structure has been reported to appear both from the observation as well as NLFFF extrapolation (Min and Chae, 2009; Inoue et al., 2012; Amari et al., 2014).

Large negative polarity as well as the positive polarity both rotated and led to the formation of twisting magnetic field lines and created sigmoid (Min and Chae, 2009). This sigmoid was also reproduced in the NLFFF extrapolation of this AR, which shows that strong current density and magnetic energy were accumulated in the core of the AR (Schrijver et al., 2008; Inoue et al., 2012). The AR has predominantly negative helicity and it is confirmed by the azimuthal components of the sunspot that has negative sign (Gopasyuk, 2015; Su et al., 2009). The Poynting flux of the AR evolved dynamically, which was associated with the emerging flux and the rotation motion happened in the AR (Fan et al., 2011). Wang et al. (2008) found that magnetic channels existed in the middle of the large main positive and negative polarities of the AR, which are associated with the emerging flux. They found that this emerging flux might be the precursor of the X3.4 flare happened from the AR.

3.3 MHD Simulation and Numerical Scheme

We used vector magnetic field of AR 10930 derived from the Spectro Polarimeter (SP) data of the SOT instrument (Tsuneta et al., 2008) on-board the Hinode satellite (Kosugi et al., 2007) for the NLFFF extrapolation. We used Ca II H line (3968.5 Å) data from the Broadband Filter Instrument (BFI) in the SOT for the purpose of examining how well the NLFFF and MHD simulation results agree with the structure of the flare ribbons. The X-ray image of the AR 10930 was obtained from the XRT on-board Hinode (Golub et al., 2007). This image is important to compare the NLFFF results with the coronal magnetic field configuration inferred from the X-ray image.

We inserted vector magnetogram data obtained from the Hinode/SP as a bottom boundary condition from the original 1000×512 pixels in order to fit to the $240 \times 128 \times 128$ uniform grid used in the simulation box. The magnetogram's field-of-view is 297×163 arcsec, corresponding to 214×118 Mm on the Sun. The simulation box represents the rectangular domain of $(-0.5L, -0.25L, 0) \leq (x, y, z) \leq (0.5L, 0.25L, 0.5L)$, where L is the normalization of the spatial length, which has the actual value of about 214 Mm. We then extrapolated the coronal magnetic field by using MHD relaxation method described in the previous chapter.

The MHD simulation is performed in the same grid as the NLFFF extrapolation. It uses the NLFFF model and the corresponding density as the initial conditions. The non-ideal zero-beta MHD equations are solved in the MHD simulation. Hence, the induction equation now takes the form

$$\frac{\partial \boldsymbol{B}}{\partial t} = -\boldsymbol{\nabla} \times (-\boldsymbol{v} \times \boldsymbol{B} + \eta_{MHD} \boldsymbol{J}), \tag{3.1}$$

and the continuity equation,

$$\frac{\partial \rho}{\partial t} = -\boldsymbol{\nabla} \cdot (\rho \boldsymbol{v}), \tag{3.2}$$

replaces equation 2.11. The magnetic diffusion (η) in equation 2.16 is defined as an anomalous resistivity following Inoue et al. (2014a),

$$\eta_{MHD}(t) = \begin{cases} \eta_2, & J \leq j_c \\ \eta_2 + \eta_3 \left(\frac{J - j_c}{j_c} \right), & J > j_c, \end{cases} \tag{3.3}$$

where $\eta_2 = 1.0 \times 10^{-5}$, $\eta_3 = 5.0 \times 10^{-3}$, and the threshold current density, $j_c = 300$. This anomalous resistivity can be expected to enhance the reconnection of the field lines in the regions of strong current (Inoue et al., 2014a).

Kusano et al. (2012) suggested that the trigger structure is located near the photospheric PIL. Accordingly, we expect the area near the PIL of the core field to be particularly effective for triggering a flare. According to Bamba et al. (2013), the

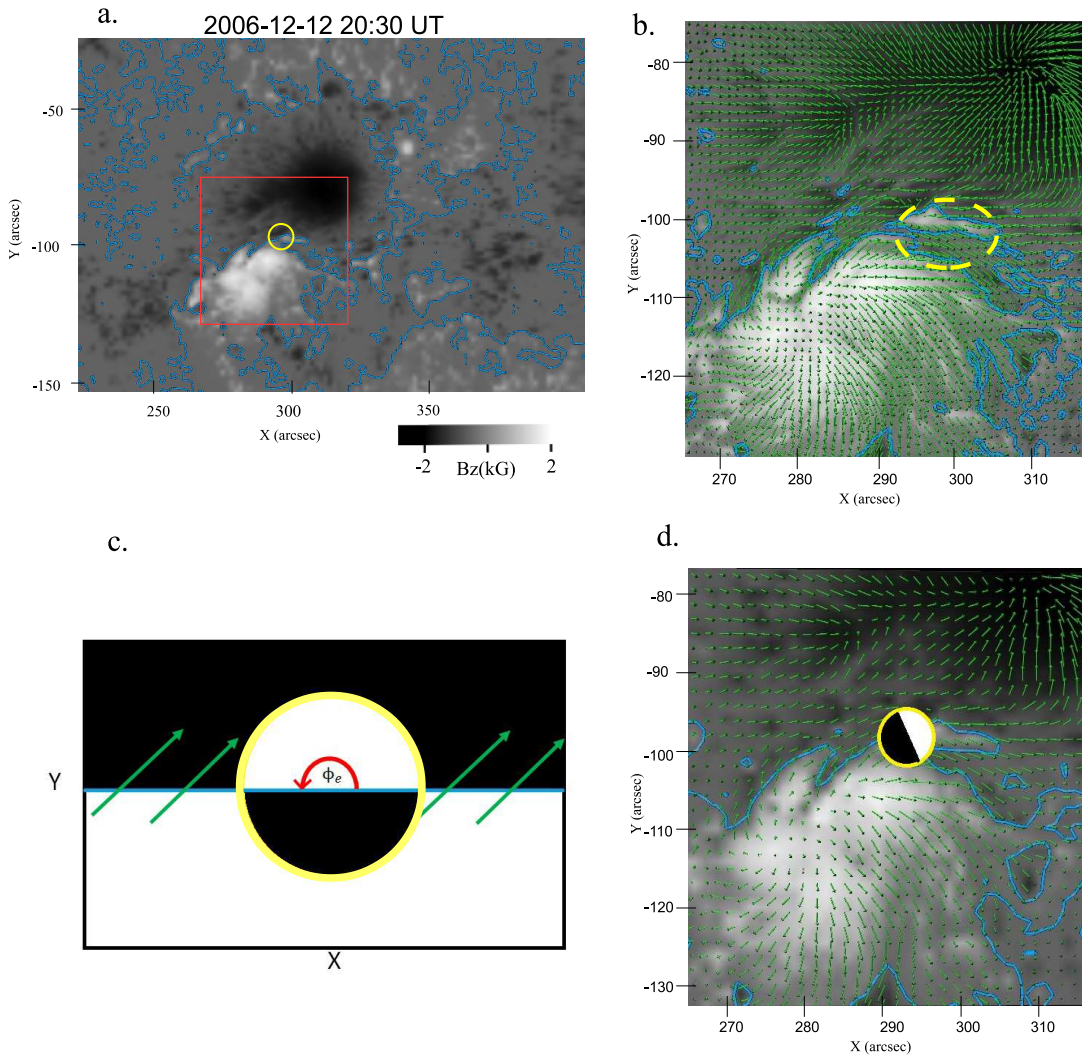

FIGURE 3.1: (a)Distribution of the normal component of AR 10930 vector magnetic field, B_z, on the bottom of the simulation box. White and black is positive and negative polarity, respectively. Blue contour is the polarity inversion line and yellow circle marks the area where the bipole field is injected. (b)Vector magnetic field map obtained from Hinode/SP magnetogram data on 2006-12-12 20:30 UT overplotted on the normal component of vector magnetic field for the area within the red box in (a). The dashed yellow ellipse shows the presence of OP-type magnetic island. (c)Orientation of the azimuthal angle ϕ_e of the emerging flux (bipole field) on the X-Y plane as seen in the top view of the simulation box. Green arrows represent the background transverse magnetic field. (d)Enlarged view of the red box in (a) with the vector magnetic field map for the binned data used in the bottom boundary of the simulation box. The yellow circle shows the orientation of the imposed bipole flux when it stops to ascend in the simulation run with $\phi_e = 110°$.

trigger structure of the X3.4 flare studied here was situated in the area marked by the yellow circle in Figure 3.1(a). They showed that a highly sheared structure existed along the PIL and that a small positive polarity magnetic island grew near the PIL as is shown in Figure 3.1(b). This location was obtained from their study of the topological features of the flare ribbons and their associated highly sheared structure. They found that the emerging flux of the magnetic island, which was located between the flare ribbons, triggered the X3.4 flare six hours after this magnetogram was taken. The orientation of the bipole flux was opposite to the orientation of the large-scale magnetic field of the active region, and thus it could lead to the eruption of the sheared or twisted magnetic field lines by introducing the reconnection which formed and destabilized the flux rope. Therefore, we chose this location as the place where the small bipole structure is injected as flux that emerges into the initial field in our simulation to trigger the eruption.

The emerging flux model follows the method of Kusano et al. (2012), where the small bipole is made from a magnetic torus that ascends from below the simulation box. The bipole structure is a sphere with radius r_e filled with a purely toroidal field of uniform strength, B_e. An electric field $\boldsymbol{B}_e \times \boldsymbol{v}_e$ is imposed in the cross-section of the bottom plane to let the torus ascend with velocity v_e, chosen to be constant during the period $0 \leq t \leq \tau_e (= r_e/v_e)$. The injected bipole structure has the azimuthal orientation angle, ϕ_e, defined as shown in Figure 3.1(c). The bipole is injected at the coordinate $P(x = 294, y = -98)$ arcsec and has a magnetic intensity, $B_e = 15$ and a radius, $r_e = 0.01$. It starts to ascend with the constant velocity $v_e = 0.02$ at $t = 0$, and is stopped at $t = \tau_e = 0.5$ when the center of the sphere reaches the bottom plane. This velocity is higher than the typically observed photospheric velocities, but still slower than the coronal Alfvén velocity and, therefore, appropriate for the problem studied here. We perform simulations with various angles ϕ_e. Eight cases are run as summarized in Table 1. Case C ($\phi_e = 110°$) is displayed in Figure 3.1(d).

Based on its orientation with respect to the pre-existing field, the bipole configurations imposed in our simulations can be classified as right polarity ($\phi_e \approx 0°$), reversed

TABLE 3.1: Azimuth angle (ϕ_e) and total reconnected flux (Φ_{rec}) in the area of the red square in Fig. 1 for the different cases performed in the simulations, estimated from the flux covered by field lines with a large displacement $\Delta x(x_0)$. The values are normalized by $\Phi_0 \equiv B_0 L^2 = 1.83 \times 10^{24}$ Mx.

Run Case	Orientation (ϕ_e)	Φ_{rec}
A	10°	2.44×10^{-4}
B	50°	4.68×10^{-4}
C	110°	6.2×10^{-4}
D	135°	6.27×10^{-4}
E	180°	8.12×10^{-4}
F	225°	4.81×10^{-4}
G	270°	2.14×10^{-4}
H	315°	1.29×10^{-4}

shear ($\phi_e \approx 90°$), opposite polarity ($\phi_e \approx 180°$), and normal shear ($\phi_e \approx 270°$) type, using the terms introduced by Kusano et al. (2012). RS type configuration is defined as the bipole flux whose orientation is almost oppositely directed to the shear (non-potential) field component. Here we define the RS-type to be the bipole with $\phi_e \approx 90°$ because the shear field in the area around the PIL has left-handed twist so that the magnetic helicity is negative. The left-handed shear and twist can be seen from the reverse S shape of the sigmoid and from the angle between the threads of the sigmoid and the PIL. This was confirmed by a computation of twist map by Inoue et al. (2012). OP type, on the other hand, is defined as the bipole structure with the orientation almost opposite to the averaged potential field.

The constraint for the tangential components of magnetic field on the top and bottom boundaries is set to be released during the simulations, whereas the normal components are fixed except for the area where the bipole flux is emerging. At the side boundaries, all physical values are fixed during the simulations in the y-direction and periodic in the x-direction. Due to the relatively small size of the numerical box and the fixed side boundary conditions, we cannot expect that the simulation will produce a large expansion of the field such as CME. We only focus on the dynamics of the beginning phase of the flare process.

It should be noted that there are some assumptions made in this simulations. First, the emerging flux imposed in the simulation was much stronger than the surrounding field that was not the case in the real AR. The preference of such a strong field to be imposed was to facilitate the possibility of eruption based on the trial and error process. We noticed that it seems there was a minimum limit of the emerging flux that could trigger a flare. However, we did not investigate this minimum limit that we believed mainly depend on the grid size used in the simulation. However, we found that even using the high flux density value for the emerging flux in the simulation did not guarantee that the eruption (flare) could be triggered. We found that the most important parameter that could trigger a flare was the orientation of emerging flux, as we described in the following result section. Therefore, it should be noted that this study mainly focus on the topological analysis of the field and not to study the dynamics of the eruption. Second, the velocity of the emerging flux was faster than the real emerging flux. This fast emerging flux would allow the whole process of eruption to be faster than the real flare. Again, it should be noted that this study mainly focus on the topology of the field. Since the magnetic field and the length scale is normalized by large values, the time scale in the simulation also represents large value. In the real coronal field, where the flux density is only in the order of 1 percent of the normalisation value in this study, the typical speed is also about 1 percent of the typical speed in this simulation. Therefore, one unit of the time in the simulation represents about 100 s.

3.4 Results

The top view of field lines in the NLFFF model, plotted over normal component of the magnetogram data, is shown in Figure 3.2(a). It shows that open magnetic field dominates the active region in the area within and surrounding the negative polarity. This is due to the imbalance of the flux between the negative and positive polarities in the active region. The coronal magnetic field is closed in the area surrounding

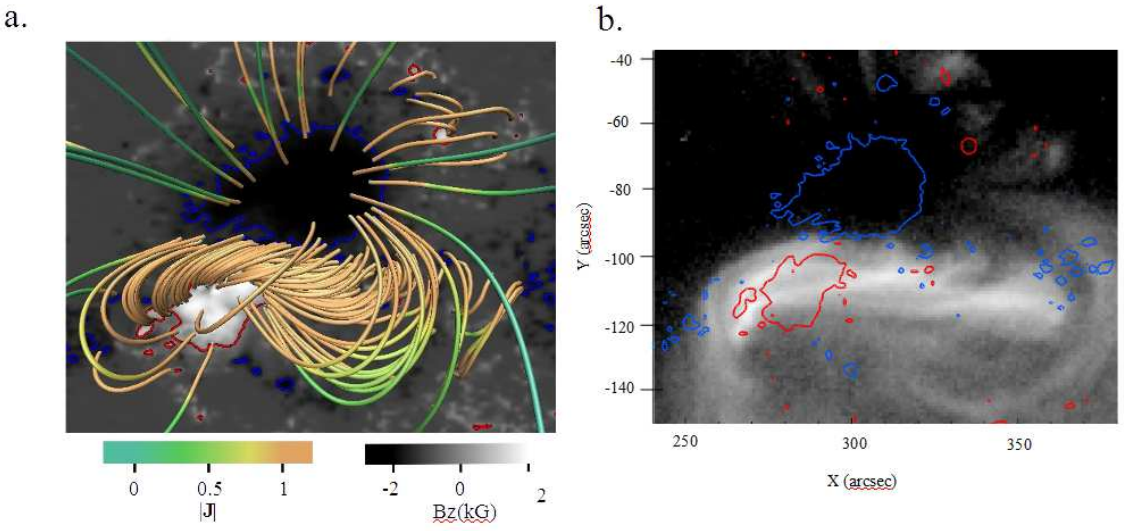

FIGURE 3.2: (a) NLFFF model of AR 10930 overplotted on the background image of B_z, with the blue and red contours showing the -800 G and 800 G levels of the B_z, respectively. Field lines are plotted with a color representing current density. The field lines with strong current density form a sigmoidal pattern. (b) The same contours of B_z plotted on the X-ray image observed by Hinode/XRT on 21.00 UT, which shows a sigmoidal structure that corresponds to the core-field in the NLFFF model.

the PIL. We call this the core field of the AR. As shown in Figue 3.2(a), the core field shows a strong shear, which can also be seen in the photosphere (Figure 3.1(b) and (d)).

The extrapolated NLFFF is strongly sheared particularly on the lower part of the corona. This core field may contain a large amount of free energy, since it differs strongly from the potential field. The comparison with X-ray image taken by the XRT instrument onboard Hinode (Figure 3.2(b)) shows that the NLFFF model agrees well with the observation in terms of the presence of high shear at the PIL. Moreover, the NLFFF model infers that the sigmoidal structure at the PIL consists of short arcade-type field lines (Figure 3.2(a)). This sigmoidal structure is important because it shows that the core field of the AR is highly sheared (Su et al. 2007; Min & Chae 2009). The reverse-S shape is well reproduced in the NLFFF extrapolation used here as well as in several previous works by Inoue et al. (2012) and Amari et al.

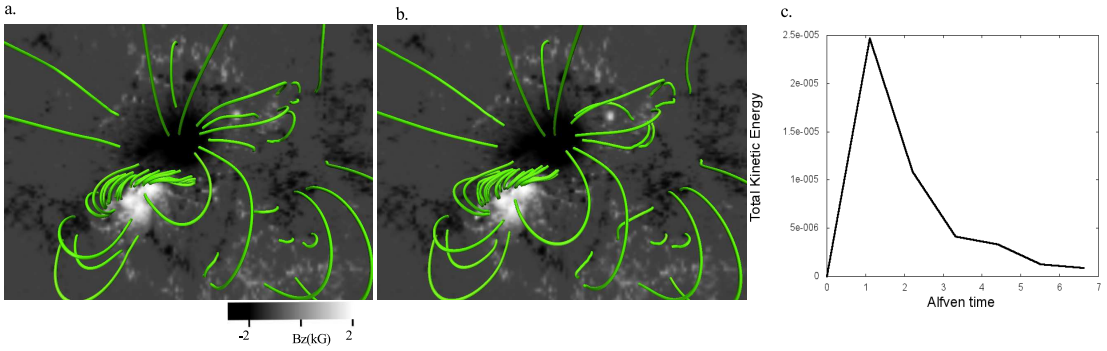

FIGURE 3.3: Magnetic field of AR 10930 in the same area as Figure 3.2(a) for the simulation without emerging flux at (a)t=0 and (b)t=3.3. The kinetic energy in the box is plotted in (c).

(2014).

As a reference case, we first carry out a simulation without imposing any external perturbation. This simulation is performed to show the nature of the system if there is no emerging flux imposed. It is verified that the residual Lorentz force in the NLFFF model is too weak for triggering an eruption (Figure 3.3(a) and (b)). The simulation shows that the shear of the magnetic field slightly weakens under the condition of the released tangential field components in the bottom boundary, as shown in Figure 3.3(b). It is easy to understand that the magnetic field will naturally relax to a lower-energy state which is toward the potential field configuration. This verifies that any eruption of the NLFFF must be driven by an external disturbance. The relaxation to a stable equilibrium state can also be seen from the evolution of the kinetic energy in the box in Figure 3.3(c), where a brief initial rise (due to the residual Lorentz force in the initial condition) is followed by a monotonic decrease (similar to Run B in Inoue et al. (2014a)).

We find that several configurations of the trigger structure can lead to an eruption; these are the structures in cases C, D, E, and F. However, each type of triggering structure creates a different dynamics and topology of the erupting flux rope. Here we carefully analyze the eruption of the flux ropes in our simulations to clarify the typical dynamics involved in the erupting process. Based on the relation between

flare reconnection and flux rope formation, all eruptive cases in our simulation can be categorized into two distinct groups, which are "eruption-induced reconnections" and "reconnection-induced eruptions". The former is the case when the flux rope is formed before the flare reconnection occurs. In this case, the emerging bipole flux triggers the creation of an unstable flux rope through pre-flare reconnection. Subsequently, the flare reconnection is generated below the flux rope during its eruption. As for the latter, the role of the emerging bipole is to trigger the reconnection between pre-existing magnetic field by reducing the shear of the overlying field which then creates an unstable flux rope. These two types of dynamical process were also observed in the simulations conducted by Kusano et al. (2012).

3.4.1 OP-type Cases

Eruption-induced reconnection features are clearly observed in the simulation results for Case E ($\phi_e = 180°$) and Case F ($\phi_e = 225°$). However, although they share some common features of eruption-induced reconnection, each case has its own characteristics of the topological structure, due to the difference in the azimuthal angle of the bipole. Figures 3.4(a)-(d) show the evolution of the eruption-induced reconnection from the initial condition until the expansion of sigmoidal flux ropes. At the beginning (Figure 3.4(a)), the magnetic field lines do not form any large twisted flux rope. After the small bipole structure emerges in the photosphere, it starts to reconnect with the pre-existing field and forms a flux rope with sigmoidal shape (Figure 3.4(b)). The flux rope, then acquires a higher twist (Figure 3.4(c)) and expands outward (Figure 3.4(d)). Figures 3.5(a)-(b) show the detailed dynamics of the eruption-induced reconnection seen from a different point of view. When the bipole flux emerges, a flux rope occurs immediately after the reconnection of the magnetic field near the PIL via the OP-type structure, and high electric current regions (shown by red shade) are formed (Figure 3.5(b)). This reconnection tends to create a large flux rope with high twist (yellow lines in Figure 3.5(c)) that quickly

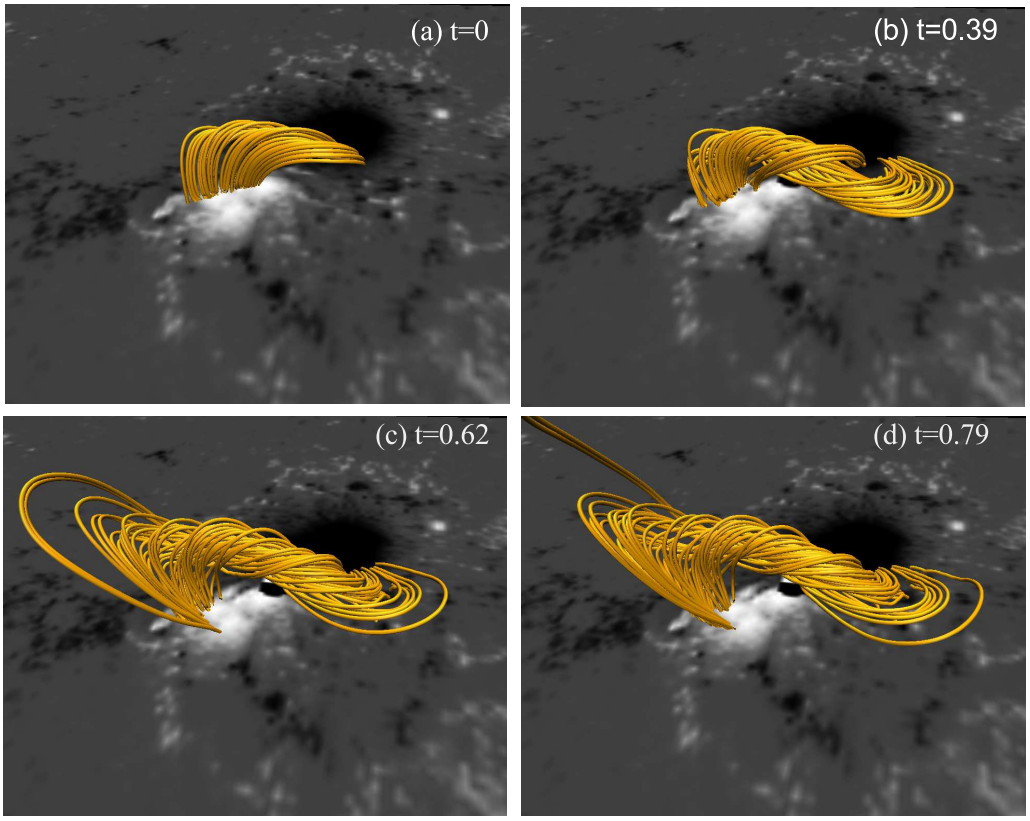

FIGURE 3.4: (a)-(d) Bird eye view of the time evolution of the core magnetic field (gold lines) for Case E with imposed bipole azimuth angle ϕ_e=180°.

erupts, as can be seen in Figure 3.5(d), where the flux rope lifts the overlying field and finally induces flare reconnection below the flux rope.

3.4.2 RS-type Cases

In Cases C and D, the process of the eruption follows reconnection-induced eruption scenarios found in Kusano et al. (2012). Figure 3.6(a)-(d) show the evolution of the reconnection-induced eruption for Case C. At the first step, the core magnetic field near the PIL reconnects with the RS structure bipole (Figure 3.6(b)). Subsequently, the overlying field at the center of the RS structure collapses (Figure 3.6(c)) and starts to create a large flux rope (Figure 3.6(d)). Figures 3.7(a)-(b) show the detailed

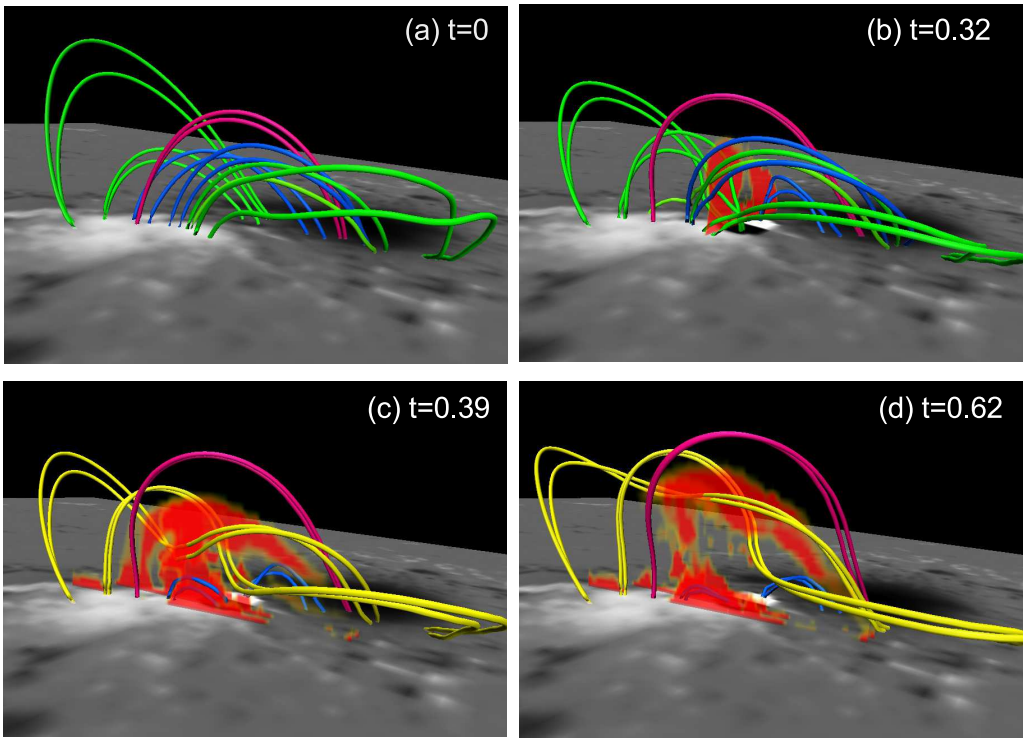

FIGURE 3.5: Dynamics of eruption-induced reconnection caused by the OP-type structure of emerging flux for Case E: (a) the initial state, (b) after the bipole flux is injected, (c) after the flux rope starts to appear, and (d) when the flux rope erupts. Green lines show the field lines before the flux rope is formed by reconnection with the OP-type bipole field. Blue lines show the magnetic field lines which changed their connectivity due to the reconnection with the imposed OP-type structure. Purple lines show the magnetic field lines which retain the same connectivity. Yellow lines show the created flux-rope due to the reconnection between green lines in (a) and (b). The red areas show enhanced current density with $|\mathbf{J}| > 30$.

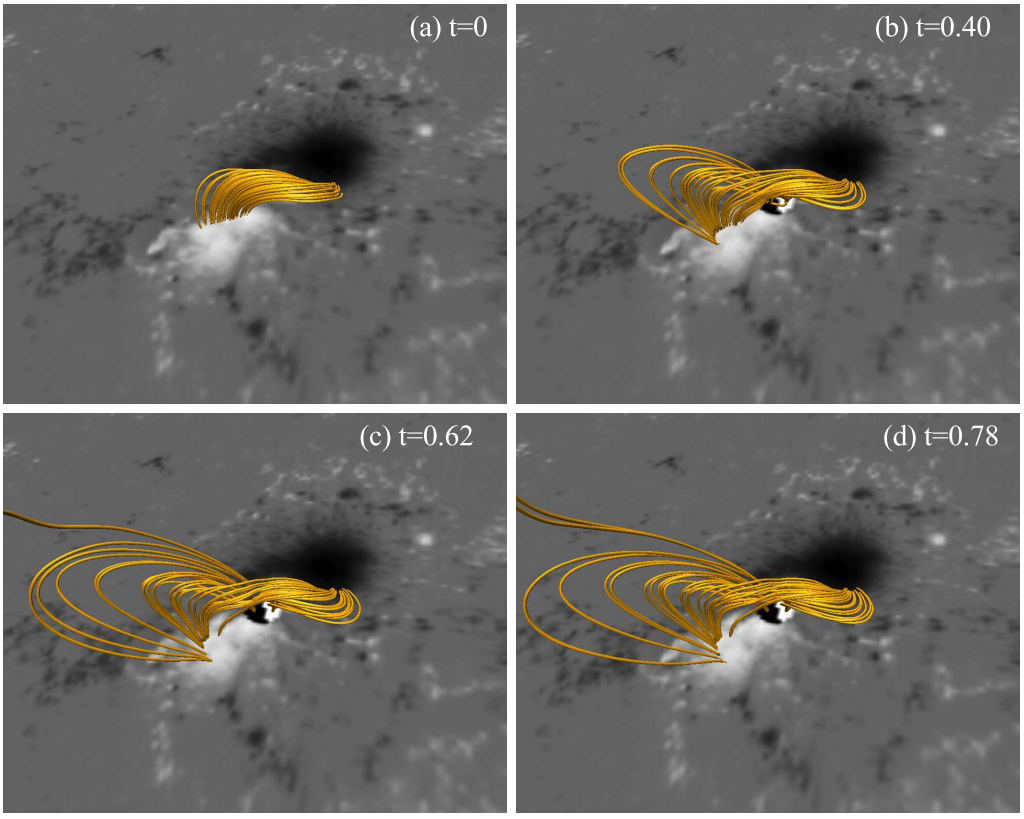

FIGURE 3.6: (a)-(d) Bird eye view of the time evolution of the core magnetic field for Case C with imposed bipole azimuth angle $\phi_e = 110°$.

dynamics of flux rope formation in the reconnection-induced eruption seen from a different point of view. Just after the bipole emerges, some of the pre-existing field lines near the PIL (blue lines in Figure 3.7(b)) are in contact with the bipole field and create a current sheet. This reconnection reduces the sheared field (blue lines), which causes the overlying field to collapse toward the center. Part of the collapsed field finally reconnects with the bipole structure (green lines in Figures 3.7(c)-(d)). However, the higher overlying field tends to form a flux rope, which then erupts upward, as shown by the yellow lines in Figure 3.7(d). The topological structure of these steps in the present simulation is consistent with the previous simulation by Kusano et al. (2012) although it is more difficult to observe compared to the previous simulation. This is due to the more complex configuration of the real

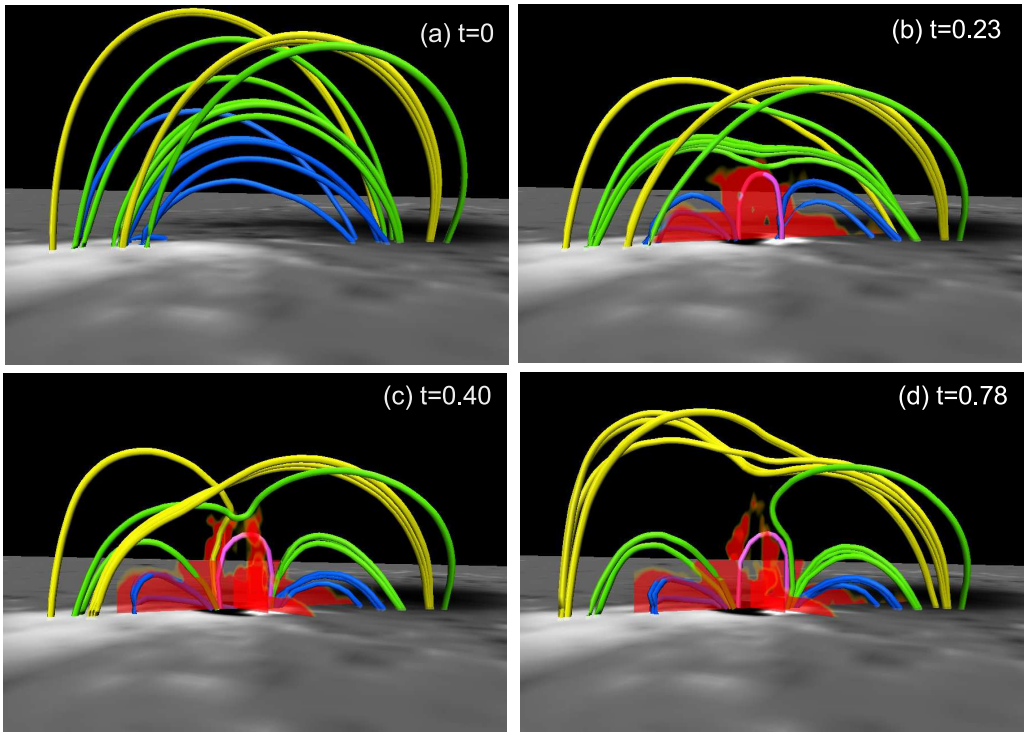

FIGURE 3.7: Dynamics of reconnection-induced eruption caused by RS-type structure for Case C: (a) the initial state, (b) after bipole flux is injected, (c) during the formation of the flux rope, and (d) when the flux rope erupts. Blue lines show the magnetic field lines which changed the connectivity due to the reconnection with the imposed RS-type structure. Green lines show the magnetic field lines which collapsed to the center of the RS-type structure and then finally reconnected with the imposed RS-type structure. Yellow lines show the magnetic field lines that created the flux rope. Red areas correspond to intense current density layers with $|\mathbf{J}| > 40$.

coronal magnetic field rather than a symmetric structure by the initial boundary condition of LFFF in the Kusano et al. (2012) simulation. All of these steps are also observed in Case D.

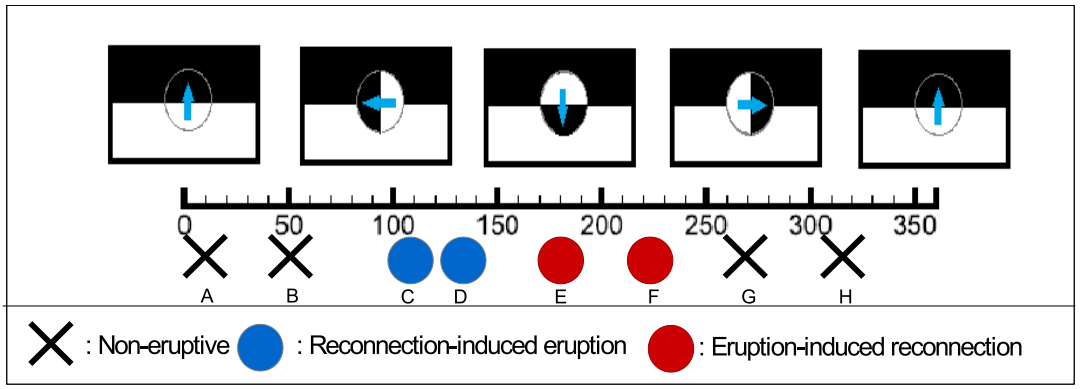

FIGURE 3.8: Summary of the simulations for Cases A-H and the classification of the events based on the eruptive behavior and trigger structure. The upper panels show the orientation of the emerging bipole structure and the corresponding azimuth angle.

3.4.3 Comparison with observations

From the simulation results we find that the azimuthal angle of the bipole structure plays a very important role in determining the overall dynamics of the magnetic field. Some imposed bipole structures clearly are not effective in triggering a flare, while some others are very effective in triggering a flare, with some aspects of the evolution also depending on the azimuth angle. A summary of the simulation results is shown in Figure 3.8. It is found that the events that do not show any eruptive characteristics are the cases where the imposed emerging flux is oriented relatively parallel to the potential or shear (non-potential) components of the pre-existing magnetic core field at PIL. In our simulations, these are the cases A, B, G, and H with $\phi_e = 10°$, $50°$, $270°$, and $315°$, respectively. Otherwise, an eruption is triggered.

Flare ribbons can well represent the topology of the reconnecting magnetic field, so that they can be used to check the results of the simulations. The ribbons mark the footpoints of magnetic field lines that reconnect during the flare. A proxy for flare ribbons in the simulations is made by following the method introduced by Toriumi et al. (2013) and applied also in Inoue et al. (2014a). We calculate the total displacement of the footpoint for each field line for a given time and consider field

lines with a large footpoint displacement to be reconnected ones. We trace each magnetic field line from each point ($\mathbf{x_0}$) in the bottom plane and identify the end point of the field line $\mathbf{x_1}(\mathbf{x_0}, t_0)$. Here, the end point position $\mathbf{x_1}$ as a function of start point $\mathbf{x_0}$ and time t_n is denoted as $\mathbf{x_1}(\mathbf{x_0}, t_n)$. After some time, we trace again the end point of the field line ($\mathbf{x_1}(\mathbf{x_0}, t_n)$) from the start point ($\mathbf{x_0}$). Therefore, the displacement of the end point position for one start point $\mathbf{x_0}$ is given by

$$\delta(\mathbf{x_0}, t_n) = |\mathbf{x_1}(\mathbf{x_0}, t_{n+1}) - \mathbf{x_1}(\mathbf{x_0}, t_n)|. \tag{3.4}$$

By integrating δ for a given time, $t = t_N$, we can obtain the total displacement of the end point from the initial state to an arbitrary time step,

$$\Delta x(\mathbf{x_0}, t) = \sum_{n=0}^{N} \delta(\mathbf{x_0}, t_n). \tag{3.5}$$

We assume that the high value of total displacement (Δx) is due to reconnection. Synthetic flare ribbons are constructed by plotting the value of the total displacement of all field lines as a function of their footpoint position on the bottom plane. The results are shown in Figure 3.9 for the eight different cases. In order to emphasize the distribution of the flare ribbons, we only plot footpoints with the total displacement exceeding 0.04. We also calculate the total reconnected flux of B_z from the areas within the red square in Figure 3.1(a) that show a large displacement of field lines and denoted this as Φ_{rec} in Table 3.1. These total fluxes show how much flux reconnects when the emerging flux meets the condition of a flare trigger.

It is obvious from Figure 3.9 that the flare ribbons constructed from the simulations are different in each case. This suggests that the topology of the reconnected magnetic field is unique for each case. Therefore, the dynamics of the magnetic field due to the interaction between the pre-existing magnetic field and the emerged bipole structure depends considerable on the orientation of the bipole. The results also show that the topology of the magnetic field involved in the eruption process triggered by the RS and OP type structures differs, even though both cases end up

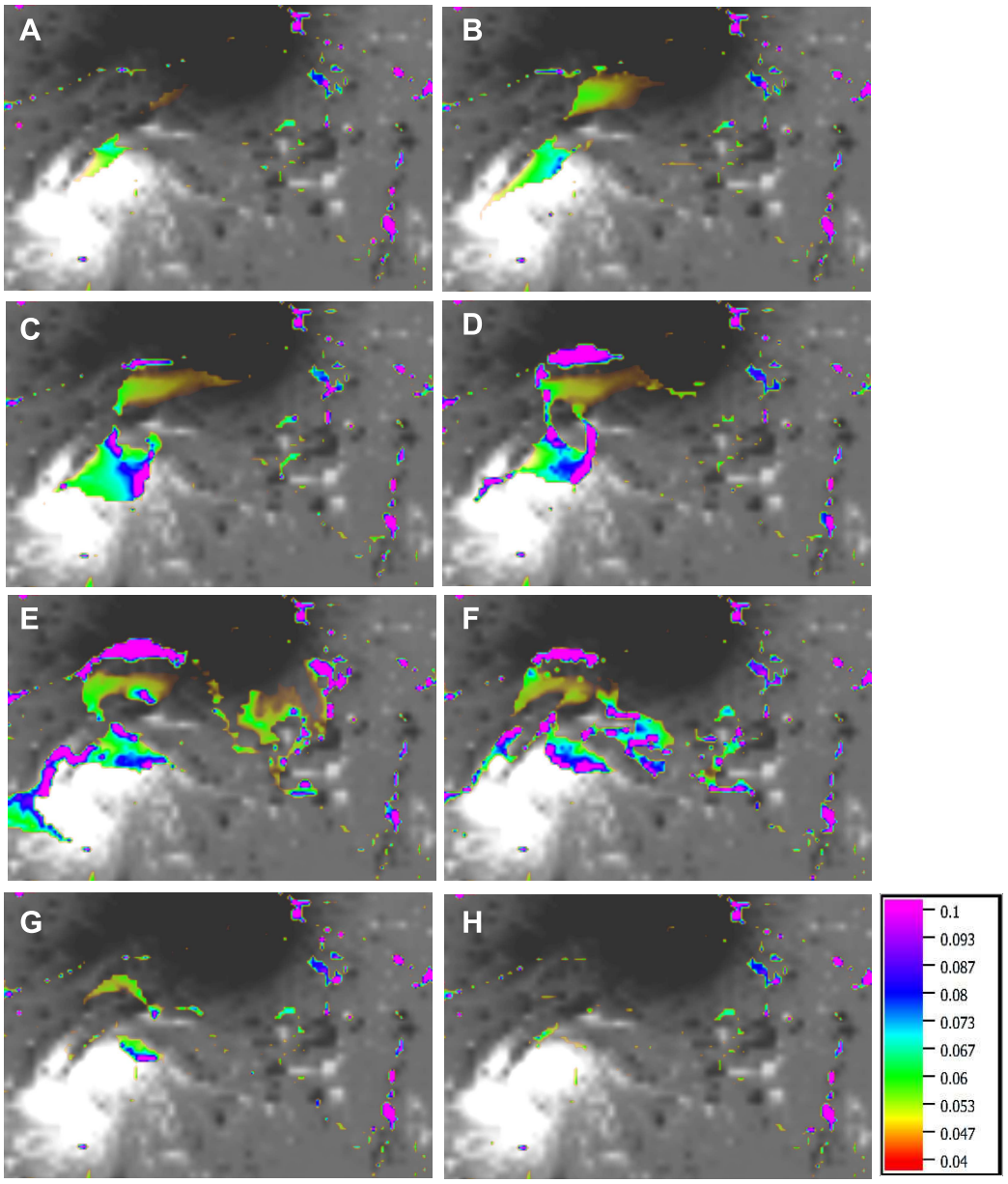

FIGURE 3.9: Synthetic flare ribbons constructed from the simulations at t=0.5, plotted over the normal component of the magnetic field for case A-H. The color bar shows the total displacement of the field line footpoints derived from equation 3.5.

with eruption. The RS-type structure (Case C and Case D) tends to produce local flare ribbons in the area of the core-field of the active region. On the other hand, the OP-type structure (Case E) can generate more extended flare ribbons of more complex structure.

3.5 Discussions

3.5.1 Trigger Mechanism

From the results of all cases in our simulation, we can classify each case of the simulation in three different categories: non-eruptive events, reconnection-induced eruption events, and eruption-induced reconnection events. In the non-eruptive cases, the small imposed bipole structure is relatively parallel to the potential or shear components of the average vector magnetic field of the large bipolar spots of AR 10930. It can be easily understood that in such kind of configurations, magnetic reconnection is very difficult to occur. Therefore, the small amount of magnetic flux involved in the reconnection is clearly responsible for the non-eruptive behavior.

Our results suggest that the effective structures for triggering solar flares are the opposite polarity (OP) and the reversed shear (RS) configurations imposed on a magnetic field with strong shear. Our simulations indicate that the both types of configuration can trigger the eruption of the sheared field, although they show different erupting mechanisms (see Figures 3.5 (a-d) and Figures 3.7(a-d)). The difference between them is in the causality of onset process of solar flare and solar eruption. The synergetic interaction between the reconnection and the eruption must be the main driver of large flares. However, just in the beginning, one process has to cause another process in order to initiate the mutual interaction. In the eruption-induced reconnection, flux rope becomes unstable and erupts before the flare reconnection

starts. On the other hand, in the reconnection-induced eruption, the flare reconnection starts first, and reconnection generates flux rope, which becomes unstable and erupts.

In the eruption-induced reconnection, the pre-flare reconnection starts just above the photosphere before the flux rope is launched from the chromosphere. It results in the propagation of ribbons from the center of flare to the location where two-ribbon appears in the main phase of flare. This type of propagation of ribbons in pre-flare brightening was found by Kusano et al. (2012), and recently Wang et al. (2017) successfully observed the detail structure and dynamics of the pre-flare using New Solar Telescope. The results are well consistent with the model of the eruption-induced reconnection. On the other hand, the reconnection in the reconnection-induced eruption process starts on some portion in the corona. The first ribbons should appear as the separated two-ribbons and the propagation from the center cannot appear. This type of flare was also found by Kusano et al. (2012) and Bamba et al. (2017). Moreover, the comparison between the total magnetic fluxes involved in the reconnection (Table 3.1) shows that the OP-type and RS-type structures tend to involve larger fluxes in the reconnection compared to the non-eruptive cases.

The comparison between synthetic and observed flare ribbons suggests that not all the cases of simulations in our simulation agree with the observation. It can be qualitatively seen that only Case E can closely reproduce the shape and location of the flare ribbons. Figure 3.10(a) shows the flare ribbons reconstructed in Case E plotted over a Ca II H image taken by the Hinode/SOT instrument. From this image, although the reconstructed flare ribbons cannot perfectly agree with the observation, the main features of the ribbons are reproduced. The simulation of Case E does find ribbons that extend far out of the core region, but their details differ from the observation. This is due to the limited size of the computational box which cannot include the magnetic field far from the core active region and its connectivity with distant structures.

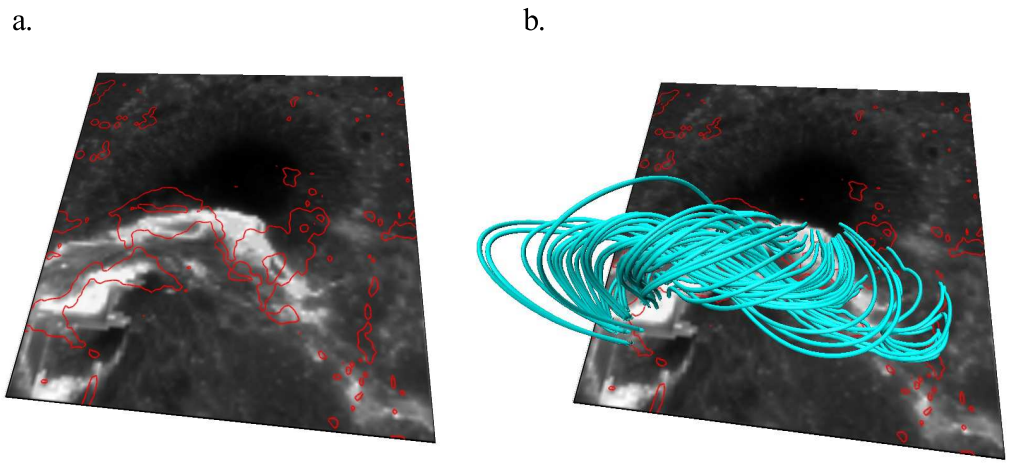

FIGURE 3.10: (a) Bird eye view of synthetic flare ribbons from Case E (red contour) at t=0.5, plotted over the flare ribbons of the Ca II H line from the Hinode/SOT observation. Red contours mark the total footpoint displacement of 0.04 in the simulation. (b)Field lines of the erupted field plotted over the panel (a).

In Figure 3.10(b), we additionally plot the field lines associated with the synthetic flare ribbons in Case E. It is found that most of the field lines traced from the reconstructed flare ribbon belong to the flux rope formed by the reconnection between the OP-type emerging flux and the pre-existing sheared field. This result is consistent with the result of Kusano et al. (2012) and Bamba et al. (2013), who studied the trigger structure through observational analysis of the magnetic field from magnetogram data and Ca II H flare ribbons. In the latter study, it was pointed out that the OP-type structure might be associated with emerging flux and that the reconnection of the OP-type emerging flux with the pre-existing sheared field may create a flux rope. Based on this assumption, it was concluded that the main flare ribbon structures both in the east and west side of the PIL were located at the feet of a twisted flux rope formed by reconnection. This main flare ribbon structures can be explained by the simulation by Kusano et al. (2012). The flare ribbons in our simulation also correspond to the footpoints of the flux rope denoted as $F - F'$ in their simulation (see Figure 3.3 in Kusano et al. (2012)).

Chapter 4

Double-arc Instability Analysis of M6.6 and X2.2 Flares in the Active Region 11158

4.1 Introduction

Several studies of flare trigger mechanisms have shown that both highly sheared field and reconnection among some field lines are required in order to produce a flare (Kusano et al., 2012). These studies used MHD simulations to show that both the configuration of the pre-existing magnetic field near the PIL and the orientation of small-scale magnetic disturbances on the PIL are important for triggering a flare. Therefore, having a large free energy accumulated in a strongly sheared magnetic field is necessary, but not sufficient for producing a flare. This result is consistent

[3]This chapter has been published in the Astrophysical Journal, 863:162(12pp), 2018 August 20, and available in http://doi.org/10.3847/1538-4357/aad181. Some modifications have been made to adjust the format and content of this thesis.

with the theory of the DAI. From numerical analyses of the stability of a double-arc electric current loop, Ishiguro and Kusano (2017) suggested that the magnetic twist and the reconnected flux may play complementary roles in triggering a flare. If a double-arc loop can be formed by a reconnection between two sheared field lines, as in the tether-cutting scenario (Moore et al., 2001), the κ parameter can be used to measure the critical condition of the DAI.

In their study, Ishiguro and Kusano (2017) found that when the value of κ exceeds a threshold κ_0, a double-arc electric current loop becomes unstable. The threshold κ_0 varies from approximately 0.08 to 0.175, depending on the external magnetic field enveloping the double-arc structure. This suggests that the magnetic twist and tether-cutting reconnection are important in destabilizing sheared magnetic field (Ishiguro and Kusano, 2017). However, calculating the value of κ for an AR is not trivial, because the observational data lack information about the magnetic twist and the reconnected flux. Although one can determine the force-free alpha parameter from magnetogram data, those data contain no information about the length of magnetic loops that can be used to derive the twist. Moreover, the reconnected flux, which is required to calculate κ, is hardly known from observations. Therefore, it is important to develop a way to calculate κ in an AR to understand the characteristics pattern of its evolution before and after a large flare happens.

We have employed DAI analysis to study flares in the AR NOAA 11158. The evolution of the magnetic field in this AR have been extensively studied, e.g. regarding the magnetic structure (Sun et al., 2012; Toriumi et al., 2013; Zhao et al., 2014; Malanushenko et al., 2014), magnetic helicity (Jing et al., 2012; Dalmasse et al., 2013; Tziotziou et al., 2013), photospheric field (Liu et al., 2012; Petrie, 2012; Wang et al., 2012), magnetic energy (Sun et al., 2012; Aschwanden et al., 2014; Malanushenko et al., 2014), magnetic twist (Liu et al., 2013; Sun et al., 2012; Inoue et al., 2011, 2014a; Zhao et al., 2014; Malanushenko et al., 2014), and others.

Observational studies suggested that tether-cutting reconnection happened in the

AR during the M6.6 (Liu et al., 2012) and X2.2 (Wang et al., 2012; Liu et al., 2013) flares, therefore double-arc current structure could be presumably occurred in the AR. Thus, DAI analysis can be applied to explain the occurrences of these flares. Our goal is to find a parameter that can be used to study the capability to produce a solar flare by implementing such a DAI analysis for a real AR. First, we study the spatial and temporal evolution of the twist distribution of the AR based on the NLFFF model. Next, we calculate a parameter to enable us to extract information about the twist and to determine the reconnected flux. Finally, we show how our proposed parameter can be used as a possible forewarning for the likelihood of flare occurrence in an AR.

4.2 Overview of AR 11158

AR 11158 initially occurred as two simple bipoles before growing to become complex quadrupole systems. Rotational and translational motions of the spots were observed within the AR (Jiang et al., 2012); these caused the magnetic field near the PIL to become sheared and elongated (Toriumi et al., 2014). Figures 4.1(a), (b), and (c) show the coronal magnetic field of AR 11158 observed by AIA 171 Å at three different times. AR 11158 produced many flares and CMEs during its passage across the solar disk. In this paper, we focus on the M6.6 flare, which occurred on 2011 February 13 at 17:28 UT, and on the X2.2 flare, which happened on 2011 February 15 at 01:44 UT. These flares occurred in the core of the AR, which is marked by the orange rectangle in Figure 4.1(g).

We have used SDO/HMI observations of the vector magnetic field from the SHARP (Bobra et al., 2014). The 180-deg ambiguity is resolved by using the minimum-energy method (Leka et al., 2009). We used a three-hour cadence of the SHARP data for AR 11158, extending from 00:00 UT on 2011-Feb-13 to 21:00 UT on 2011-Feb-15 with 744×377 pixels covering about 268×134 Mm^2. For detailed analyses

of two large flares that occurred during this period, we used the 12-minute cadence of the SHARP data from 15:00−18:00 UT 2011-Feb-13, when M6.6 flare happened, and 00:00−03:00 UT 2011-Feb-15, when X2.2 flare occurred.

We reduced the original vector magnetogram data by using IDL CONGRID function with the nearest-neighbour interpolation to 256×128 pixels, which we used as bottom boundaries for extrapolating the coronal magnetic field. We employed the NLFFF extrapolation technique to reconstruct the coronal magnetic field by applying the MHD relaxation method (Inoue et al., 2014b) in a computational box of 256×128×128 grids. First, we calculated the potential field for the AR from the normal component (B_r) of the given boundary condition by solving Poisson's equation using the Fourier method (Alissandrakis, 1981). The tangential components (B_ϕ, B_θ) then incrementally changed at the bottom boundary to match the observational tangential components. Next, we calculate a set of MHD-like equations until the solution approaches the force-free field (for the details of MHD relaxation method, see Inoue et al. (2014b)). All the physical variables at all the boundaries are fixed during the iteration. The method and parameters used here are similar to the NLFFF calculations in our previous work.

4.3 Critical Instability Parameter

4.3.1 Kappa star

To derive information similar to that embodied in the parameter κ from the observational data, we propose the alternative parameter namely κ^* that is defined as follows:

$$\kappa^*_{T_c} = \frac{\int_{\frac{T_w}{T_c}>1} |T_w| \, \mathrm{d}\phi}{\phi_{tot}}, \tag{4.1}$$

with $\mathrm{d}\phi = |B_r|\mathrm{d}S$.

In this formula, instead of using the reconnected flux, which is not measurable, we integrate the magnetic twist only over the high-twist area as a function of magnetic flux (ϕ). The threshold for the integrated magnetic twist is given by T_c. The concept of replacing the reconnected flux with the high-twist flux is based on the assumption that internal reconnection between high-twist field lines in the pre-flare phase is more effective in enhancing the creation of higher twist flux ropes, which can be expected to drive a flare (Démoulin and Aulanier, 2010). This assumption is supported by the fact that large flares usually come from the core of an AR, which contains highly twisted field lines, and which stores a large free energy. In fact, the NLFFFs of several ARs showed that the shapes and locations of flare ribbons are very well matched with the footpoint locations of the highly twisted field lines (Inoue et al., 2013; Liu et al., 2016). Therefore, it is likely that a flare is triggered by the reconnection of high-twist field.

The definition of $\kappa^*_{T_c}$ requires a proper threshold (T_c) to determine the high-twist area, since this can affect the overall estimation of $\kappa^*_{T_c}$. Inoue et al. (2014a) found that the maximum twist value of the AR 11158 was less than unity before the flare. A few of field lines had twist more than 0.5, although most of the field lines had smaller values. Inoue et al. (2011, 2016) showed that ARs 10930 and 12192 also had similar magnetic twist properties. Based on those results (Inoue et al. (2011, 2014a, 2016)) we have employed 0.5 as a benchmark for the high-twist threshold and have surveyed the dependence of $\kappa^*_{T_c}$ on T_c around this value (0.5). Another possible way to determine T_c is by analyzing the twist distribution after a flare occurs. This distribution can be expected to change, because the flare relaxes the magnetic twist. Magnetic field will thus tend to have lower twist values after a flare. Magnetic flux that loses twist can be considered to be reconnected flux. Therefore, the maximum twist value of the field remaining after a flare, denoted by T_m, can be used as a minimum threshold for determining the high-twist field before the flare. Here, we first try to calculate $\kappa^*_{0.5}$, and we then compare it with $\kappa^*_{T_m}$, which we compute using coronal magnetic field reconstructed from NLFFF extrapolation. The twist of a field

line is calculated from the following definition of magnetic twist (Berger and Prior, 2006):

$$T_w = \frac{1}{4\pi} \int \alpha \, \mathrm{d}l. \tag{4.2}$$

Here, α is the force-free parameter

$$\alpha = \frac{\nabla \times \mathbf{B} \cdot \mathbf{B}}{|B|^2}, \tag{4.3}$$

which is calculated for each point in a computational box along a field line, where l is the length coordinate along the field line. The magnetic twist is thus defined as a function of each field line. This definition was also used by Inoue et al. (2015, 2016) to calculate the twist. We then evaluate equation 4.1 for several different values of T_c at each different epoch.

In the weak field region, there are big numerical errors in the calculation of α, and the evaluation of the magnetic twist is less reliable. Therefore, we exclude the magnetic field lines coming from weak field regions by using a minimum field threshold in the calculation. In this work, we only consider magnetic flux density larger than 140 G in calculating $\kappa^*_{T_c}$. The total flux (ϕ_{tot}) in equation 4.1 is defined as the total unsigned flux, which is the closed field within the core of the AR. This excludes fluxes for which the field lines are open or their connectivity is beyond the area within the core of the AR, where the center of the flare ribbons was observed during the flares.

4.4 Results

4.4.1 NLFFF Extrapolations

NLFFF extrapolation provides the reconstructed coronal magnetic field for AR 11158 from 2011 February 13 – 2011 February 15 (Figures 4.1(d), (e), and (f)).

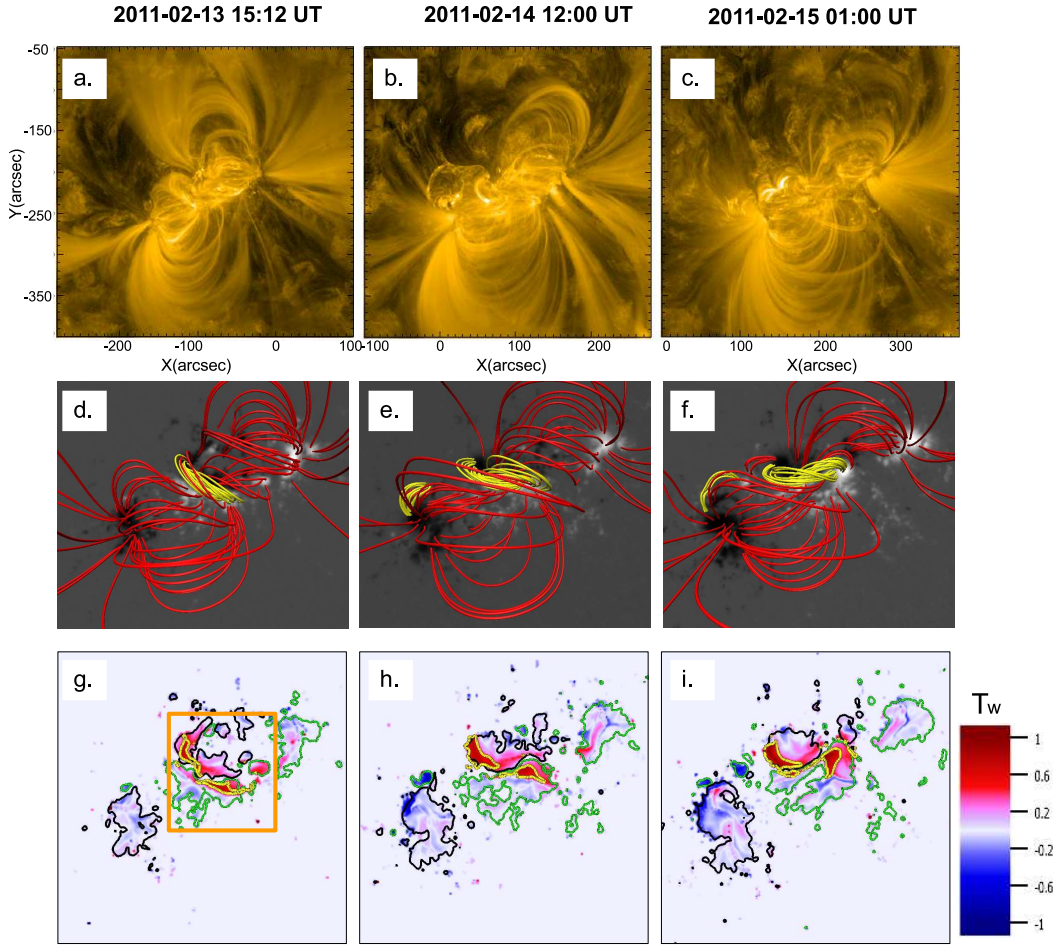

FIGURE 4.1: The coronal magnetic fields of AR 11158 observed by SDO/AIA 171 Å at three different times (a),(b), and (c). The coronal magnetic fields reconstructed from NLFFF extrapolations for AR 11158 corresponding to the epochs of the top panels are presented in (d),(e), and (f). The yellow (red) lines show selected magnetic field lines with twists higher (lower) than 0.5 turn. Twist map for AR 11158 calculated from the NLFFF model (g), (h), and (i). The green (black) contours in the bottom panels represent the normal components of magnetic field at 560 G (-560 G), respectively. The yellow contours show the integration surface for calculating $\kappa^*_{T_c}$ with $T_c = 0.5$.

The field lines (yellow lines) within the core of the AR have arcade-like structure with a relatively strong twist mainly near the PIL. These figures show that the magnetic field evolved during this period. Although we did not quantitatively compare the field lines with the observation, in general, the reconstructed coronal fields morphologies match with the observations in Figures 4.1(a), (b) and (c). The general morphologies and the locations of the high-twist fields also in agreement with many previous studies (Jing et al., 2012; Sun et al., 2012; Dalmasse et al., 2013; Liu et al., 2013; Inoue et al., 2013, 2014a; Aschwanden et al., 2014; Zhao et al., 2014; Malanushenko et al., 2014).

Unlike Zhao et al. (2014) who could identify the twisted flux rope from the topology of the reconstructed coronal field, we could not find obvious topological signature of flux rope existing in our NLFFF during our analysis time window. It might be due to the fact that there were few magnetic flux with twist higher than one-turn in our NLFFF and it is difficult to be topologically defined as a flux rope. However, our result is consistent with other NLFFF results (Jing et al., 2012; Sun et al., 2012; Liu et al., 2013; Inoue et al., 2014a; Malanushenko et al., 2014). The high twist region in our result also in agreement with the region with high helicity flux (Dalmasse et al., 2013) and the location of the flare ribbons (Bamba et al., 2013; Liu et al., 2013), as well as the high current density region (Janvier et al., 2014).

Figures 4.1 (g), (h), and (i) show the evolution of the twist distribution map, with the magnetic twist of the field lines plotted at the footpoints of field lines according to a color scale. This shows that the high-twist (strongly right-handed twist corresponding to $T_w > 0.5$) areas are concentrated in only a limited part of the AR. The high-twist area grew and became even more twisted just before the X2.2 flare (Figure 4.1(i)). Most parts of the AR have twist values less than 0.25, but near the PIL the twist can reach more than 0.5, even up to about a full turn. This is consistent with the results of Sun et al. (2012) and Inoue et al. (2014a). A high-twist (strong negative/left-handed twist) area also developed in the eastern part of the AR, which

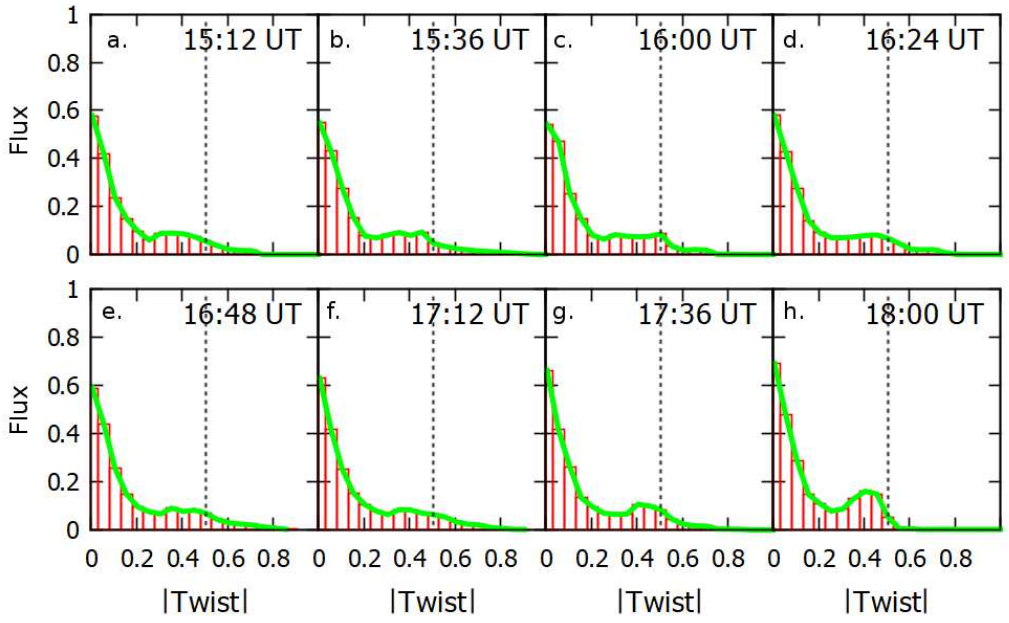

FIGURE 4.2: Evolution of the twist distribution of AR 11158 before and after the M6.6 flare on 2011 February 13. The M6.6 flare onset time is 17:28 UT. The flux plotted on the y-axis is normalized by 7.72×10^{21} Mx. The dashed vertical line in each panel marks the value of twist equal to 0.5 turn.

did not exist initially on February 13. Both of these high-twist areas produced several flares. However, here we focus on the flares resulted from the high-twist core region near the center of the AR, where the M6.6 and X2.2 flares occurred.

4.4.2 Twist Distribution and Evolution

4.4.2.1 2011 February 13 (M6.6 Flare Event)

In order to examine the evolution of twist before and after M6.6 flare, we plotted the distribution of magnetic twist in the core of AR 11158 from 15:00−18:00 UT on 2011 Feb 13 with a 12-minute cadence. Note that M6.6 flare started at around 17:28 UT. We obtained the twist distribution by binning the absolute value of twist with increments of 0.05 and then summing the magnetic flux of the B_r component, which corresponds to the footpoints of the field lines for which we calculated the twist

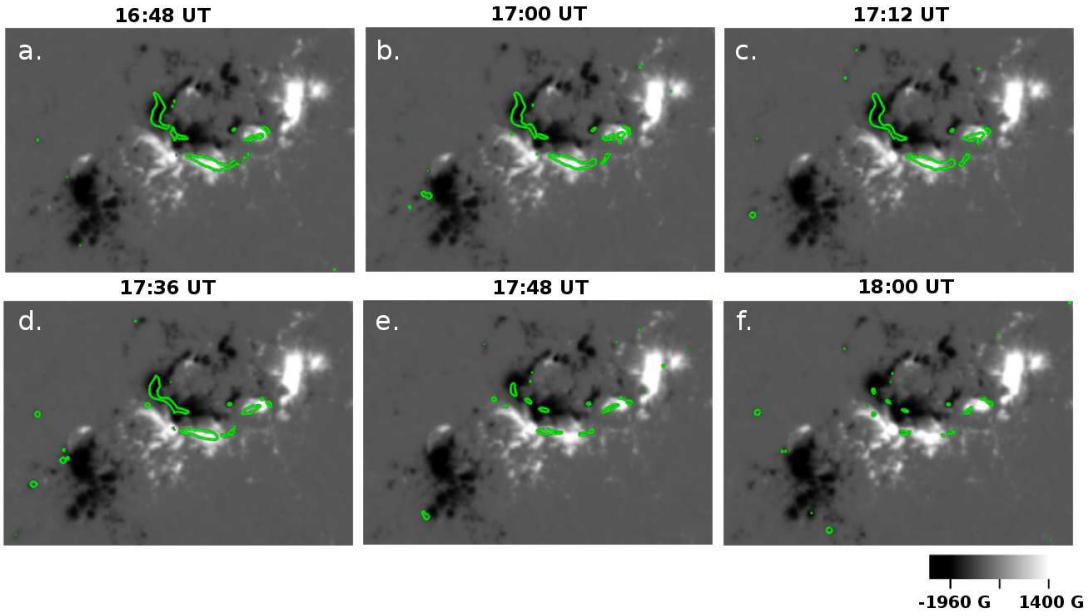

FIGURE 4.3: Spatial evolution of the high-twist field in AR 1158 before (a, b, c) and after (d, e, f) M6.6 flare on 2011 February 13. The green contours correspond to areas with absolute magnetic twist equal to 0.5. The top (bottom) panels show the evolution of the high-twist distribution before (after) the M6.6 flare.

within the area in Figure 4.1. We excluded field from areas with weak magnetic field (less than 280 G) in order to eliminate noise. The plot of the amount of magnetic flux as a function of its corresponding twist, normalized by 7.72×10^{21} Mx, is presented in each panel of Figure 4.2, which shows the evolution of the twist distribution of AR 11158 before and after M6.6 flare. In general, most field lines had only small amount of twist, with values less than 0.2 turn. However, several field lines had twist exceeding 0.5 or even 0.8 turn before the flare occurred. After the flare, almost all twists of the high-twist magnetic field gradually reduced to less than 0.6 turn. This result is consistent with the result of Liu et al. (2012).

The selected spatial evolution of the magnetic twist distribution in AR 11158 during the three-hour period from 15:00−18:00 UT on February 13 is presented in Figure 4.3. This figure shows how the high-twist (larger than 0.5 turn) field area (enclosed by the green contour) intensified, with the magnetic flux was 1.6×10^{21} Mx, just before the flare (17:12 UT) and then shrank significantly to 3.6×10^{20} Mx after the flare (18:00 UT). This suggested that magnetic helicity might have been transferred

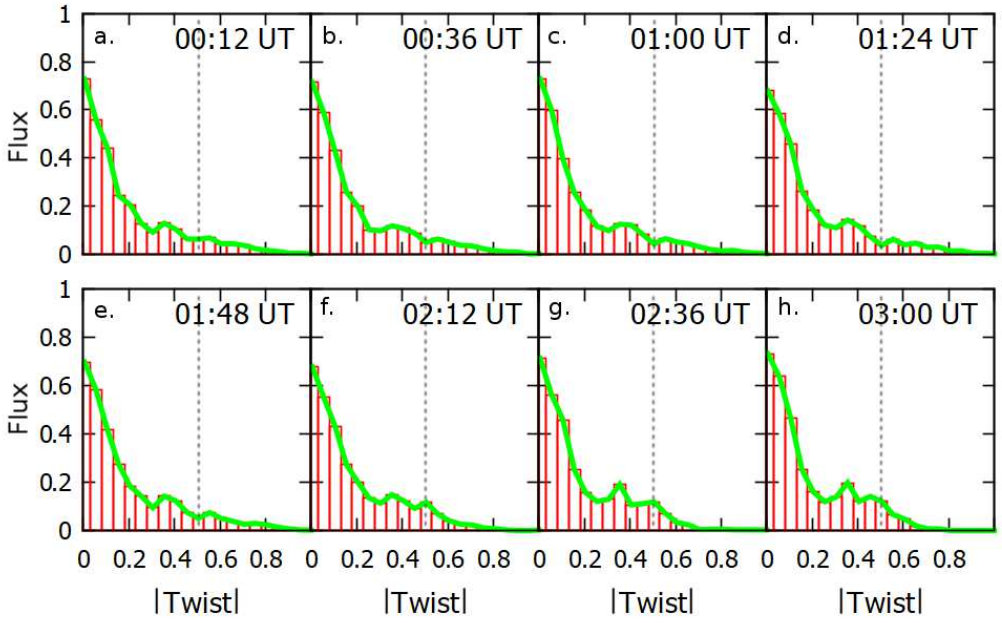

FIGURE 4.4: Evolution of the twist distribution of AR 11158 before and after the X2.2 flare on 2011 February 15. The X2.2 flare onset time is 01:44 UT. The flux plotted on the y-axis is normalized by 7.72×10^{21} Mx. The dashed vertical line in each panel marks the value of twist equal to 0.5 turn.

from the core of the AR to the upper region where the magnetic field erupted during the flare to the interplanetary space. The results of the twist distribution and evolution before and after the flare are consistent with the result of Inoue et al. (2013).

4.4.2.2 2011 February 15 (X2.2 Flare Event)

X2.2 flare started around 01:44 UT on February 15. To study the evolution of magnetic twist in AR 11158 before and after the flare, we plotted the twist distribution in the AR from 00:00−03:00 UT on February 15 with a 12-minute cadence. Selected plots of the twist distribution are shown in Figure 4.4. Over this time period, the trend was similar to the development of the twist distribution for the M6.6 flare. However, before the X2.2 flare, more field existed with twist higher than 0.5, or even larger than 0.8 turn. This shows that, during this period, the magnetic field of AR

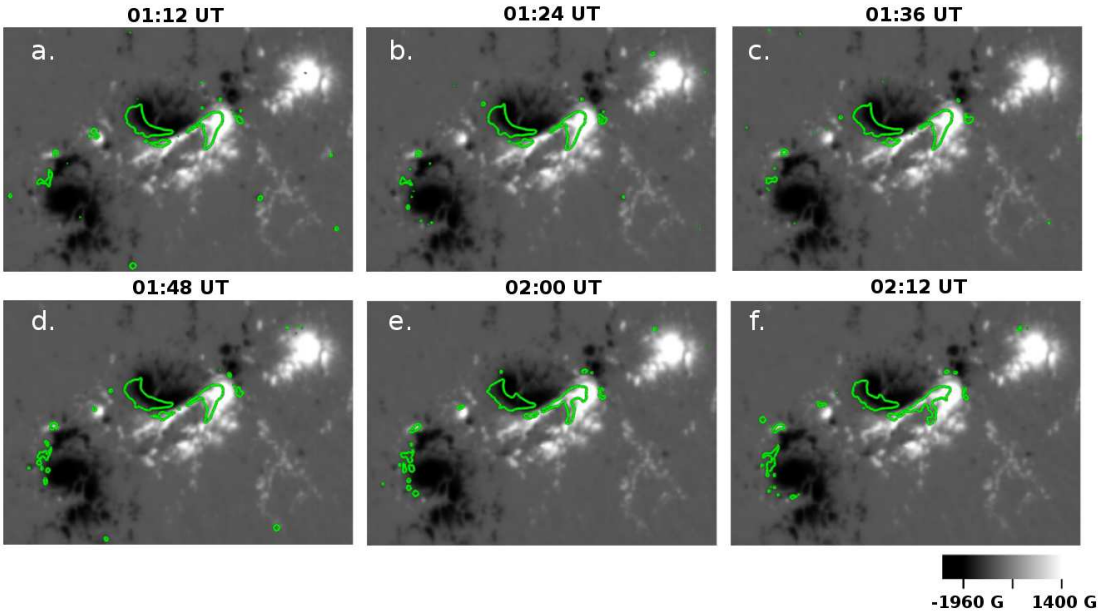

FIGURE 4.5: Spatial evolution of high-twist field in AR 1158 before (a, b, c) and after (d, e, f) the X2.2 flare on 2011 February 15. The green contours correspond to areas with absolute magnetic twist equal to 0.5. The top (bottom) panels show the evolution of high-twist distribution before (after) the X2.2 flare.

11158 had stronger shear than before the previous event. Field with twist higher than 0.8 turn mostly disappeared after the flare. This is also similar to the previous event, although the AR retained more flux with magnetic twist higher than 0.5 even one hour after the peak of the flare.

We also plotted contours for magnetic field with twist higher than 0.5 over the B_r component of the magnetogram data for the period 00:00−03:00 UT on February 15 with a 12-minute cadence. Selected plots of these images are shown in Figure 4.5. The region with magnetic twist higher than 0.5 did not exhibit significant changes before the flare (2×10^{21} Mx at 01:36 UT), but it gradually reduced in size just after the flare (1.9×10^{21} Mx at 02:12 UT). However, high-twist region with $T_w > 0.6$ decreased from 1.45×10^{21} Mx before the flare (01:36 UT) to 7×10^{20} Mx after the flare (02:12 UT). Unlike M6.6 flare, high-twist flux still remained in relatively large area, instead of significantly disappearing. This implies that AR 11158 still retained a significant amount of free energy. These results of the twist distribution

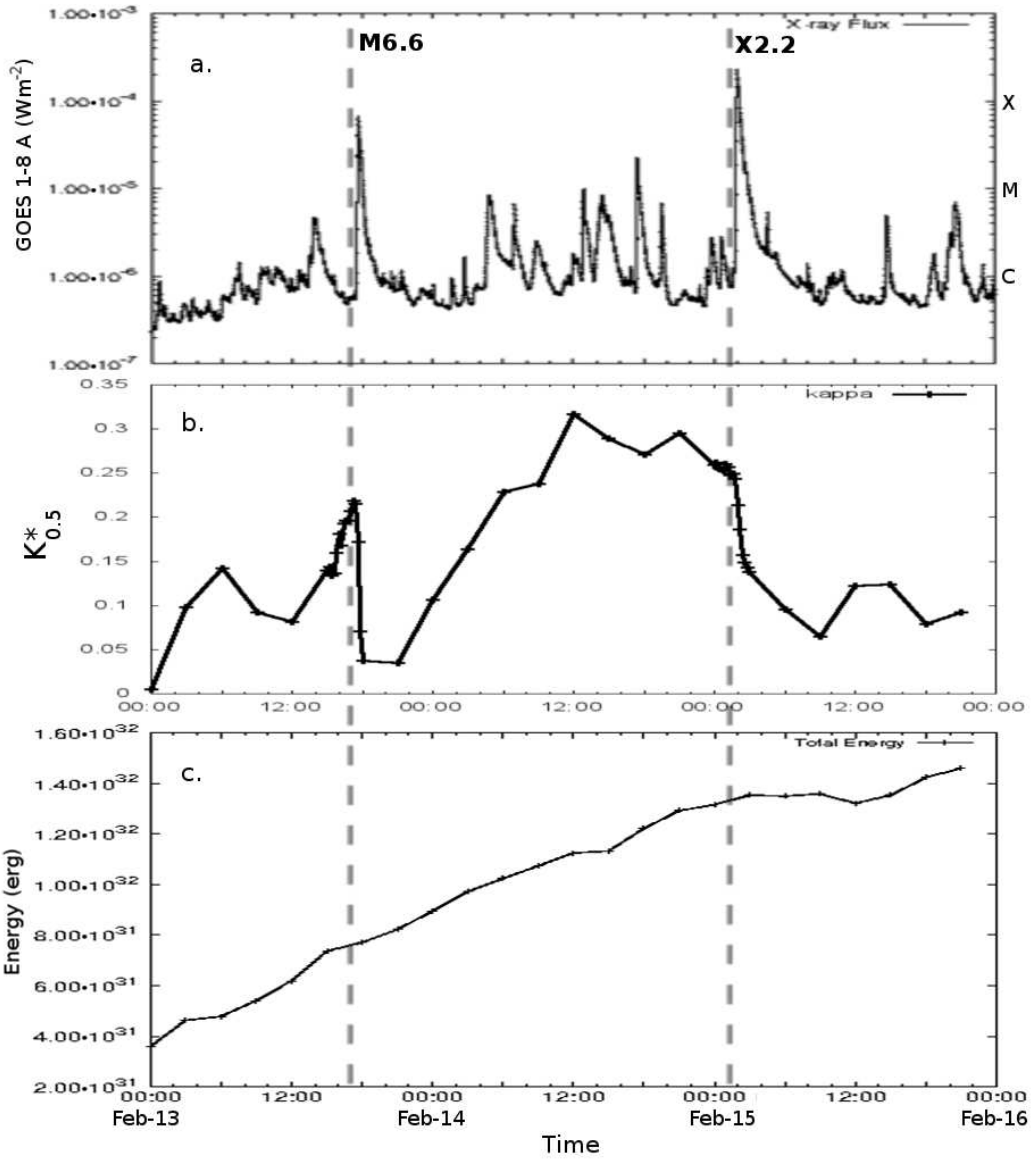

FIGURE 4.6: Evolution of the GOES X-ray flux (a), $\kappa^*_{0.5}$ (b), and the total magnetic energy of the core of the AR (c) during the flare-active period from 2011, February 13 to February 15. The dashed vertical lines mark the onset times of the flares.

and evolution before and after the flare are also consistent with the result of Inoue et al. (2013).

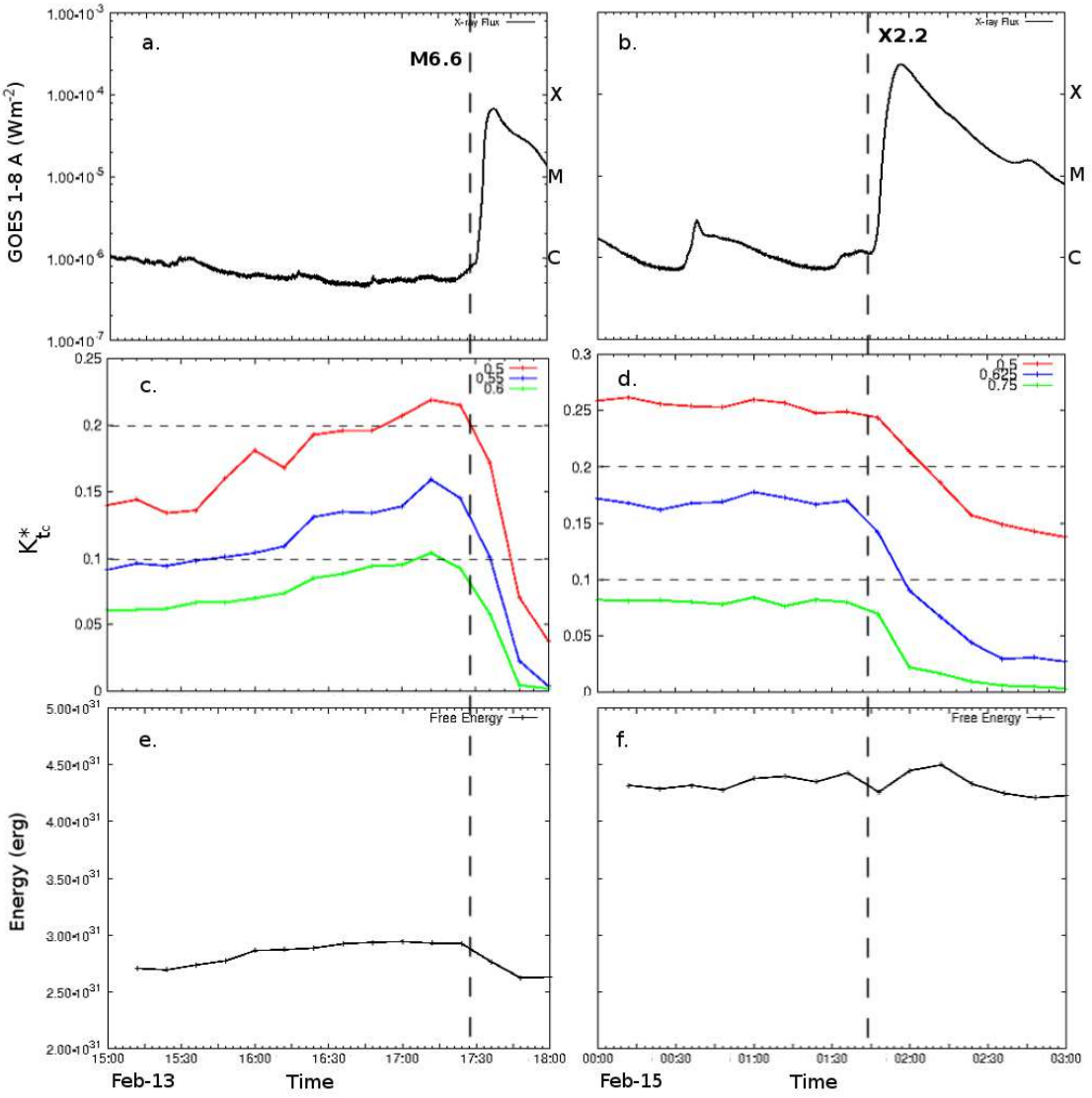

FIGURE 4.7: Panels (a), (c), and (e) show the evolution of the GOES X-ray flux, $\kappa^*_{T_c}$, and the free energy of the core of the AR for the M6.6 flare, respectively. Panels (b), (d), and (f) show the corresponding quantities for the X2.2 flare, respectively. The legends in panels (c) and (d) show three values of T_c as colored lines. The dashed vertical lines mark the onset times of the flares.

4.4.3 Kappa star Evolution

For a more detailed analysis, we have plotted in Figures 4.7 (a) and (b) the evolution of the GOES X-ray flux during M6.6 and X2.2 flare, respectively. We also plotted in Figures 4.7 (c) and (e) the evolution of $\kappa^*_{T_c}$ and free energy, each with a 12-minute cadence, just before and just after the M6.6 flare, respectively. We used three different values for the threshold (T_c) for the high-twist flux for this event (shown as different colored lines in Figure 4.7 (c)). The first threshold ($T_c = 0.5$; red line) is the benchmark. We obtained the second threshold ($T_c = 0.6$; green line) from the highest value of the magnetic twist after the flare (T_m), as can be seen from the last panel in Figure 4.2. The third threshold ($T_c = 0.55$; blue line) is just the mean value between the first and second, which we used for comparison. Figure 4.7(c) shows that $\kappa^*_{T_c}$ increased for each value of T_c before the flare and then significantly decreased just after the flare started. The trend is similar for all three thresholds, although $\kappa^*_{T_c}$ becomes smaller for higher T_c. It is interesting that the maximum $\kappa^*_{T_m}$ is slightly greater than 0.1. This is consistent with the theoretical threshold for κ in DAI analysis done by Ishiguro and Kusano (2017). Note that the free magnetic energy decreased slightly after the flare, which shows that some energy was released during the flare.

In Figures 4.7(d) and (f), we plotted the same parameters as in Figures 4.7(c) and (e), but for X2.2 flare. We also used three different thresholds (T_c) for the high-twist flux (shown as different lines in Figure 4.7(d). The first threshold ($T_c = 0.5$; red line) is again the benchmark threshold. The second ($T_c = 0.75$; green line) is the highest twist of the field after the flare (T_m) (see the last panel in Figure 4.4). The third threshold ($T_c = 0.625$; blue line) is the mean between the first and second, which we have again used for comparison. Note that $\kappa^*_{T_c}$ increased long before the X2.2 flare occurred. Figure 4.6(b) shows that this increase began on February 14 around 00:00 UT and exceeded 0.2 around 04:00 UT, which corresponded to the phase when the AR resumed the flare activity producing the C8.3 flare at 04:29 UT

on February 14. However, after the X2.2 flare happened, $\kappa^*_{T_c}$ decreased significantly, just as it did following the M6.6 flare event. Note also in Figure 4.7(d) that $\kappa^*_{T_m}$ (green line) has a maximum value slightly below 0.1. This value is again consistent with the critical threshold for the DAI introduced by Ishiguro and Kusano (2017). Figure 4.7(f) shows that the free energy was at the higher level before the X2.2 flare than before the M6.6 flare. It increased during the flare, and finally decreased after the X2.2 flare.

4.4.4 Magnetic Energy Evolution

Analysis of the magnetic energy of the core region shows that the total energy increased continuously during the three-day period covered by the data we used, as can be seen in Figure 4.6(c). Although from Figure 4.6(c) we see that the magnetic energy accumulating in the AR increased continously during the three days of observation, the $\kappa^*_{0.5}$ profile shows dramatic changes before and after the flares. This suggests that $\kappa^*_{0.5}$ can serve as a proxy for the degree of DAI necessary for an AR to produce a flare. On the other hand, the total magnetic energy did not show significant changes even during the flares, and instead increased almost monotonically. Ultimately, substantial amount of energy about 1.2×10^{32} erg was stored before the X2.2 flare after the M6.6 flare. This implies that the amount of magnetic energy stored in the AR does not represent the critical condition for a flare to occur, but it may be related to the size of the event once a flare does occur.

Figures 4.7(e) and (f) show that the free energy for M6.6 and X2.2 flares, respectively, were also at different levels and that the free energy for the latter was almost twice that of the former. Thus, significant energy accumulated in the core of the AR from day to day. When M6.6 flare happened, the free energy decreased ($\approx$8 %), showing that some of the energy had been released by the flare. A similar thing happened in the X2.2 flare: some of the energy was released and the free energy decreased. This energy evolution is consistent with previous results by Sun et al. (2012); Aschwanden

et al. (2014) and Malanushenko et al. (2014), although we obtained a smaller energy level than they found because we calculated the energy only for the core region. However, the general trend of the free energy was still increasing even after the flare happened, showing that using just the free energy profile to predict the occurrence of a flare is somewhat problematic. This is because we cannot differentiate the critical state required to trigger a flare during the continuous accumulation of energy in an AR, although the stored energy and helicity are related to the size and class of a flare once it occurs.

Our result confirmed that non-potential energy does not directly provides necessary criterion for an eruption as it has been known in previous studies, e.g. in Schrijver et al. (2005) and Jing et al. (2009). This is also consistent with previous simulation study by Pariat et al. (2017). In this sense, analyzing the $\kappa^*_{T_c}$ profile can be more helpful for monitoring the condition necessary to trigger a flare and for evaluating how likely it is that an AR may erupt. Information about the free energy is useful for estimating the maximum size (class) of a flare that can be produced in an AR.

4.5 Discussions

4.5.1 Determination of T_c

We have found that the twist of magnetic field in the AR evolved significantly during our three-day analysis time window. In general, the magnetic field of the AR tended to relax to a lower state after the flares occurred. Because the coronal plasma just above the core of the AR erupted, it carried some of the high-twist field from the lower corona to the higher corona or out into interplanetary space. Subsequently, the high-twist magnetic field in the core of the AR relaxed and the magnetic twists decreased. However, some of the high-twist magnetic field still remained there even

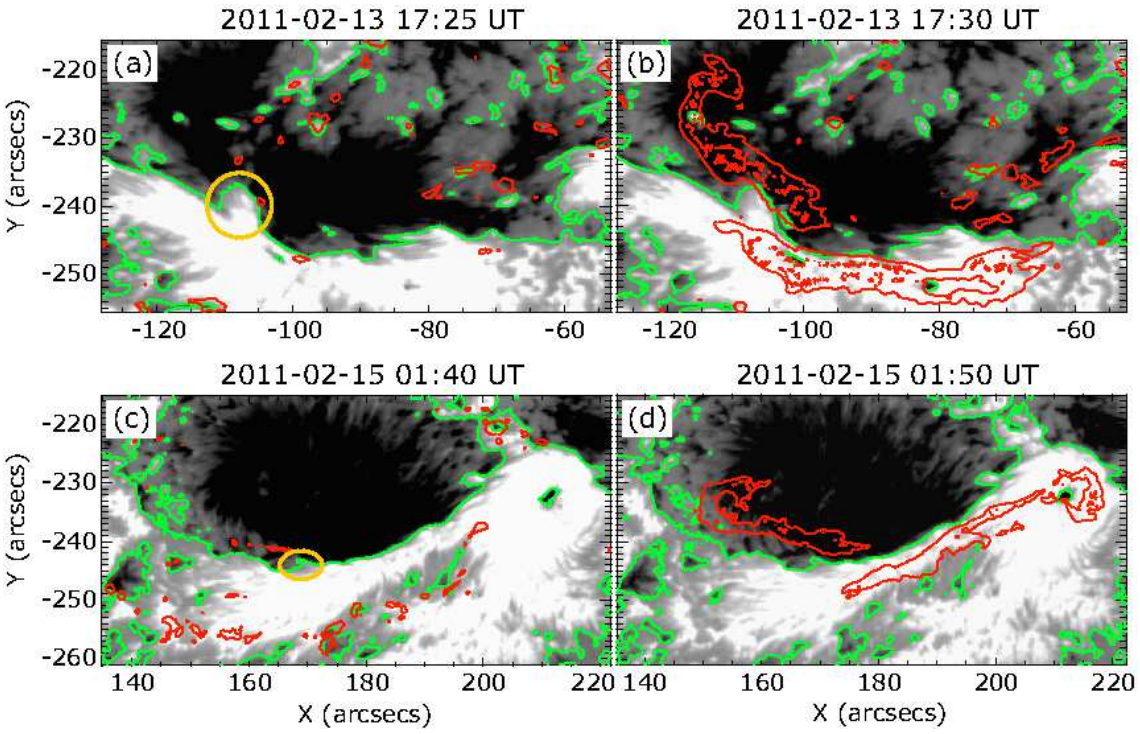

FIGURE 4.8: Evolution of M6.6 flare (top) and X2.2 flare (bottom) plotted on the line-of-sight (LOS) component of the magnetic field obtained from Hinode/SP. The white and black colors correspond to positive and negative polarities, respectively. The green lines represent the PIL, and red contours show the strong Ca II H line emission. Yellow circles outline the magnetic "peninsula" structures that trigger the flares.

after the flares. This result that magnetic twist decreased after the flares is consistent with previous studies by Inoue et al. (2013) and Liu et al. (2016).

Previous studies of flare ribbons using footpoint displacement analyses in MHD simulations (Toriumi et al., 2013; Inoue et al., 2015) and quasi separatrix layers (QSL) in NLFFF models (Aulanier et al., 2012; Guo et al., 2013; Janvier et al., 2014; Savcheva et al., 2016) have shown that the shapes and locations of flare ribbons usually correspond to the shapes and locations of the footpoints of the reconnected flux. Here, we have found that the contours and locations of the high-twist fields in Figures 4.3 and 4.5 correspond to the shapes and locations of the observed flare ribbons for both flares in Figures 4.8 (b) and (d). During the flares, reconnection thus tends to involve high-twist fields. This result is consistent with the study by Inoue

et al. (2015). It also supports the idea that the reconnected flux in equation 1.23 can be replaced by some part of the high-twist flux in equation 4.1, although they are not completely identical. Moreover, the flare ribbon marks the reconnected flux during the flare, while the reconnected flux in equation 1.23 only includes internal reconnection among the field lines before the flare. Therefore, the high-twist flux always overestimates the reconnected flux in the pre-flare state. Consequently, $\kappa^*_{T_c}$ generally has a higher value than the initial definition of κ.

The evolution of $\kappa^*_{T_c}$ in Figures 4.7(c) and (d) suggests that the AR tended to have relatively large value of $\kappa^*_{T_c}$ before a flare and it quickly decreased after the flare. These results suggest that we may be able to use $\kappa^*_{T_c}$ as a useful parameter as a forewarning of a flare. However, it is still not clear how we can choose the threshold (T_c) for the magnetic twist to use it as a flare predictor. For both of the flares we studied, when $T_c = T_m$, the values of $\kappa^*_{T_c}$ just prior to the eruption were around 0.1, which is consistent with the critical value derived by Ishiguro and Kusano (2017). They found that the critical κ for the DAI were 0.08 and 0.125, respectively, for a point source and for the external field that decay exponentially with altitude. We suggest that the maximum value of the remaining high-twist field (T_m), has more physical meaning than other values of twist as a proper value of T_c for the high-twist flux. Using this threshold reduces the possibility of including non-reconnected flux in calculating $\kappa^*_{T_c}$, which makes it more consistent with the theoretical definition of κ.

4.5.2 Importance of Trigger Structure

Our results show that $\kappa^*_{T_c}$ increased about one day before the X2.2 flare, while it increased only about 6 hours before the M6.6 flare. In order to understand the different features of these two flares, we have investigated their trigger mechanisms by analyzing the magnetogram data taken by Hinode/SOT. Figure 4.8 shows the evolution of the core of the AR before and after the M6.6 and X2.2 flares.

Bamba et al. (2013, 2014) found that M6.6 flare was triggered by a relatively large magnetic "peninsula", in which a region with positive polarity intruded into the one with negative polarity (the yellow circle in Figure 4.8(a)). The trigger structure (peninsula) was formed since around February 13 13:00 UT by inflow of small positive magnetic patches from the northern positive region (Toriumi et al., 2013). This caused the azimuth angle of the magnetic field on the west (the right side) boundary of the peninsula to be reversed from that of the main sheared field in the PIL, enabling reconnection on that boundary to occur by means of the tether-cutting mechanism. This kind of trigger structure has been defined as a "reversed-shear" (RS) structure by Kusano et al. (2012). This suggests that in the M6.6 flare, the magnetic structure of the core of the AR was strongly perturbed by the presence of the large peninsula structure before the flare just after the $\kappa^*_{T_c}$ increased significantly. Such a large peninsula structure can easily trigger a flare if the magnetic twist grows high enough, and this provides a possible explanation for the prompt onset of M6.6 flare immediately after the value of $\kappa^*_{T_c}$ exceeded the threshold.

On the other hand, X2.2 flare was triggered by a small RS-structure near the PIL (the yellow circle in Figure 4.8(c)). This small structure could hardly trigger a flare, since it could only perturb a small portion of the lower coronal field (Bamba et al., 2013). In addition, we found that the formation of the trigger structure (peninsula) for the X2.2 flare just started from around February 14 21:00 UT, which was about one day after the $\kappa^*_{T_c}$ increased significantly. Hence, although helicity was continuously injected into the core of the AR, the field structure was able to maintain its high $\kappa^*_{T_c}$ value for a relatively long period before the structure of the small RS field met the condition for instability. For that reason, more free energy and magnetic helicity were stored before the onset of the flare, and finally a bigger flare erupted than the previous one. This suggests that the structure of the trigger field is also important to complement the information provided by $\kappa^*_{T_c}$ for estimating the probability of the occurrence of a flare.

Chapter 5

Double Arc Instability Analysis for a Complex Active Region

We have shown in the previous chapter that $\kappa^*_{T_c}$ evolution shows dramatic changes before the two big flares occurred in AR 11158. However, we can consider that the AR 11158 was relatively simple because the core region consisted only of a bipole. In the next study, we tried to explore the possibility of employing the DAI analysis in the more complex AR, which is AR 12673 that produced many large flares in September 2017. We also show how we can improve the method to determine the region where the highly twisted field lines and magnetic flux were used in the calculation of $\kappa^*_{T_c}$.

5.1 Overview of AR 12673

Active Region (AR) 12673 produced at least 4 X-class and 27 M-class flares, two of them are X2.2 and X9.3 flares happened on September 6th, 2017 (Yang et al., 2017) as it is shown by the profile of GOES X-ray flux in figure 5.1. The X9.3 flare is still the largest flare ever in the solar cycle 24. The huge flares from this

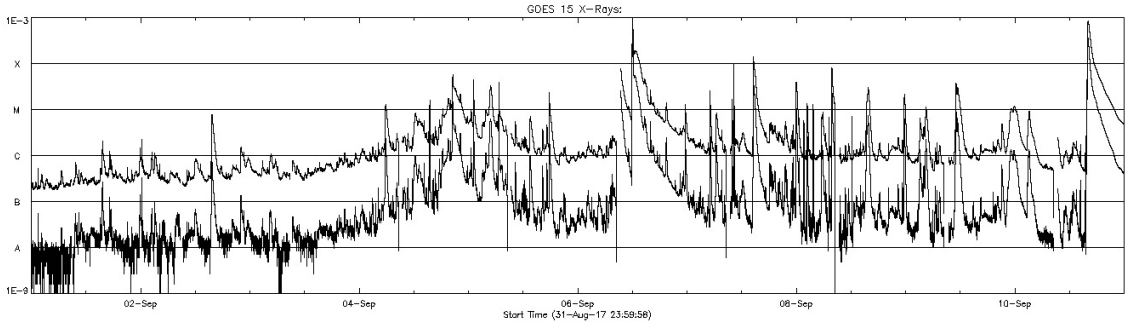

FIGURE 5.1: GOES-15 X-ray flux from September 1-11, 2017, which was dominantly affected by the activities of AR 12673.

AR has produced a lot of energetic protons and radiation that affected geomagnet and ionosphere and has some implications to the navigation services (Berdermann et al., 2017). The magnetic field of this AR showed very dynamics evolution from its birth until the two large flares happened. Large magnetic flux emerged very quickly within three days prior to the flares and strong shearing motions happened on the surface of the Sun that led to the formation of strongly twisted coronal magnetic field (Verma, 2018). Understanding the evolution of this AR is very important to reveal the possible mechanism that work in an AR before large flares happen.

Several studies have been conducted to explain the reason why this AR was very active as well as to understand the flare trigger mechanism in this complex AR. Yang et al. (2017) suggested that some pairs of emerging flux and the apparent motion of these fluxes formed a complex magnetic system, where the large positive polarity region blocked the motion of smaller negative patch. The formation and evolution scenario of the complex magnetic system in this AR is shown in figure 5.2 (Yang et al., 2017). In the beginning, there were two pairs of bipole that emerged (a) and then the same polarities patches converged to form a bigger bipole system. After that, two new bipoles emerged in between the old combined bipole (b) and moved in such a way that created a semi circular complex magnetic system with magnetic flux rope existed (c). The small negative patch then penetrated to trigger the X-class flare. Study of coronal magnetic field models by NLFFF showed that the shearing motion, sunspot rotation, and the dynamics of a magnetic flux rope in

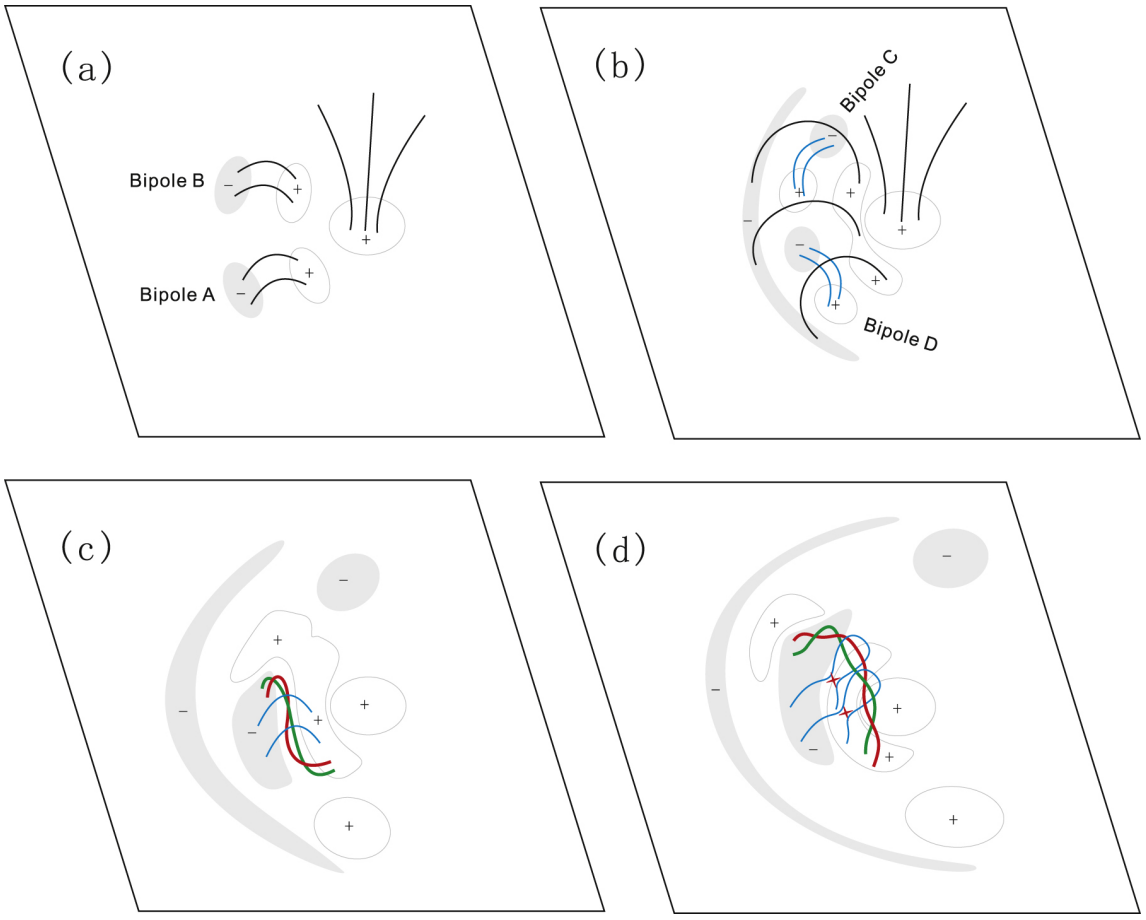

FIGURE 5.2: Scenario of photospheric magnetic field evolution in the AR 12673 from the beginning until the X2.2 flare happened. Reprinted from Yang et al. (2017).

the AR played important roles in the X2.2 and X9.3 flares (Yan et al., 2018; Inoue et al., 2018).

5.2 DAI analysis of AR 12673

We studied the magnetic field of the AR NOAA 12673 during one day period of intense solar flares on 2017 September 6. Using vector magnetic field of SHARP data produced by SDO, we reconstructed coronal magnetic field of the active region before and after the X2.2 and X9.3 flares. We applied the DAI analysis to study the stability of this active region, especially when the strongest flare happened. Due

to the complexity of magentic system in this AR, we applied a new method to determine the corresponding flux rope and magnetic flux that are relevant for the DAI analysis.

The similar procedure for studying AR 11158 was also applied for this AR. First, we reconstructed the NLFFF of AR 12673 by using 1-hour cadence SHARP data from 01:00 - 16:00 UT on September 6th, 2017. The NLFFFs were reconstructed using MHD relaxation method applied to the 360×240 grid, which was reduced from its original SHARP data with 688×448 pixels using CONGRID function in IDL. The magnetic field in the reduced data was normalized by 2745 G. After that, magnetic twist for every field line was calculated by using equation 4.2. Finally, we calculated the $\kappa^*_{T_c}$ for each data time to see the evolution of $\kappa^*_{T_c}$ before and after the flares.

Figure 5.3(a) shows the vertical component of magnetic field (Bz) of AR 12673 at 08:36 UT that we used as a boundary condition for extrapolating coronal field. The reconstructed coronal magenetic field of the given boundary condition in figure 5.3(a) is shown in figure 5.3(b). NLFFF shows that the coronal field near the PIL was strongly twisted and large current density was accumulated there. This implies that free magnetic energy was also accumulated in the corresponding region, therefore it was likely that the flare could occur from this region. Indeed, the X2.2 and X9.3 flares happened initially in this region as it shown by the AIA 1600 Å observations (see figure 5.4).

The DAI analysis is based on the theory of the DAI, which analyzed the critical instability state of a double-arc loop as a simplest form of a flux rope within the influence of the external field. Therefore, it is important to apply the DAI analysis to a magnetic system where a flux rope is present, which is responsible for the initiation of a flare. In the simple bipole AR, it is not difficult to identify such a region, where free magnetic energy is accumulated near the main PIL. However, in the complex AR, where complicated PILs separate field lines with different connectivities, identifying the region that should be correctly analyzed by the DAI analysis can be somewhat

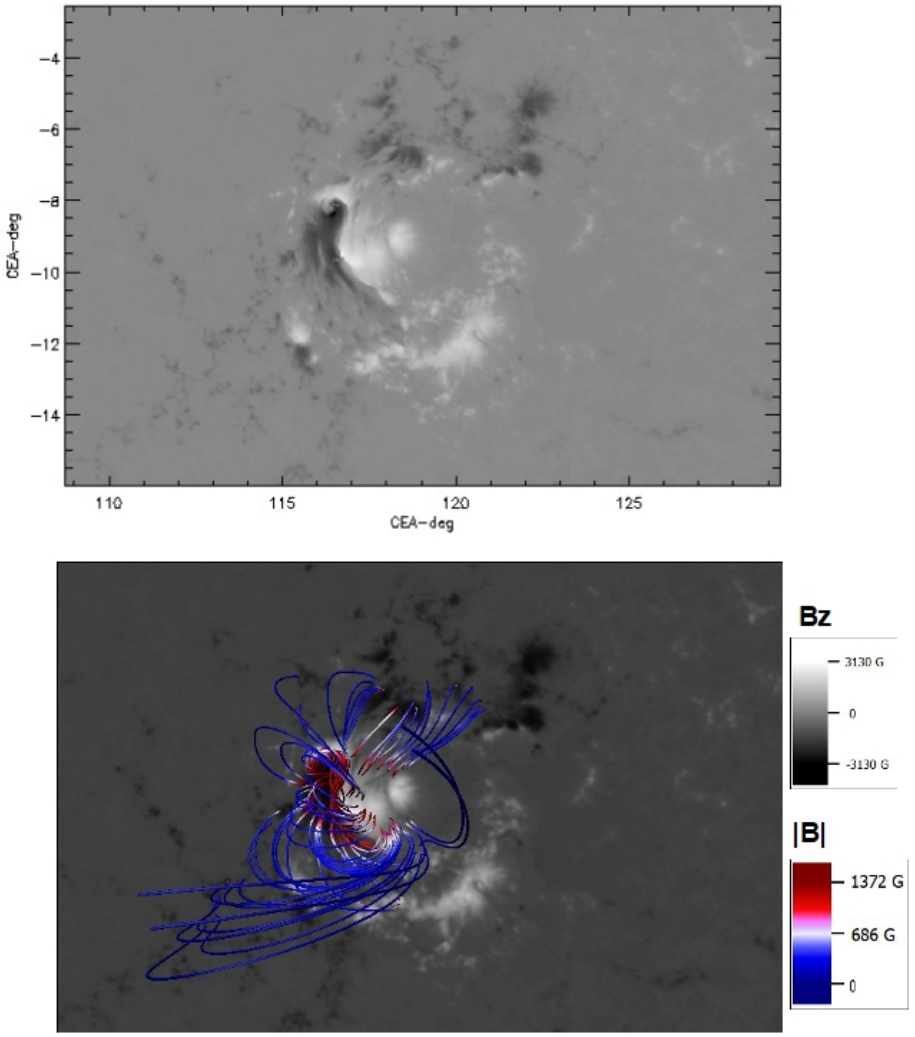

FIGURE 5.3: Bz of the AR 12673 in the CEA coordinate given by SHARP data at 08:36 UT on September 6, 2017, before the X2.2 flare happened and (b) the NLFFF model calculated using MHD relaxation method.

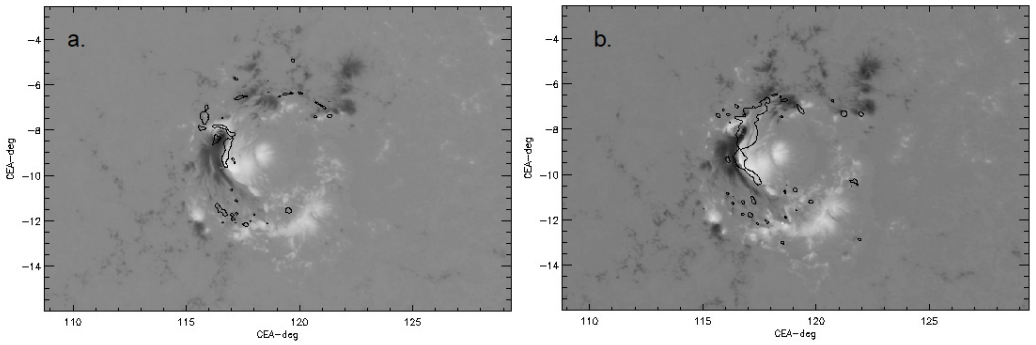

FIGURE 5.4: Bz of the AR 12673 in the CEA coordinate given by SHARP data at (a) 08:36 UT on September 6, 2017, before the X2.2 flare happened and (b) at 08:36 UT, before the X9.3 flare happened. The black contours indicate the brightening of the AIA 1600 Å at the beginning of the flares.

difficult. Applying the DAI analysis for the improper region in the AR can give us the wrong estimation of the flux rope as well as the total flux, which finally lead to the irrelevant $\kappa^*_{T_c}$ value.

Due to the complexity of the AR 12673, applying DAI analysis is more challenging than to apply it for the previous AR (AR 11158). This is because the AR 12673 was very dynamics and had very complicated connectivity. In order to help us in identifying the proper region, we made a squashing map of this AR that can give us information of the location of the quasi separatrix layer (QSL). QSL acts as a separatrice, which separates between two region with different field connectivity, although there is no actual mathematical discontinuity of the field line mapping (Priest and Démoulin, 1995). Therefore, QSL is the region where the magnetic field is significantly changing, but it is still continue (Janvier, 2017). Suppose we define the footpoints of a field line in the photosphere by (x_1, y_1) and (x_2, y_2). Then, the Jacobian matrix of the associated mapping from (x_1, y_1) to (x_2, y_2) is

$$D_{12} = \begin{pmatrix} \partial x_2/\partial x_1 & \partial x_2/\partial y_1 \\ \partial y_2/\partial x_1 & \partial y_2/\partial y_1 \end{pmatrix} \equiv \begin{pmatrix} a & b \\ c & d \end{pmatrix}. \tag{5.1}$$

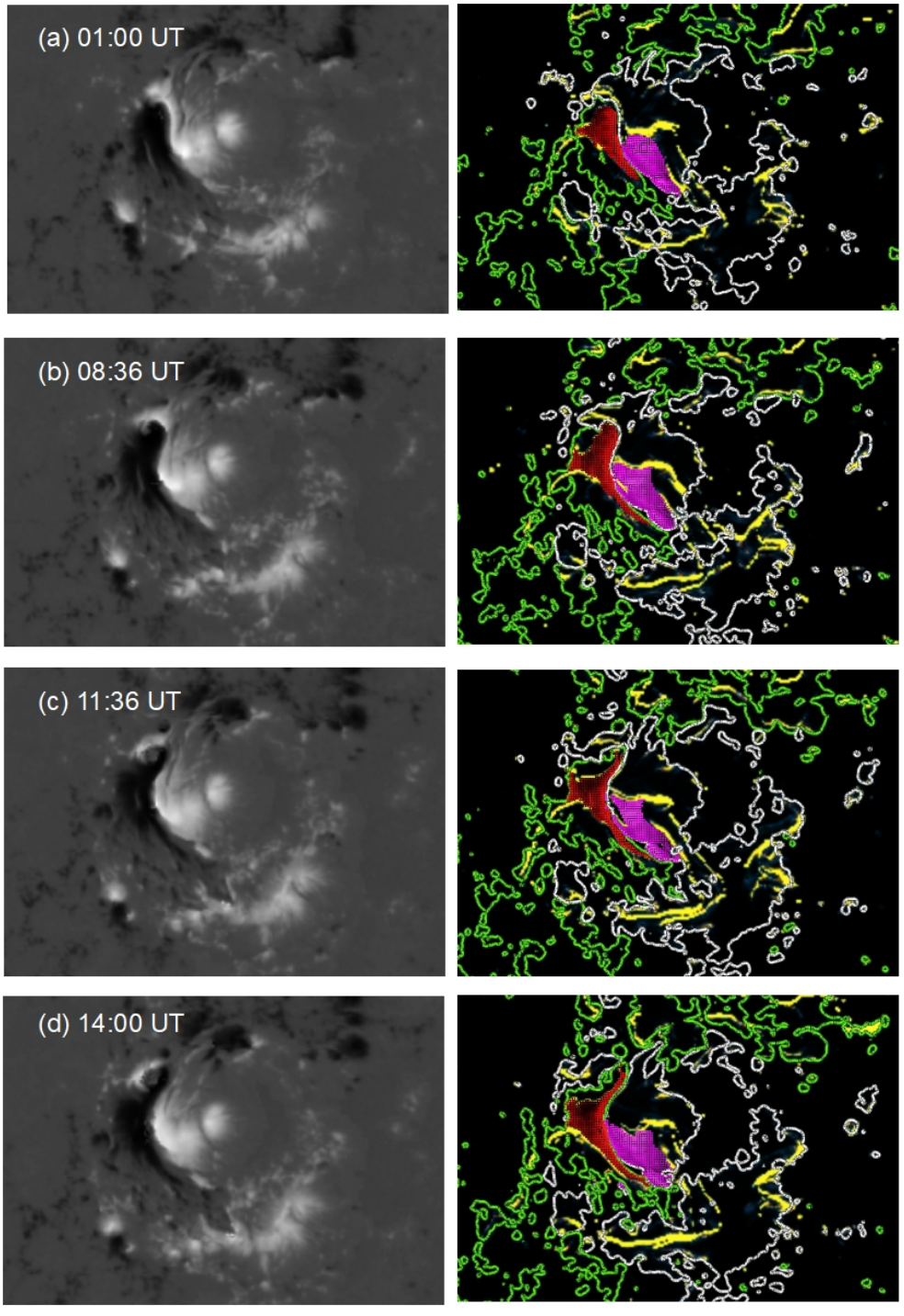

FIGURE 5.5: B_z of the AR 12673 in the CEA coordinate given by SHARP data at (a) 01:00 UT, (b) 08:36 UT, (c) 11:36 UT, and (d) 14:00 UT on September 6, 2017, respectively. The corresponding Q-maps are shown in the right panel. Yellow contours show the high-Q value (QSL) on the photosphere. White (green) contours show the region with 275 G and (-275 G) respectively. Purple (red) shaded regions show the region with positive (negative) flux polarity, where we use to calculate the $\kappa^*_{T_c}$.

We can define the squashing factor (Q) associated with the mapping as

$$Q \equiv \frac{a^2 + b^2 + c^2 + d^2}{|B_{n,1}(x_1, y_1)/B_{n,2}(x_2, y_2)|}, \tag{5.2}$$

where $B_{n,1}(x_1, y_1)$ and $B_{n,2}(x_2, y_2)$ are the normal components of the magnetic field in the photosphere on both of the footpoints (Titov et al., 2002; Liu et al., 2016). The larger the Q-value of the mapping, the more drastic the magnetic field connectivity changes compared to its neighbour field. The QSL is defined as the layer with highest Q-value in the local region. The squashing (Q) maps of the AR 12673 are shown in figure 5.5. This figure shows the cross-section of a QSL in the photosphere of the AR.

To have the Q-map of the complex AR like AR 12673 was very important since it can provide us information of the field connectivity in the AR. Therefore, we could exactly identify the region in which the flaring site was located. This region contained the main flux rope that was analyzed using the DAI analysis. Based on figure 5.4, we could see the two flares coming from the region near the main PIL, where magnetic field was strongly twisted (see figure 5.3). By using connectivity map given by squashing value distribution in the photosphere and the location of the initial brightening of the flares, we could determine the region whose magnetic field has connectivity related to the initial flaring site. The purple and red shaded regions in figure 5.5 represent the area where we obtained the total flux (ϕ_{tot}) for the equation 4.1. We analyzed the evolution of this region from time to time and then calculated $\kappa^*_{T_c}$.

5.3 Results and Interpretation

In order to determine the threshold of high-twist field, we plotted the histogram of the magnetic twist distribution in this region (see figure 5.6). We found that until 06:00 UT, only few field lines have twist more than one turn (figure 5.6(a)).

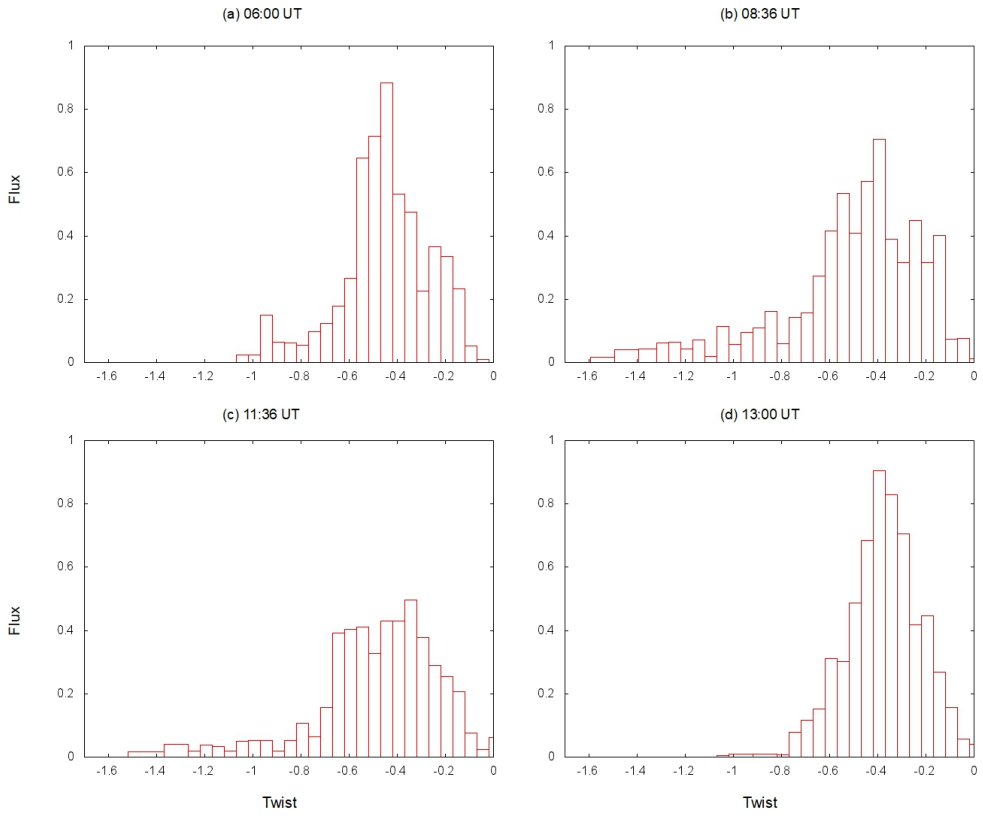

FIGURE 5.6: Magnetic twist distribution calculated for the purple shaded region in figure 5.5, which is the flux in the positive polarity region.

Unfortunately, magnetogram data were unavailable after 06:00 UT for about two and a half hours. The data was again available at around 08:36 UT, when X2.2 flare occured 20 minutes later. However, just about 20 minutes before the X2.2 flare started, large portion of the magnetic field was strongly twisted to more than one turn (figure 5.6(b)). This situation did not significantly change after the X2.2 flare until the X9.3 flare happened (figure 5.6(c)). After the X9.3 flare, most of the high twist field, which has more than one turn negative twist, disappeared to the level slightly above -0.7 turn. Using this information, we employed the DAI analysis to the core of the AR 12673 by using -0.7 as the threshold of high twist field. We calculated the $\kappa^*_{-0.7}$ for the positive and negative flux, as well as the average of them. The result of the $\kappa^*_{-0.7}$ evolution is shown in figure 5.7. It is clear that $\kappa^*_{-0.7}$ increased

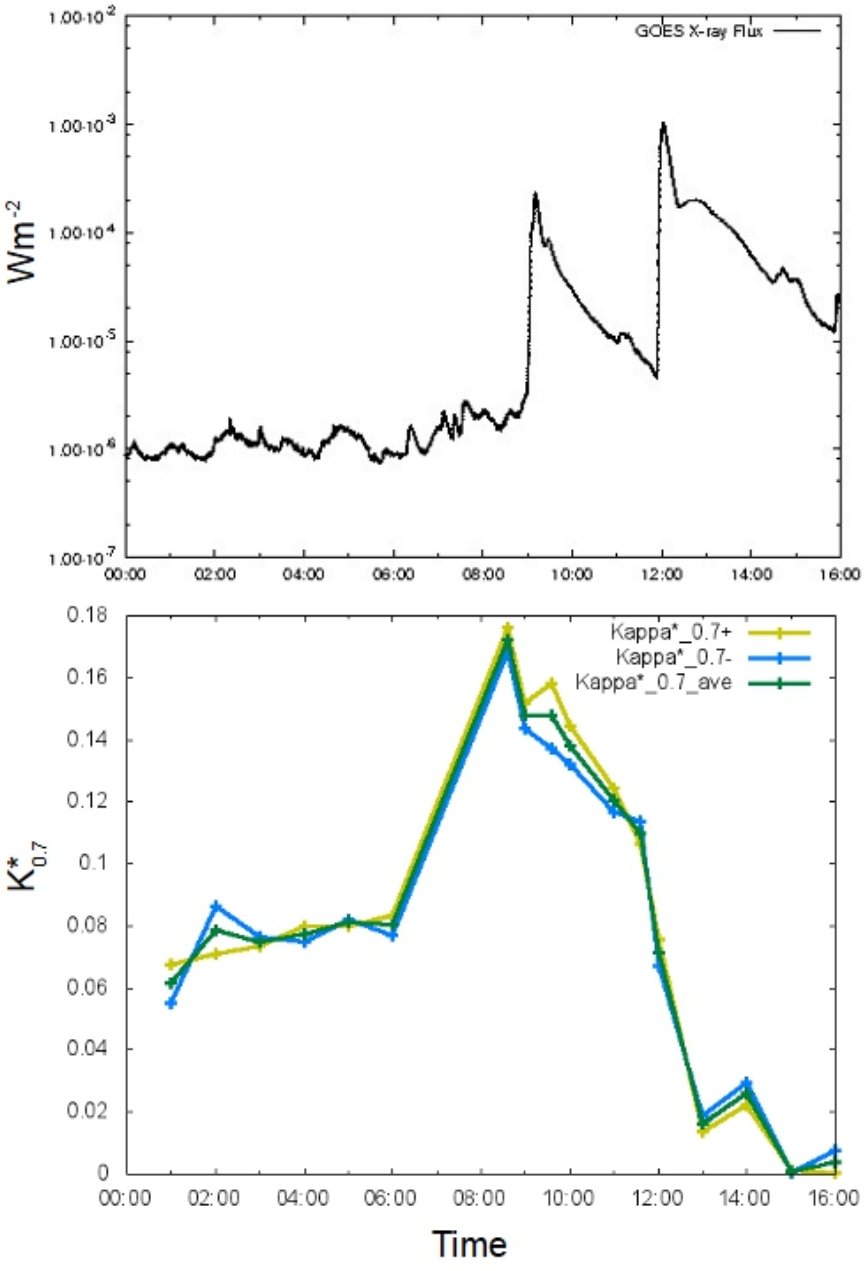

FIGURE 5.7: GOES 1-8 Å X-ray flux (top) and $\kappa^*_{-0.7}$ of the AR 12673 (bottom) from 01:00 UT to 16:00 UT. Yellow and blue lines in the bottom panel show the $\kappa^*_{-0.7}$ calculated from the positive and negative polarity, respectively, meanwhile the green line shows the average value.

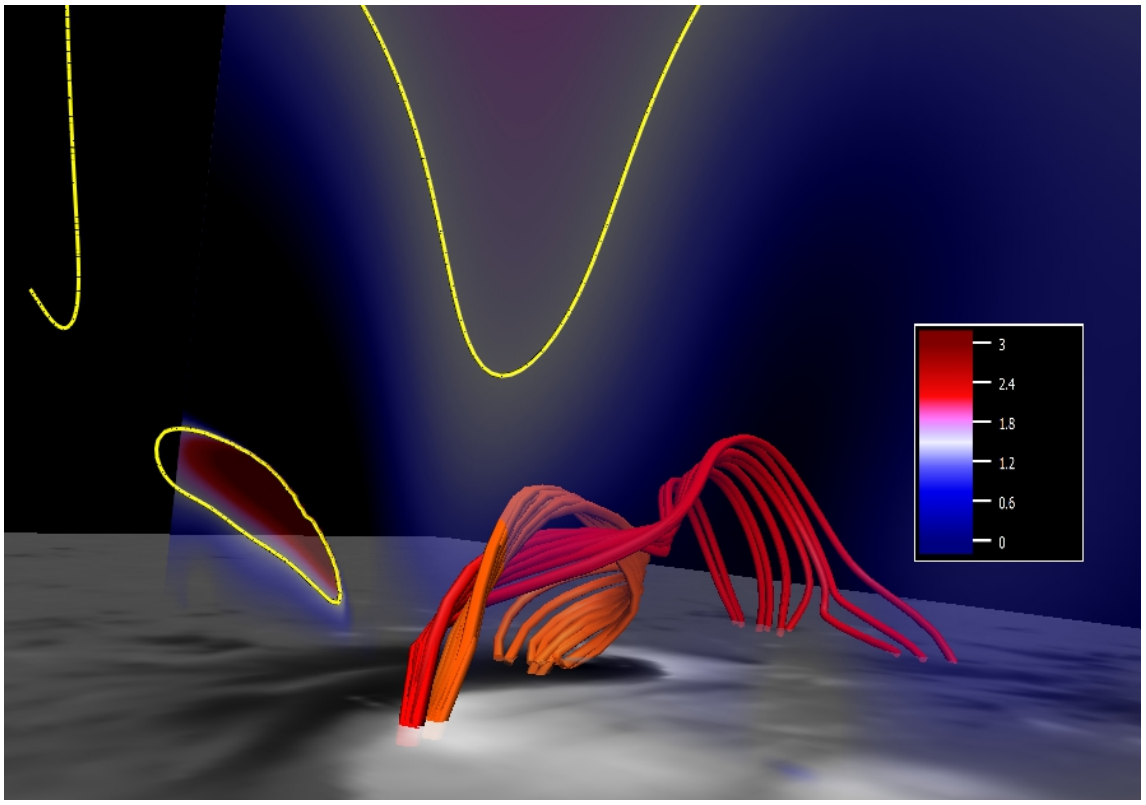

FIGURE 5.8: Selected high twist magnetic field lines above the core region of the AR 12673. Orange and red color field lines represent magnetic field lines with different connectivity. Colorbar corresponds to the decay index value. Yellow contours correspond to the decay index with value 1.5.

dramatically before the X2.2 flare. This rapid rise can also be well described by the rapid enhancement of strong twist magnetic field about 3 hours before the flare as it is shown in figure 5.6. The $\kappa^*_{-0.7}$ reached its peak just on the onset time of the X2.2 flare. This $\kappa^*_{-0.7}$ did not significantly decreased after for about 3 hours. It shows that this AR was still unstable as well as contained a lot of magnetic energy. However, after the X9.3 flare $\kappa^*_{-0.7}$ suddenly decreased, which implies that the AR was probably in the stable state.

The peculiar thing about the time profile of the $\kappa^*_{-0.7}$ appeared after the X2.2 flare happened, since the $\kappa^*_{-0.7}$ value did not decrease significantly after the flare. This trend was somewhat different from other results as have been shown in previous events. Why did this happen? To understand the eruptive behavior of the AR

during these two flares, we analyzed the occurrence of CMEs within the same period. We found that for the X2.2 flare, there was only small CME observed associated with this flare. It implies that the coronal magnetic structure of this AR tend to be confined even when the large flare happened. This might be due to the overlying field was strong enough to keep the flux rope above the AR so that it could still potentially erupt in the near future. This is why the $\kappa^*_{-0.7}$ only slightly decreased, but was still relatively high (> 0.1). On the other hand, we found there was a very big CME happened after the X9.3 flare. This CME implies that the magnetic structure above the AR has changed significantly and the high twist flux rope has been erupted to the interplanetary space. Therefore, $\kappa^*_{-0.7}$ significantly decreased due to the disappearance of the flux rope.

In order to analyze the possibility of the torus instability that worked during the eruption of the flux rope, we plotted the decay index in the core of the AR in figure 5.8. The decay index here was defined as $n = -z/B_{ex}(\partial B_{ex}/\partial z)$, following Inoue et al. (2018). Here, n is decay index. B_{ex} is the horizontal component of the external field, which is the potential field. It is found that the high twist field lines (flux rope) was still located below the threshold of the decay index for torus instability, which is $n > 1.5$. We suggest that during the X2.2 flare, flux rope did not reach the layer of the torus instability threshold. On other hand, the X9.3 flare was large enough to bring the flux rope to reach the torus instability threshold, and therefore the eruption could take place and observed as a CME.

Our finding suggests that the DAI analysis is more relevant to be applied for the occurrence of a flare instead of CME (i.e. eruption). This can be explained by the assumption made in the original work of Ishiguro and Kusano (2017) in which they studied the instability analysis of a double arc structure under the constraint of limited height. Since the DAI analysis is applicable for the limited height, it can only capture the flux rope eruption until it reaches a torus shape. When the torus shape formed, torus instability may dominantly work, and therefore torus instability analysis should be taken into account. Our result confirms the study of Ishiguro

and Kusano (2017) that the DAI analysis is applicable in the flare domain instead of CME.

Chapter 6

Discussions

6.1 Improvement of the κ^* Calculation

We have shown that $\kappa^*_{T_c}$ can give us some information of how the magnetic field in the AR 11158 evolved and became unstable to the DAI, especially before the large flares happened. Since the calculation of the DAI is strongly based on the coronal field extrapolation by NLFFF model, it is important to check how well the model is. It has been shown in Chapter 1 and 2 that the MHD relaxation method is a method to solve a boundary value problem, which is given by magnetogram data. Therefore, the magnetogram data used as a bottom boundary layer in the MHD relaxation method have a very crucial role in the NLFFF model as well as the calculation of $\kappa^*_{T_c}$ that we used to analyze the DAI of the AR. Since it will determine the overall calculation of the $\kappa^*_{T_c}$, evaluating this issue can also be used to improve the validity of the DAI analysis. In this section, we discuss how the quality of the SHARP data that we used for calculating $\kappa^*_{T_c}$, especially if we consider the signal to noise ratio.

6.1.1 Constraining Signal to Noise Ratio of the SHARP data

Vector magnetogram data obtained from SHARP database consist of three components of vector field. Since the value of magnetic field in each grid is obtained by the inversion of HMI Stokes data from the observation, this value may have some errors that should be considered. Fortunately, SHARP team [1] provides the error for each component that is derived from the statistical errors during the inversion. Each error in each component (Bp_err, Bt_err, and Br_err) shows the computed uncertainty (standard deviation) of the phi, theta, and radial component, respectively. We can consider this error as a noise in each pixel of the magnetogram data that we use to calculate the signal to noise ratio (SNR). Therefore, here we define the signal to noise ratio of each pixel as:

$$SNR_p = \frac{Bp}{Bp\_err}, \tag{6.1}$$

$$SNR_t = \frac{Bt}{Bt\_err}, \tag{6.2}$$

$$SNR_r = \frac{Br}{Br\_err}, \tag{6.3}$$

We have mentioned earlier in Chapter 4 that we have selected the region for calculating the $\kappa^*_{T_c}$ based on the strength of magnetic field, particularly that have closed field line within the core region where the X2.2 and X9.3 flares happened. In this study, we chose arbitrary value for the minimum threshold of the radial component flux, which is about 140 G. This is based on the fact that the NLFFF in the weak field region tends to have big noise because the magnetic field lines can be extremely

[1] (http://jsoc.stanford.edu/doc/data/hmi/sharp/sharp.htm)

twisted. However, this does not guarantee that the magnetogram data for the strong field region has high SNR. Therefore, we discuss how the distribution of the SNR and how is the relation of the selection of strong field to the high SNR data.

To understand the quality of the data that we used for calculating the $\kappa^*_{T_c}$ in the AR 11158, we plot the distribution of the SNR after we reduced the data size of the errors using the same function when we reduced the vector magnetogram data. As a sample, we show in figure 6.1 the SNR of vector magnetic field data on February 15, 2011 at 15:00 UT. Here, Bp_err, Bt_err, and Br_err is represented as Bx, By and Bz, respectively. It can be seen from figure 6.1 that most of the strong field area is occupied with high SNR data in all components of vector field. It means that the selection of strong field region can work effectively to separate the low SNR in the calculation of $\kappa^*_{T_c}$ for this AR.

Since the calculation of $\kappa^*_{T_c}$ depends only on the magnetic flux of the radial component, as we described in equation 4.1 in Chapter 4, we focus on the evaluation of the distribution of $\mathrm{SNR_r}$. We plot the $\mathrm{SNR_r}$ of the selected times from February 13 to February 15, 2011 in figure 6.2. This figure shows that almost all the region that we used to obtain the flux for calculating $\kappa^*_{T_c}$ have SNR more than 10. It means that the selection of the region for calculating $\kappa^*_{T_c}$ based on the field strength can automatically avoid the use of low SNR data in this AR. However, it should be noted that it does not guarantee that the same result will be obtained for different ARs. We suggest that the selection of the region to calculate the $\kappa^*_{T_c}$ should consider the SNR as well as the field strength to improve the certainty of the result.

6.2 Force-Freeness of the NLFFF Model

As has been described in Chapter 1, using photospheric magnetic field data in the relaxation method does not guarantee that the extrapolated coronal magnetic field is perfectly force-free. This situation requires evaluation of the Lorentz force remaining

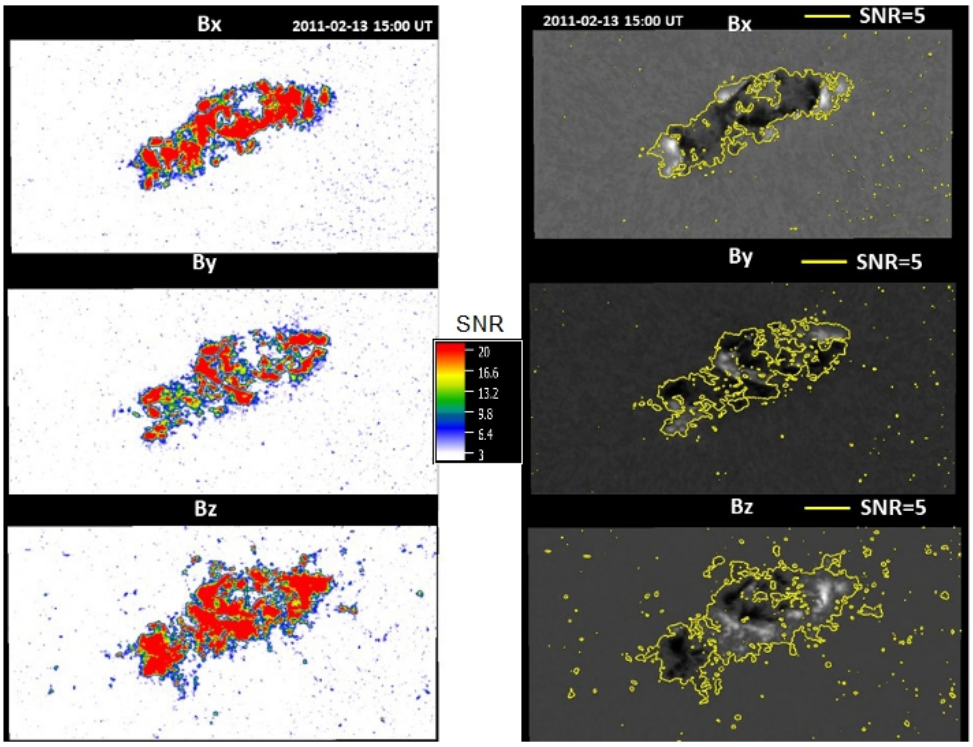

FIGURE 6.1: SNR of vector magnetic field data on February 15, 2011 at 15:00.

within the numerical box at the final step as well as to check the solenoidal condition. Good NLFFF extrapolation can be examined at least by evaluating two things, how small the Lorentz force exists in the model and how close the magnetic field to the solenoidal condition. In order to evaluate the NLFFF of the AR 11158 in our study, we present in figure 6.3 the total Lorentz force and the divergence **B** in the calculation box during the relaxation time to the final step. This figure shows that the divergence **B** reached a small number at the final step to the order of 10^{-5}, while the Lorentz force was in the order of 10^{-3}. The fact that the NLFFF model has finite number of divergence **B** and Lorentz force should be realized as limitations of the NLFFF extrapolation used in this study. Therefore, comparing the NLFFF model with coronal images from the observation is necessary to make sure that the extrapolated coronal field is not far from the reality.

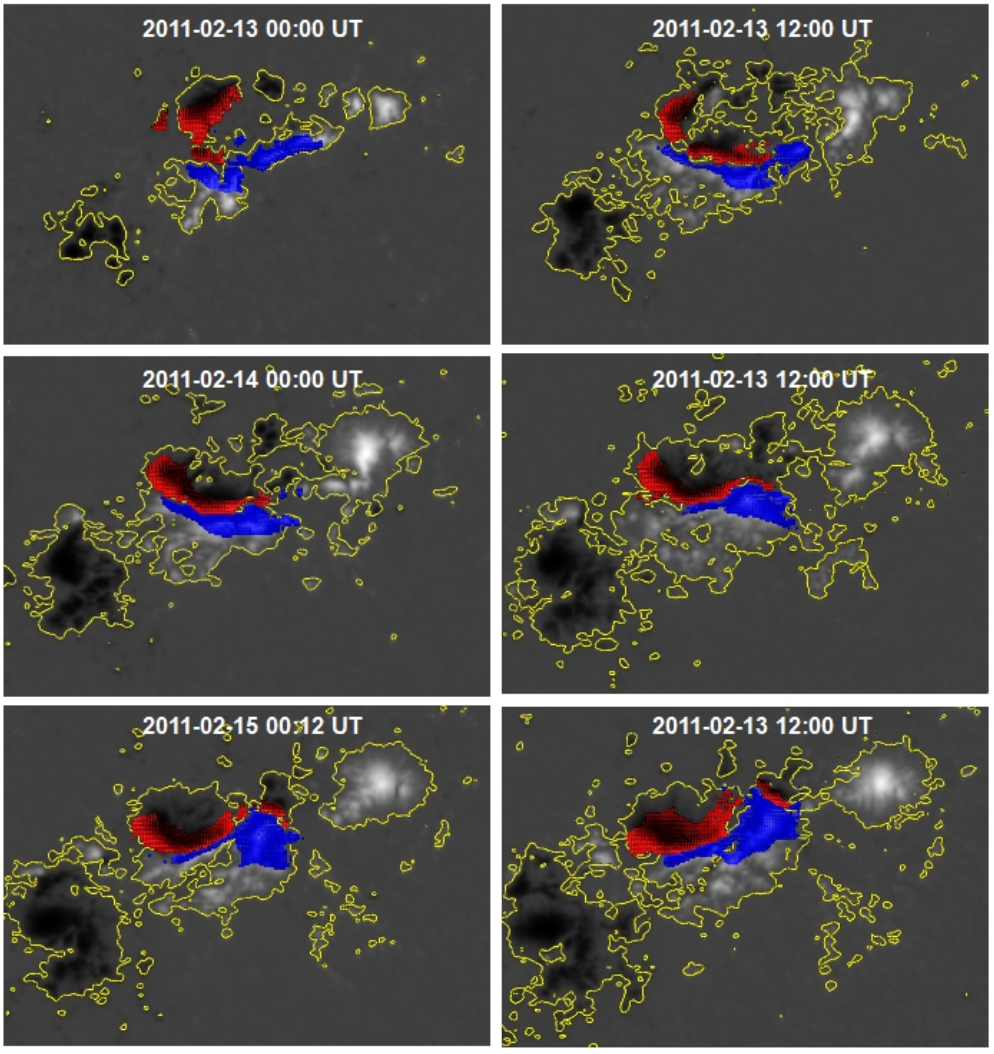

FIGURE 6.2: Selected distribution of SNR of vector magnetic field data on February 13 to February 15, 2011. Yellow contours show the SNR=10. Blue (red) shaded region shows the region where the positive (negative) magnetic flux was selected for calculating the $\kappa^*_{T_c}$.

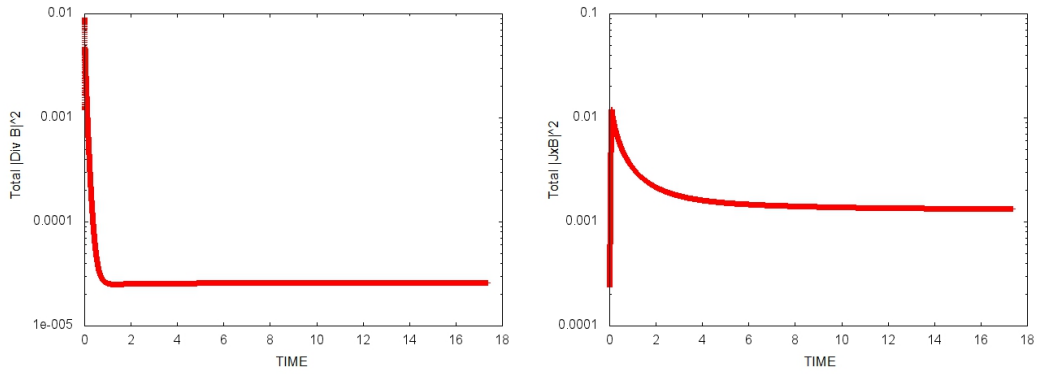

FIGURE 6.3: Divergence B and Lorentz Force profiles during the relaxation time for the NLFFF extrapolation of AR 11158 at 2011-02-15 01:00 UT before the X2.2 flare happened.

Another limitation of the MHD relaxation method is that this method does not guarantee that the force-free α along the field line is uniform. Figure 6.4 shows how the variation of α along the field line traced from arbitrary location. Although α tends to vary around a certain value, there is a deviation from the mean value (green line), particularly near the photosphere. This can be understood since the photospheric field itself is not force-free. Therefore, tracing one field line from one point in the photosphere with $\alpha = \alpha_1$ will not guarantee that the end point will have the same α_1. This condition will make the α along the field line also varies with length.

Non-uniform α in the NLFFF model has a further consequence in the calculation of magnetic twist for each field line. Since magnetic twist is defined as the integration of α along the field line, see equation 1.19, the result of magnetic twist for non-uniform α will give the same result as the integration of $\overline{\alpha}$ along the field line. Here, $\overline{\alpha}$ is the average α along the field line. This means that the calculated magnetic twist represents the twist of a field line with uniform $\overline{\alpha}$ along the field line. In order to evaluate the variation of α along the field line, one can calculate the standard deviation of α as $s\alpha$. Using 95 % confidence level, one can calculate margin of error for α in each field line as $m\alpha$. If we consider this margin of error in the calculation

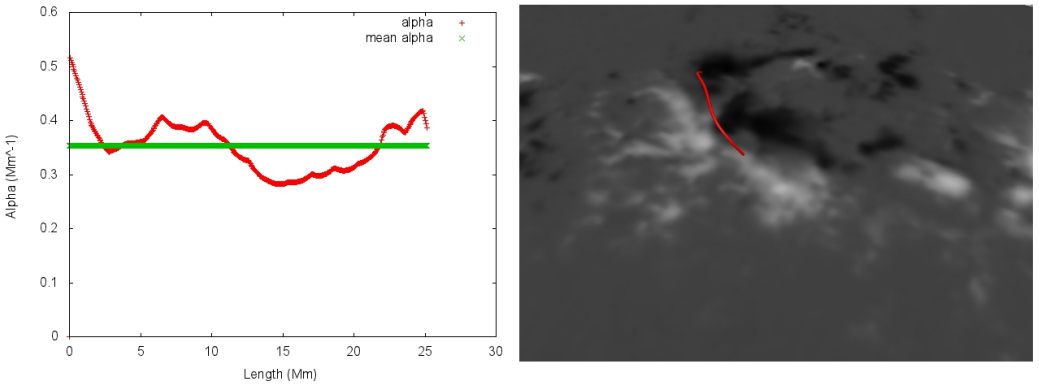

FIGURE 6.4: Variation of α along the selected field line traced from position (0.015,0.0225) in the computational box.

of twist for each field line, we can obtain the maximum and minimum twist value as the integration of $\overline{\alpha} + m\alpha$ and $\overline{\alpha} - m\alpha$ along the field line, respectively. Using this maximum and minimum twist, we calculated again the $\kappa^*_{T_c}$ and defined these as the errorbars for each time. The evolution of $\kappa^*_{T_c}$ and its errorbars is plotted in figure 6.5. From this figure, we can see that the significance increase of $\kappa^*_{T_c}$ before the flares and the dramatic decrease of $\kappa^*_{T_c}$ after the flares were beyond the range of errorbars. Therefore, we can say that the increase and decrease of $\kappa^*_{T_c}$ before and after the flares were due to the significant change of the magnetic field in the AR.

By considering some limitations of the NLFFF extrapolation method, we should notice that the extrapolation field may not capture all features and structures of the real coronal field. However, we have shown that the general structure of the coronal field can be reproduced, particularly in the core of the AR (see figure 4.1). Moreover, our result shows that even when we used extrapolated coronal field to calculate $\kappa^*_{T_c}$, the evolution of $\kappa^*_{T_c}$ was still consistent with the DAI theory.

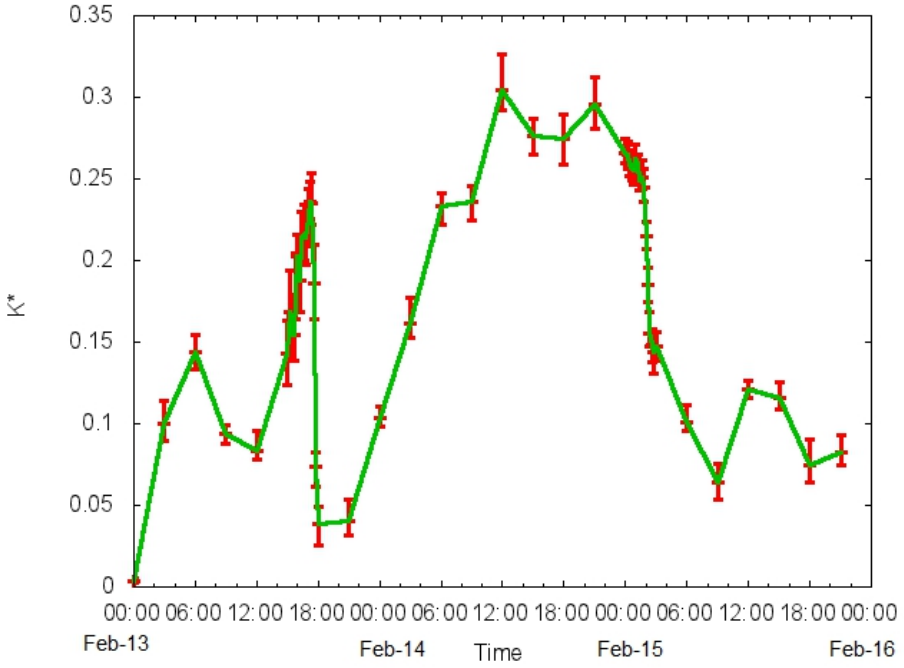

FIGURE 6.5: $\kappa^*_{0.5}$ evolution of AR 11158 with the errorbar.

6.3 Double Arc Instability Analysis of the Cases from the Simulations

We have shown in Chapter 3 how the proper orientation of emerging magnetic flux in the highly sheared magnetic field along the PIL could trigger eruption (flare) in an AR. In this section, we used the result of the simulations in Chapter 3 to analyze the $\kappa^*_{T_c}$ and compared it with the the κ, which was derived from the original definition by Ishiguro and Kusano (2017). This study is important to know how well the high twist flux can be used as a proxy for the reconnected flux in the $\kappa^*_{T_c}$ calculation. For a comparison, we studied a case with eruption (case E) and without eruption (case A). Since our simulations were performed to study the initial phase of the flare, the simulations were conducted in a very short period of time. Therefore, in this study

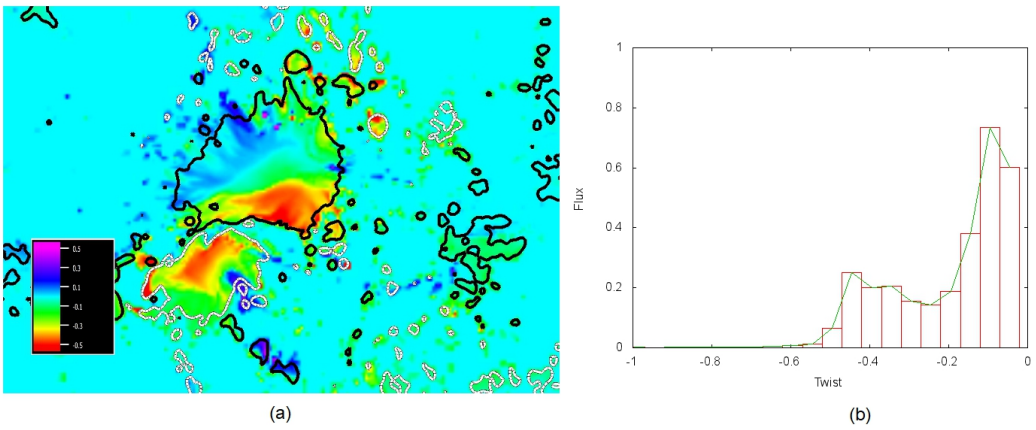

FIGURE 6.6: (a) Magnetic twist map of AR 10930. White (black) contours represents the 400 (-400) Gauss, respectively. (b) Magnetic twist distribution of AR 10930. Flux in the vertical axis is normalized by 1.83×10^{21} Mx.

we only focus on the comparison between the evolution of $\kappa^*_{T_c}$ and κ.

The initial condition for the simulation is the NLFFF extrapolated from the magnetogram data about 6 hours before the X3.4 flare happened. Unfortunately, there was no other data obtained by the Hinode until the X3.4 flare happened, so that we could not calculate nor analyze the evolution of $\kappa^*_{T_c}$ during this period. However, we could still calculate the $\kappa^*_{T_c}$ for the time corresponding to the initial condition in the simulation. First, we calculated magnetic twist of each field line and analyzed the distribution of the twist. Figure 6.6 shows the magnetic twist map (a) and twist distribution (b) of the magnetic field of the AR 10930. Based on its twist distribution, most of the magnetic field lines in the AR 10930 have twist less than 0.5 turn. The relatively high twist region was concentrated in the core of the AR, where the emerging flux was located in between the positive and the negative polarity regions. We calculated the $\kappa^*_{T_c}$ with $T_c = -0.4$, considering the twist distribution in figure 6.6(b). We found that the $\kappa^*_{-0.4} = 0.19$. This was relatively high considering this was calculated from the data 6 hours before the flare happened.

For the next step, we calculated the $\kappa^*_{T_c}$ for the magnetic field evolution in the simulation for the eruptive case, which was case E. Since the reconnection happened

after the emerging flux was imposed, we could determine the reconnected flux and also calculate the κ given by the equation 1.23. Here, we defined the reconnected field line as the field line whose connectivity changed as the time proceeds by evaluating the change of one footpoint using equation 3.5. We chose the threshold of the displacement for the reconnected flux is 0.04, which is twice of the diameter of the emerging flux. This threshold was chosen to exclude the reconnected field lines that reconnect with the emerging flux and end up as small loops near the emerging bipole as shown as blue lines in figure 3.5. Consequently, we only considered the reconnected flux corresponding to the field lines that gained their magnetic twist and created a flux rope. Since DAI analysis essentially analyzes the double-arc shape loop, considering reconnected flux that leads to the formation of magnetic flux rope was more preferable in this study.

Figure 6.7 shows how the evolution of the $\kappa^*_{T_c}$ and κ for the simulation in case E, where OP-type emerging flux was imposed to the NLFFF. Here we found that the $\kappa^*_{-0.4}$ has the largest value compared to the others. It is understandable since using smaller value as the high twist threshold will include more flux than the real reconnected flux. On the other hand, reconnection made field lines gained their twist. The higher twist magnetic field lines were formed after the bipole flux was imposed. The evolution shows that the number of magnetic field lines with twist lower than -0.4 increased just after the beginning of emerging flux was imposed but then almost steady after that. However, the number of magnetic field lines with twist lower than -0.6 continuously increased until the emerging flux stopped to emerge. Unfortunately, the simulation was conducted for a short period so we could not see further evolution of $\kappa^*_{T_c}$ and κ for longer time. We believe that in the real eruptive solar flare, $\kappa^*_{T_c}$ will decrease significantly after the eruption because the eruption allows transfer of magnetic helicity to the interplanetary space. Our result shows that high twist flux estimation using $T_c = -0.4$ to calculate $\kappa^*_{-0.4}$ for this particular case always overestimate the reconnected flux. On the other hand, the similar trend of the $\kappa^*_{-0.6}$ with κ indicates that high twist flux can be used as

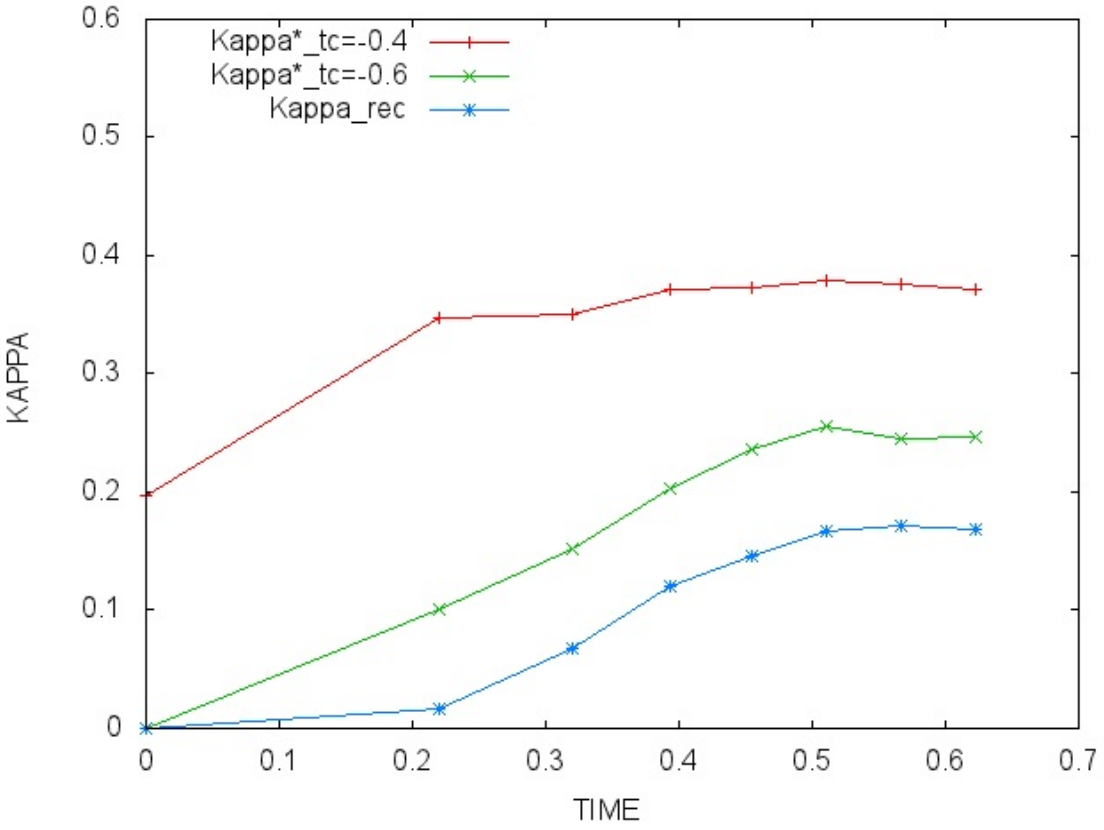

FIGURE 6.7: Evolution of $\kappa^*_{T_c}$ and κ for the simulation in case E. Red, green, and blue lines represent the $\kappa^*_{-0.4}$, $\kappa^*_{-0.6}$, and κ evolution with time. Time in the horizontal axis is normalized so that one unit is corresponding to approximately 100 s.

a proxy of the reconnected flux if we can find the proper value of the high twist threshold (T_c).

The evolution of the $\kappa^*_{T_c}$ and κ for the simulation in case A, where emerging flux whose orientation was almost the same as the average of the large sheared field near the PIL, is shown in figure 6.8. The evolution of $\kappa^*_{-0.4}$ shows similar trend with the $\kappa^*_{-0.4}$ in case E (figure 6.7). However, $\kappa^*_{-0.6}$ just slightly increased and did not show significant change during the simulation time. The same thing happened with the κ that no dramatic increase happened during the simulation. This implies that there was no significant amount of field lines that reconnected and formed a flux rope. Indeed, this case of simulation was one of the cases that the eruption did not occur.

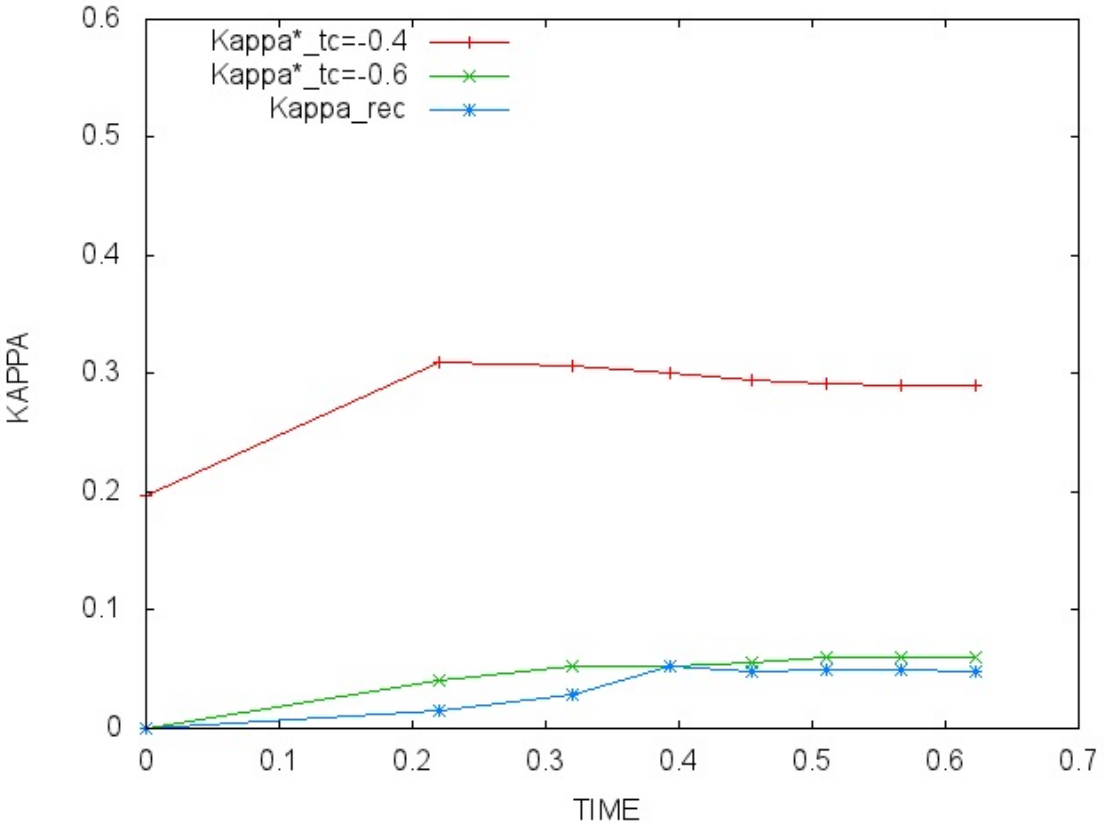

FIGURE 6.8: Evolution of $\kappa^*_{T_c}$ and κ for the simulation in case A. Red, green, and blue lines represent the $\kappa^*_{-0.4}$, $\kappa^*_{-0.6}$, and κ evolution with time. Time in the horizontal axis is normalized so that one unit is corresponding to approximately 100 s.

The DAI analysis performed to the simulation of the eruptive and non-eruptive cases shows that $\kappa^*_{T_c}$ does not exactly represent the true κ derived from the real reconnected flux. $\kappa^*_{T_c}$ with moderate T_c can somewhat represent the overestimation or the upper limit of the true κ. This suggests that $\kappa^*_{T_c}$ is the representation of the capability of the AR to produce a flare. However, the flare onset itself depends on the existence of the proper trigger structure that determines whether the reconnection really happen or not. This finding is consistent with our result in Chapter 4 in which we discuss about the importance of trigger structure.

Chapter 7

Conclusions

In this study, we aimed to analyze solar flare trigger mechanism and stability of the magnetic structures that were formed prior to several big flares by employing MHD simulations and DAI analysis on to the observational magnetogram data. The magnetogram data from Hinode and SDO have been used in this study to extrapolate the coronal magetic field by using MHD relaxation method Inoue et al. (2014b). We employed zero-beta magnetohydrodynamic simulations to the Hinode data by imposing bipole structures with different orientations to examine the trigger scenario proposed by Kusano et al. (2012). We found that several emerging bipole fluxes with the orientation consistent with the OP and RS-type structures proposed by Kusano et al. (2012) could trigger a flare, while other orientations that relatively parallel to the potential field failed to trigger a flare. Our finding confirms previous studies by Kusano et al. (2012); Bamba et al. (2013, 2014); Toriumi et al. (2013); Wang et al. (2017) that solar flares could happen when AR magnetic fields near the PIL had strong shear and perturbed by the emergence of a small bipole with the orientation opposite to the potential field or to the large-scale field in that regions.

Our simulations show that the trigger mechanism proposed by Kusano et al. (2012) can be applied to the real coronal-like magnetic field structure. We also confirmed that the OP and RS-type emerging fields proposed by Kusano et al. (2012) could

trigger a flare in the AR 10930 through different mechanism in the causality of the onset process of solar flare and solar eruption. The OP-type trigger structure tends to trigger a flare through an eruption-induced reconnection in which the emerging flux facilitates the reconnection between the highly twisted field lines that later on erupted and reconnected with the overlying field lines. On the other hand, RS type structure tends to force flare reconnection to happen to drive the eruption. In this study, we succeed to confirm the OP-type trigger structure and mechanism responsible for X3.4 flare in AR 10930, which was proposed by Kusano et al. (2012) based on observation and simulations using an idealized AR model. We also confirmed that the X3.4 could be triggered by the emerging flux situated in the location where a small opposite magnetic field appeared as it suggested by Bamba et al. (2013). We could also show that the proper orientation of the emerging flux produce the similar flare ribbon pattern as it was observed.

Although the trigger structures appear as emerging flux in our simulations, it is possible that the trigger may come from other processes as long as the configuration of the trigger structure exists in the proper way. Several possible ways are a splitting of the sunspot that may lead to a flow towards the PIL (Louis et al., 2014) and a series of bipolar emergence (Toriumi et al., 2013). Kurokawa et al. (2002) showed that such a configuration indeed occurred in a flare-productive active region and could be explained by an emerging twisted flux rope. This emerging twisted flux rope evolved and appeared as a sunspot motion or rotation by means of the kink instability. Although we run the simulations under several constraints of the limited size of the simulation box, large emerging flux, and fast time scale, we demonstrate that MHD simulations can be a powerful tool to examine the trigger process of flares. This study can be important for space weather prediction, especially for the method that rely more on the physics-based approach rather than the statistical approach. However, some improvement of the simulation technique is needed to make the flare and eruption happens with more realistic smaller emerging flux. Some future works to examine the critical size and location of the emerging flux that can trigger a flare

are also important to make a more comprehensive flare trigger models that can be applied for a broader context.

Moreover, we tried to analyze the stability of magnetic structure formed as a consequence of a tether cutting reconnection in the early phase of a flare. We developed a method to analyze the stability of a magnetic system in the AR 11158 by employing double-arc instability theory developed by Ishiguro and Kusano (2017). We demonstrated that the stability of a magnetic field, which is controlled by the κ parameter in Ishiguro and Kusano (2017), can be represented by its proxy $\kappa^*_{T_c}$. We have analyzed the evolution of magnetic twist, $\kappa^*_{T_c}$, and free energy for AR 11158. During the three days of its flare-active period, we found that the magnetic twist and $\kappa^*_{T_c}$ increased before M6.6 and X2.2 flares, and then decreased just after the flares. High-twist magnetic field accumulated in the core of the AR near the PIL before both the flares. We also found that the locations and shapes of the high-twist regions corresponded to the flare ribbons for both the flares, which shows that reconnection during the flares mostly involved high-twist fields in the AR. We found that more high-twist field remained after X2.2 flare in the AR than after M6.6 flare. Accordingly, we suggest that the magnetic field in the AR relaxed considerably after M6.6 flare, but it retained its strong shear after X2.2 flare.

We have examined the values of $\kappa^*_{T_c}$ as a proxy for the parameter κ in order to explore the possibility of using this parameter to analyze the condition required for solar flares. We found that the value of $\kappa^*_{T_c}$ appeared to reach a certain level before a flare happened. This value of $\kappa^*_{T_c}$ decreased significantly after both the flares, and to almost comparable levels. This shows that $\kappa^*_{T_c}$ provides a consistent behavior, so that it may be used to analyze the condition necessary for the occurrence of a solar flare. We suggest that the $\kappa^*_{T_c}$ value is related to the stability condition represented by the κ parameter introduced by Ishiguro and Kusano (2017). We showed that the ratio of the high-twist flux compared to the total flux in the AR can be important to assess the possibility of a solar flare occurrence. It is noted that recently Pariat et al. (2017) found the importance of the ratio of the current helicity to the total helicity

as a possible flare trigger from their parametric simulations. They speculated that this ratio may be related to the instability criterion of the torus instability. Although we investigated high-twist flux instead of helicity, since the helicity and the twist are related, some characteristics between their parameter and κ may also be related. We suggest that during the eruption process, a double-arc structure can develop into a simple torus-like structure in the later phase. When it happens, it is possible that the torus instability will work and the TI threshold will determine the eruption.

Moreover, we found that $\kappa^*_{T_c}$ is very sensitive to the threshold (T_c) chosen to define the high-twist flux. Our analysis shows that the $\kappa^*_{T_c}$ value is more consistent if the threshold T_c is chosen as the maximum twist of the flux remaining after a flare. However, we found that the T_m value is not the same for different flares. Figures 4.2 and 4.4 show that the X2.2 flare had a larger value of T_m than the M6.6 flare. It is still an open issue how to determine the threshold (T_m) before the onset of a flare in order to use $\kappa^*_{T_m}$ to predict a flare. One possibility is that T_m may be related to the flare triggering process in which some disturbance of the magnetic field may play a role. It is likely that the value of T_m should be higher (lower) if a smaller (larger) disturbance causes the triggering reconnection of less (more) flux. Further analysis of the evolution of $\kappa^*_{T_m}$ for many more flares and for non-flaring ARs is required to determine the proper value of T_m. However, the result of our study suggests that DAI analysis can be applied to a real AR in the Sun as long as we can obtain reliable values for the parameters required to calculate the κ.

We have also explored the possibility of applying DAI analysis for a complex AR, which is AR 12673. The complex AR has complicated connectivity that makes it more difficult to determine which part of the AR should be analyzed by the DAI analysis. We proposed that the core region can be identified by observing the initial brightening of the flare as it observed in AIA 1600 Å. Once the core region has been identified, the relevant total flux can be determined by using squashing map in which the main flux rope was located within the region enclosed by a certain QSL. This region contained some bundle of magnetic flux and closed magentic field that has

same field lines connectivity. Therefore, this region was determined as the region whose magnetic flux considered as the the total flux (ϕ_{tot}). As a consequence, flux rope was considered to exist as a high twist field lines within this region.

We found that AR 12673 evolved very dynamically within one day, especially since 3 hours before the X2.2 flare happened. Profile of the $\kappa^*_{-0.7}$ shows that $\kappa^*_{-0.7}$ increased significantly about three hours before the X2.2 flare happened. After the X2.2 flare, $\kappa^*_{-0.7}$ slighly decreased and then dramatically decreased after the X9.3 flare. Our finding shows that the AR might experience condition against the DAI before the X2.2 flare and X9.3 flare. However, after the X2.2 flare, the magnetic field failed to erupt so that the system maintains the strong twist magnetic field in the core region. We found that the first flare (X2.2 flare) was accompanied by small CME while the second (X9.3) flare was followed by large CME. This confirms that the second flare results with the eruption that dramatically changed the magnetic system in the core of the AR. Our result shows that the DAI analysis can be applied for assessing the probability of a flare rather than a CME. This is consistent with the theoretical analysis of DAI by Ishiguro and Kusano (2017) that was developed under the constraint of limited height of the double-arc structure.

We also found that the magnetic energy decreased slightly before the flares, although it increased almost continuously during three days flare-active period. The free energy level in the AR 11158 was different for the two flares we studied. The AR had a higher free energy level before the X2.2 flare than before the M6.6 flare. However, we found that merely using the free energy in an AR is not sufficient to predict the onset of a flare, because it does not contain information about the stability of the magnetic system in the AR. The free energy level can indicate how large class of a flare can be produced by an AR, while $\kappa^*_{T_m}$ may be useful as a parameter to indicate an impending flare in an AR. We believe that further studies based on the DAI analysis and its proxy parameter $\kappa^*_{T_m}$ can be helpful in achieving better understanding of the conditions necessary for a flare.

The use of SHARP magnetogram data as a boundary layer to extrapolate coronal magnetic field should also be complemented with information of errors in each vector field component. Error information can be used to analyze the reliability of the data by calculating the SNR of each pixel. We have shown that the magnetogram data for AR 11158 have very high SNR in the core region, whose magnetic flux has in general greater than 150 G. On the other hand, the weak field region has big errors that is almost comparable to the signal itself. We found that simply by using minimum threshold, we could eliminate errors of the irrational high twist field in the NLFFF as well as most of the low SNR data in the calculation of $\kappa^*_{T_c}$. However, we still suggest that the selection of high SNR data for the calculation of $\kappa^*_{T_c}$ should also need to be conducted in order to improve the reliability of the result, since the data in the strong field region not always have high SNR.

In conclusion, we proposed that the possibility of a solar flare occurrence in an AR can be examined by analyzing the photospheric magnetic field obtained from magnetogram data as well as coronal magentic field reconstructed by NLFFF. Analysis of magnetic twist and magnetic flux in the AR complemented with the trigger structure (i.e. emerging flux) in the photosphere are very promising tools to assess the possibility of the upcoming flare in an AR. Although we only demonstrated our method for big flares in few ARs, we believe that the similar process happen in many other flares. Statistical studies of many more flares from different ARs are certainly required to confirm our study. However, since the numerical simulations and NLFFF extrapolations are quite time consuming and require big computational resources, larger computational systems are expected for this kind of studies. Finally, we expect that the improvement of flare trigger scenario and stability analysis that we studied can be applied in the practical flare forecasting in the future.

References

Alissandrakis, C. E. (1981). On the computation of constant α force-free magnetic field. *Astronomy and Astrophysics*, 100(197):4pp.

Altas, L. (1994). Spotless flare activity. *Solar Physics*, 151:169–176.

Aly, J. J. (1985). Quasi-static evolution of sheared force-free fields and the solar flare problem. *Astronomy and Astrophysics*, 143(19):4pp.

Amari, T., Aly, J. J., Luciani, J. F., Boulmezaoud, T. Z., and Mikic, Z. (1997). Reconstructing the solar coronal magnetic field as a force-free magnetic field. *Solar Physics*, 174:129–149.

Amari, T., Canou, A., and Aly, J. J. (2014). Characterizing and predicting the magnetic environment leading to solar eruptions. *Nature*, 514:465–469.

Antiochos, S. K., DeVore, C. R., and Klimchuk, J. A. (1999). A model for solar coronal mass ejections. *The Astrophysical Journal*, 510:485–493.

Aschwanden, M. J., Sun, X., and Liu, Y. (2014). The magnetic field of active region 11158 during the 2011 february 12-17 flares: Differences between photospheric extrapolation and coronal forward-fitting methods. *The Astrophysical Journal*, 785(34):27pp.

Aschwanden, M. J., Wuelser, J.-P., Nitta, N. V., Lemen, J. R., DeRosa, M. L., and Malanushenko, A. (2012). First three-dimensional reconstructions of coronal

loops with the stereo a+b spacecraft. iv. magnetic modeling with twisted force-free fields. *The Astrophysical Journal*, 756(2):22pp.

Aulanier, G., DeLuca, E. E., Antiochos, A. K., McMullen, R. A., and Golub, L. (2000). The topology and evolution of the bastille day flare. *The Astrophysical Journal*, 540:1126–1142.

Aulanier, G., Démoulin, P., Schrijver, C. J., Janvier, M., Pariat, E., and Schmieder, B. (2013). The standard flare model in three dimensions ii. upper limit on solar flare energy. *Astronomy and Astrophysics*, 549(A66):7pp.

Aulanier, G., Janvier, M., and Schmieder, B. (2012). The standard flare model in threedimensions I. strong to weak shear transition in post flare loops. *Astronomy and Astrophysics*, 543(A110):14pp.

Aulanier, G., Torok, T., Demoulin, P., and DeLuca, E. E. (2010). Formation of torus-unstable flux ropes and electric currents in erupting sigmoids. *The Astrophysical Journal*, 708:129.

Bamba, Y., Inoue, S., Kusano, K., and Shiota, D. (2017). Triggering process of the x1.0 three-ribbon flare in the great active region noaa 12192. *The Astrophysical Journal*, 838(134):16pp.

Bamba, Y., Kusano, K., Imada, S., and Iida, Y. (2014). Comparison between hinode/sot and sdo/hmi, aia data for the study of the solar flare trigger process. *Publication of the Astronomical Society of Japan*, 66(SP1):S16.

Bamba, Y., Kusano, K., Yamamoto, T. T., and Okamoto, T. J. (2013). Study on the triggering process of solar flares based on the hinode/sot observations. *The Astrophysical Journal*, 778(48):13pp.

Bateman, G. (1978). *MHD Instabilities*. Cambridge, MA: Massachussets Institute of Technology.

Benz, A. O. (2008). Flare observations. *Living Reviews of Solar Physics*, 5:1–64.

Berdermann, J., Kriegel, M., Banys, D., Heymann, F., Hoque, M. M., Wilken, V., Borries, C., Heßelbarth, A., and Jakowski, N. (2017). Ionospheric response to the x9.3 flare on 6 september 2017 and its implication for navigation services over europe. *Space Weather*, 16:12pp.

Berger, M. A. and Prior, C. (2006). The writhe of open and closed curves. *Journal of Physics A: Mathematical and General*, 39:8321–8348.

Bobra, M. G. and Ilonidis, S. (2016). Predicting coronal mass ejections using machine learning methods. *The Astrophysical Journal*, 821(127):7pp.

Bobra, M. G., Sun, X., Hoeksema, J. T., Turmon, M., Liu, Y., Hayashi, K., Barnes, G., and Leka, K. D. (2014). The helioseismic and magnetic imager (hmi) vector magnetic field pipeline: Sharps – space-weather hmi active region patches. *Solar Physics*, 289:3549–3578.

Bobra, M. G., van Ballegooijen, A. A., and DeLuca, E. E. (2008). Modeling nonpotential magnetic fields in solar active regions. *The Astrophysical Journal*, 672:1209–1220.

Borrero, J. M., Tomczyk, S., Kubo, M., Socas-Navarro, H., Schou, J., Couvidat, S., and Bogart, R. (2011). Vfisv: Very fast inversion of the stokes vector for the helioseismic and magnetic imager. *Solar Physics*, 273:267–293.

Canfield, R. C., Hudson, H. S., and McKenzie, D. E. (1999). Sigmoidal morphology and eruptive solar activity. *Geophysical Research Letters*, 26(6):627–630.

Carmichael, H. (1964). A process for flares. *AAS-NASA Symposium on Solar Flares ed. W. N. Ness*, NASA SP-50(451).

Carrington, R. C. (1859). *Monthly Notices of the Royal Astronomical Society*, 20(13).

Chen, H., Zhang, J., Cheng, X., Ma, S., Yang, S., and Li, T. (2014). Direct observations of thether-cutting reconnection during a major solar event from 2014 february 24 to 25. *The Astrophysical Journal Letters*, 797(L15):7pp.

Chen, Y., Du, G., Zhao, D., Wu, Z., Liu, W., Wang, B., Ruan, G., Feng, S., and Song, H. (2016). Imaging a magnetic breakout solar eruption. *The Astrophysical Journal Letters*, 820(L37):8pp.

Chiu, Y. T. and Hilton, H. H. (1977). Exact green's function method of solar force-free magnetic-field computations with constant alpha. i - theory and basic test cases. *The Astrophysical Journal*, 212(1):873–885.

Choudary, D. P., Ambastha, A., and Ai, G. (1998). Emerging flux and x-class flares in noaa 6555. *Solar Physics*, 179:133–140.

Clyne, J., Mininni, P., Norton, A., and Rast, M. (2007). Interactive desktop analysis of high resolution simulations: application to turbulent plume dynamics and current sheet formation. *New Journal of Physics*, 9(8):301.

Clyne, J. and Rast, M. (2005). A prototype discovery environment for analyzing and visualizing terascale turbulent fluid flow simulations. In *Electronic Imaging 2005*, pages 284–294. International Society for Optics and Photonics.

Dalmasse, K., Pariat, E., Valori, G., Démoulin, P., and Green, L. M. (2013). First observational application of a connectivity-based helicity flux density. *Astronomy and Astrophysics*, 555(L6):4pp.

Dedner, A., Kemm, F., Kröner, Munz, C.-D., Schnitzer, T., and Wesenberg, M. (2002). Hyperbolic divergence cleaning for the mhd equations. *Journal of Computational Physics*, 175(2):645–673.

Démoulin, P. and Aulanier, G. (2010). Criteria for flux rope eruption: Non-equilibrium versus torus instability. *The Astrophysical Journal*, 718:1388–1399.

DeRosa, M. L., Schrijver, C. J., Barnes, G., Leka, K. D., Lites, B. W., Aschwanden, M. J., amari, T., Canou, A., M, M. J., Régnier, S., Thalman, J. K., Valori, G., Wheatland, M. S., Wiegelman, T., Cheung, M., Conlon, P. A., Fuhrman, M.,

Inhester, B., and Tadesse, T. (2009). A critical assessment of nonlinear force-free field modeling of the solar corona for active region 10953. *The Astrophysical Journal*, 696:1780–1791.

DeRosa, M. L., Wheatland, M. S., Leka, K. D., Barnes, G., Amari, T., Canou, A., Gilchrist, S. A., Thalman, J. K., Valori, G., Wiegelman, T., Schrijver, C. J., malanushenko, A., Sun, X., and Régnier, S. (2015). The influence of spatial resolution on nonlinear force-free modeling. *The Astrophysical Journal*, 811(2):107.

Falconer, D. A., Moore, R. L., and Gary, G. A. (2008). Magnetogram measures of total nonpotentiality for prediction of solar coronal mass ejections from active regions of any degree of magnetic complexity. *The Astrophysical Journal*, 689:1433–1442.

Fan, Y. L., Wang, H. N., He, H., and Zhu, X. S. (2011). Study of the poynting flux in active region 10930 using data-driven magnetohydrodynamic simulation. *The Astrophysical Journal*, 737(39):9pp.

Fletcher, L., Dennis, B. R., Hudson, H. S., Krucker, S., Phillips, K., Veronig, A., Battaglia, M., Bone, L., Caspi, A., Chen, Q., Gallagher, P., Grigis, P. T., Ji, H., Liu, W., Milligan, R. O., and Temmer, M. (2011). An observational overview of solar flares. *Space Science Review*, 159:19–106.

Gary, G. A. (2001). Plasma beta above a solar active region: Rethinking the paradigm. *Solar Physics*, 203:71–86.

Gary, G. A. and Hagyard, M. J. (1990). Transformation of vector magnetograms and the problems associated with the effects of perspective and the azimuthal ambiguity. *Solar Physics*, 126:21–36.

Gibson, S. E., Fan, Y., Török, T., and Kliem, B. (2006). The evolving sigmoid: Evidence for magnetic flux ropes in the corona before, during, and after cmes. *Space Science Reviews*, 124:131–144.

Gilchrist, S. A. and Wheatland, M. S. (2012). A magnetostatic grad-rubin code for coronal magnetic field extrapolations. *Solar Physics*, 282:283–302.

Gold, T. and Hoyle, F. (1960). On the origin of solar flares. *Monthly Notices of the Royal Astronomical Society*, 120(2):89–105.

Golub, L., DeLuca, E., Austin, G., Bookbinder, J., Caldwell, D., Cheimets, P., Cirtain, J., Cosmo, M., Reid, P., Sette, A., Weber, M., Sakao, T ans Kano, R., Shibasaki, K., Hara, H., Tsuneta, S., Kumagai, K., Tamura, T., Shimojo, M., McCracken, J., Carpenter, J., Haight, H., Siler, R., Wright, E Tucker, J., Rutledge, H., Barbera, M., Peres, G., and Varisco, S. (2007). The x-ray telescope (xrt) for the hinode mission. *Solar Physics*, 243:63–86.

Gopasyuk, O. S. (2015). Rotation of sunspots in active region noaa 10930. *Advances in Space Research*, 55(3):937–941.

Guo, Y., Ding, M. D., Cheng, X., Zhao, J., and Pariat, E. (2013). Twist accumulation and topology structure of a solar magnetic flux rope. *The Astrophysical Journal*, 779(157):13pp.

Hagyard, M. J., Smith.Jr., J. B., Teuber, D., and West, E. A. (1984). A quantitative study relating observed shear in photospheric magnetic fields to repeated flaring. *Solar Physics*, 91:115–126.

Hale, G. E. (1908). *The Astrophysical Journal*, 28(315).

Heyvaerts, J., Priest, E. R., and Rust, D. M. (1977). An emerging flux model for the solar flare phenomenon. *The Astrophysical Journal*, 216:123–137.

Hirayama, T. (1974). Theoretical model of flares and prominences. i: Evaporating flare model. *Solar Physics*, 34(2):323–338.

Hodgson, R. (1859). *Monthly Notices of the Royal Astronomical Society*, 20(15).

Hood, A. W. and Priest, E. R. (1979). Kink instability of solar coronal loops as the cause of solar flares. *Solar Physics*, 64:303–321.

Inhester, B., Birn, J., and Hesse, M. (1992). The evolution of line-tied coronal arcades including a converging footpoint motion. *Solar Physics*, 138(2):257–281.

Inoue, S. (2016). Magnetohydrodynamic modeling of coronal magnetic field and solar eruptions based on the photospheric magnetic field. *Progress in Earth and Planetary Science*, 3(19):28pp.

Inoue, S., Hayashi, K., and Kusano, K. (2016). Structure and stability of magnetic fields in solar active region 12192 based on nonlinear force-free field modeling. *The Astrophysical Journal*, 818(168):11pp.

Inoue, S., Hayashi, K., Magara, T., Choe, G. S., and Park, Y. D. (2014a). Magnetohydrodynamic simulation of the x2.2 solar flare on 2011 february 15. i. comparison with the observations. *The Astrophysical Journal*, 788(182):10pp.

Inoue, S., Hayashi, K., Magara, T., Choe, G. S., and Park, Y. D. (2015). Magnetohydrodynamic simulation of the x2.2 solar flare on 2011 february 15. ii. dynamics connecting the solar flare and the coronal mass ejection. *The Astrophysical Journal*, 803(73):19pp.

Inoue, S., Hayashi, K., Shiota, D., Magara, T., and Choe, G. S. (2013). Magnetic structure producing x- and m-class solar flares in solar active region 11158. *The Astrophysical Journal*, 770(79):11pp.

Inoue, S., Kusano, K., Magara, T., Shiota, D., and Yamamoto, T. T. (2011). Twist and connectivity of magnetic field lines in the solar active region noaa 10930. *The Astrophysical Journal*, 738(161):6pp.

Inoue, S., Magara, T., Pandey, V. S., Shiota, D., Kusano, K., Choe, G. S., and Kim, K. S. (2014b). Nonlinear force-free extrapolation of the coronal magnetic field based on the magnetohydrodynamic relaxation method. *The Astrophysical Journal*, 780(101):13pp.

Inoue, S., Magara, T., Watari, S., and Choe, G. S. (2012). Nonlinear force-free modeling of a three-dimensional sigmoid observed on the sun. *The Astrophysical Journal*, 747(1):65.

Inoue, S., Shiota, D., Bamba, Y., and Park, S.-H. (2018). Magnetohydrodynamic modeling of a solar eruption associated with an x9.3 flare observed in the active region 12673. *The Astrophysical Journal*, 867(83):8pp.

Ishiguro, N. and Kusano, K. (2017). Double arc instability in the solar corona. *The Astrophysical Journal*, 843(101):8pp.

Janvier, M. (2017). Three-dimensional magnetic reconnection and its application to solar flares. *Journal of Plasma Physics*, 83(535830101).

Janvier, M., Aulanier, G., Bommier, V., Schmieder, B., Dèmoulin, P., and Pariat, E. (2014). Electric currents in flare ribbons: Observations and three-dimensional standard model. *The Astrophysical Journal*, 788(1):60.

Jiang, C., Wu, S. T., Feng, X., and Hu, Q. (2016). Data-driven magnetohydrodynamic modelling of a flux-emerging active region leading to solar eruption. *Nature Communications*, 7:11522.

Jiang, Y., Zheng, R., Yang, J., Hong, J., Yi, B., and Yang, D. (2012). Rapid sunspot rotation associated with the x2.2 flare on 2011 february 2011. *The Astrophysical Journal*, 744(50):6pp.

Jing, J., Chen, P. F., Wiegelmann, T., Xu, Y., Park, S.-H., and Wang, H. (2009). Temporal evolution of free magnetic energy associated with four x-class flares. *The Astrophysical Journal*, 696:84–90.

Jing, J., Park, S.-H., Liu, C., Lee, J., Wiegelmann, T., Xu, Y., Deng, N., and Wang, H. (2012). Evolution of relative magnetic helicity and current helicity in the noaa active region 11158. *The Astrophysical Journal Letters*, 752(L9):7pp.

Jing, J., Yurchychyn, B., Yang, G., Xu, Y., and Wang, H. (1994). On the relation between filament eruptions, flares, and coronal mass ejections. *The Astrophysical Journal*, 614:1054–1062.

Kliem, B., Lin, J., Forbes, T. G., Priest, E. R., and Török, T. (2014). Catastrophe versus instability for the eruption of a toroidal solar magnetic flux rope. *The Astrophysical Journal*, 789(46):13pp.

Kliem, B., Su, Y. N., van Ballegooijen, A. A., and DeLuca, E. E. (2010). Magneto-hydrodynamic modeling of the solar eruption on 2010 april 8. *The Astrophysical Journal*, 779:314–333.

Kliem, B. and Török, T. (2006). Torus instability. *Physical Review Letters*, 96:255002.

Klimchuk, J. A. and Sturrock, P. A. (1992). Three-dimensional force-free magnetic fields and flare energy buildup. *The Astrophysical Journal*, 385:344–353.

Kopp, R. A. and Pneuman, G. W. (1976). Magnetic reconnection in the corona and the loop prominence phenomenon. *Solar Physics*, 50:85–98.

Kosugi, T., Matsuzaki, K., Sakao, T Shimizu, T., Sone, Y., Tachikawa, S., Hashimoto, T., Minesugi, K., Ohnishi, A., Yamada, T., Tsuneta, S., Hara, H., Ichimoto, K., Suematsu, Y., Shimojo, M., Watanabe, T., Shimada, S., Davis, J. M., Hill, I. D., Owens, J. K., Title, A. M., Culhane, J. J., Harra, L. K., Doschek, G. A., and Golub, L. (2007). The hinode (solar-b) mission: an overview. *Solar Physics*, 243:3–17.

Kubo, M., Yokoyama, T., Katsukawa, Y., Lites, B., Tsuneta, S., Suematsu, Y., Ichimoto, K., Shimizu, T., Nagata, S., Tarbell, T. T., Shine, R. A., Title, A. M., and Elmore, D. (2007). Hinode observations of a vector magnetic field change associated with a flare on 2006 december 13. *Publication of the Astronomical Society of Japan*, 59(sp3):S779–S784.

Kurokawa, H., Wang, T., and Ishi, T. T. (2002). Emergence and drastic breakdown of a twisted flux rope to trigger strong solar flares in noaa active region 9026. *The Astrophysical Journal*, 572:598–608.

Kusano, K., Bamba, Y., Yamamoto, T. T., Iida, Y., Toriumi, S., and Asai, A. (2012). Magnetic field structures triggering solar flares and coronal mass ejections. *The Astrophysical Journal*, 760(31):9pp.

Kusano, K., Maeshiro, T., Yokoyama, T., and Sakurai, T. (2004). Triggering an eruptive flare by emerging flux in a solar active region complex. *The Astrophysical Journal*, 610:537–549.

Leamon, R. J., Canfield, R. C., Blehm, Z., and Pevtsov, A. A. (2003). What is the role of the kink instability in solar coronal eruptions? *The Astrophysical Journal*, 596:L255–L258.

Leka, K. D. and Barnes, G. (2007). Photospheric magnetic field properties of flaring versus flare-quiet active regions. iv. a statistically significant sample. *The Astrophysical Journal*, 656:1173–1186.

Leka, K. D., Barnes, G., Crouch, A. D., Metcalf, T. R., Gary, G. A., Jing, J., and Liu, Y. (2009). Resolving the 180^0 ambiguity in solar vector magnetic field data: Evaluating the effects of noise, spatial resolution, and method assumptions. *Solar Physics*, 260:83–108.

Leka, K. D., Fan, Y., and Barnes, G. (2005). On the availability of sufficient twist in solar active regions to trigger the kink instability. *The Astrophysical Journal*, 626(2):1091–1095.

Lemen, J. R., Title, A. M., Akin, D. J., Boerner, P. F., Chou, C., F, D. J., Duncan, D. W., Edwards, C. J., Friedlaender, F. M., Heyman, G. F., Hurlburt, N. E., Katz, N. L., Kushner, G. D., Levay, M., Lindgren, R. W., Mathur, D. P., McFeaters, E. L., Mitchell, S., Rehse, R. E., Schrijver, C. J., Springer, L. A., Stern, R. A., Tarbell, T. D., Wuelser, J.-P., Wolfson, C. J., Yanari, C., Bookbinder, J. A.,

Cheimets, P. N., Caldwell, D., Deluca, E. E., Gates, R., Golub, L., Park, S., Podgorski, W. A., Bush, R. I., Scherrer, P. H., Gummin, M. A., Smith, P., Auker, G., Jerram, P., Pool, P., Soufli, R., Windt, D. L., Beardsley, S., Clapp, M., Lang, J., and Waltham, N. (2012). The atmospheric imaging assembly (aia) on the solar dynamics observatory (sdo). *Solar Physics*, 275:17–40.

Liu, C., Deng, N., Lee, J., Wiegelmann, T., Moore, R. L., and Wang, H. (2013). Evidence for solar tether-cutting magnetic reconnection from coronal field extrapolations. *The Astrophysical Journal Letters*, 778(L36):7pp.

Liu, C., Deng, N., Liu, R., Lee, J., Wiegelmann, T., Jing, J., Xu, Y., Wang, S., and Wang, H. (2012). Rapid change of photospheric magnetic field after tether-cutting reconnection and magnetic implosion. *The Astrophysical Journal Letters*, 745(L4):7pp.

Liu, R., Kliem, B., Titov, V., Chen, J., Wang, Y., Wang, H., Liu, C., Xu, Y., and Wiegelmann, T. (2016). Structure, stability, and evolution of magnetic flux ropes from the perspective of magnetic twist. *The Astrophysical Journal*, 818(148):22pp.

Louis, R. E., Kliem, B., Ravindra, B., and Chintzoglou, G. (2015). Triggering an eruptive flare by emerging flux in a solar active region complex. *Solar Physics*, 290:3641–3662.

Louis, R. E., Puschmann, K. G., Kliem, B., Balthasar, H., and Denker, C. (2014). Sunspot splitting triggering an eruptive flare. *Astronomy and Astrophysics*, 562:A110.

Lui, W., Chen, Q., and Petroslan, V. (2013). Plasmoid ejections and loop contractions in an eruptive m7.7 solar flare: Evidence of particle acceleration and heating in magnetic reconnection outflows. *The Astrophysical Journal*, 767(168):18pp.

Magara, T. and Tsuneta, S. (2008). Hinode's observational result on the saturation of magnetic helicity injected into the solar atmosphere and its relation to the

occurrence of a solar flare. *Publication of the Astronomical Society of Japan*, 60(5):1181–1189.

Malanushenko, A., Schrijver, C. J., DeRosa, M. L., and Wheatland, M. S. (2014). Using coronal loops to reconstruct the magnetic field of an active region before and after a major flare. *The Astrophysical Journal*, 783(102):15pp.

Masuda, S., Kosugi, T., Hara, H., Tsuneta, S., , and Ogawara, Y. (1994). A loop-top hard x-ray source in a compact solar flare as evidence for magnetic reconnection. *Nature*, 371:495–497.

Metcalf, T. R., Leka, K. D., Barnes, G., Lites, B. W., Georgoulis, M. K., Pevtsov, A. A., Balasubramaniam, K. S., Gary, G. A., Jing, J., Li, J., Liu, Y., Wang, H. N., Abramenko, V., Yurchyshyn, V., and Moon, Y.-J. (2006). An overview of existing algorithms for resolving the 180^0 ambiguity in vector magnetic fields: Quantitative tests with synthetic data. *Solar Physics*, 237:267–296.

Mikić, Z. and McClymont, A. N. (1994). Deducing coronal magnetic fields from vector magnetograms. *ASP Conference Series, Solar Active Region Evolution: Comparing Models with Observations, eds Balasubramaniam, K.S and Simon, G.W*, 68:225.

Min, S. and Chae, J. (2009). The rotating sunspot in ar 10930. *Solar Physics*, 258:203–217.

Moore, R. L., Falconer, D. A., and Sterling, A. C. (2012). The limit of magnetic shear energy in solar active regions. *The Astrophysical Journal*, 750(24):10pp.

Moore, R. L., Sterling, A. C., Hudson, H. S., and Lemen, J. R. (2001). Onset of the magnetic explosion in solar flares and coronal mass ejections. *The Astrophysical Journal*, 552:833–848.

Nakagawa, Y. (1974). Dynamics of the solar magnetic field. i method of examination of force-free magnetic fields. *The Astrophysical Journal*, 190:437–440.

Narukage, N., Sakao, T., Kano, R., Shimojo, M., Winebarger, A., Weber, M., and Reeves, K. K. (2014). Coronal-temperature-diagnostic capability of the hinode/ x-ray telescope based on self-consistent calibration. ii. calibration with on-orbit data. *Solar Physics*, 289(3):1029–1042.

Pariat, E., Leake, J. E., Valori, G., Linton, M. G., Zuccarello, F. P., and Dalmasse, K. (2017). Relative magnetic helicity as a diagnostic of solar eruptivity. *Astronomy and Astrophysics*, 601:A125.

Park, S.-H., Kusano, K., Cho, K.-S., Chae, J., Bong, S.-C., Kumar, P., Park, S.-Y., Kim, Y.-H., and Park, Y.-D. (2013). Study of magnetic helicity injection in the active region noaa 9236 producing multiple flare-associated coronal mass ejection events. *The Astrophysical Journal*, 778(13):8pp.

Parker, E. N. (1963). The solar-flare phenomenon and the theory of reconnection and annihiliation of magnetic fields. *Astrophysical Journal Supplement*, 8:p177.

Peter, H., Warnecke, J., Chitta, L. P., and Cameron, R. H. (2015). Limitations of force-free magnetic field extrapolations: Revisiting basic assumptions. *Astronomy and Astrophysics*, 584(A68):8pp.

Petrie, G. J. D. (2012). The abrupt changes in the photospheric magnetic and lorentz force vectors during six major neutral-line flares. *The Astrophysical Journal*, 759(50):18pp.

Pevtsov, A. A., Berger, M. A., Nindos, A., Norton, A. A., and van Driel-Gesztelyi, L. (2014). Magnetic helicity, tilt, and twist. *Space Science Reviews*, 186(1–4):285–324.

Priest, E. R. and Démoulin, P. (1995). Three-dimensional magnetic reconnection without null points. 1. basic theory of magnetic flipping. *Journal of Geophysical Research*, 100(A12):23443–23464.

Priest, E. R. and Forbes, T. G. (2002). The magnetic nature of solar flares. *The Astronomy and Astrophysics Review*, 10:313–377.

Priest, E. R., Longcope, D. W., and Janvier, M. (2016). Evolution of magnetic helicity during eruptive flares and coronal mass ejections. *Solar Physics*, 291:2017–2036.

Roumeliotis, G. (1996). The "stress-and-relax" method for reconstructing the coronal magnetic field from vector magnetograph data. *The Astrophysical Journal*, 473:1095–1103.

Rust, D. M. and Kumar, A. (1996). Evidence for helically kinked magnetic flux ropes in solar eruptions. *The Astrophysical Journal*, 464:L199–L202.

Rust, D. M. and LaBonte, B. J. (2005). Observational evidence of the kink instability in solar filament eruptions and sigmoids. *The Astrophysical Journal*, 622:L69–L72.

Sakurai, T. (1981). Calculation of force-free magnetic field with non-constant alpha. *Solar Physics*, 69:343–359.

Sakurai, T. (1982). Green's function methods for potential magneti fields. *Solar Physics*, 76:301–321.

Sakurai, T. (1989). Magnetic equilibria and instabilities. *Solar Physics*, 121:347–360.

Savcheva, A., Pariat, E., McKillop, S., McCauley, P., Hanson, E., Su, Y., and DeLuca, E. E. (2016). The relation between solar eruption topologies and observed flare features. ii. dynamical evolution. *The Astrophysical Journal*, 817:22pp.

Scherrer, P. H., Schou, J., Bush, R. I., Kosovichev, A. G., Bogart, R. S., Hoeksema, J. T., Liu, Y., Duvall Jr, T. I., Zhao, J., Title, A. M., Schrijver, C. J., Tarbell, T. D., and Tomczyk, S. (2012). The helioseismic and magnetic imager (hmi) investigation for the solar dynamics observatory (sdo). *Solar Physics*, 275:207–227.

Schou, J., Scherrer, P. H., Bush, R. I., Wachter, R., Couvidat, S., Rabello-Soares, M. C., Bogart, R. S., Hoeksema, J. T., Liu, Y., Duvall Jr, T. I., Akin, D. J., Allard, B. A., Miles, J. W., Rairden, R., Shine, R. A., Tarbell, T. D., Title, A. M.,

Wolfson, C. J., Elmore, D. F., Norton, A. A., and Tomczyk, S. (2012). Design and ground calibration of the helioseismic and magnetic imager (hmi) instrument on the solar dynamics observatory (sdo). *Solar Physics*, 275:229–259.

Schrijver, C. J., DeRosa, M. L., Metcalf, T., Barnes, G., Lites, B., Tarbell, T., McTiernan, J., Valori, G., Wiegelmann, T., Wheatland, M. S., Amari, T., Aulanier, G., Démoulin, P., Fuhrmann, M., Kusano, K., Régnier, S., and Thalmann, J. K. (2008). Nonlinear force-free field modeling of a solar active region around the time of a major flare and coronal mass ejection. *The Astrophysical Journal*, 675:1637–1644.

Schrijver, C. J., DeRosa, M. L., Title, A. M., and Metcalf, T. R. (2005). The nonpotentiality of active-region coronae and the dynamics of the photospheric magnetic field. *The Astrophysical Journal*, 628:501–513.

Shibata, K. and Magara, T. (2011). Solar flares: Magnetohydrodynamic process. *Living Reviews of Solar Physics*, 8(6).

Shibata, K., Masuda, S., Shimojo, M., Hara, H., Yokoyama, T., Tsuneta, S., Kosugi, T., and Ogawara, Y. (1995). Hot-plasma ejections associated with compact-loop solar flares. *The Astrophysical Journal Letters*, 451:L83–L85.

Sturrock, P. A. (1966). Model of the high-energy phase of solar flares. *Nature*, 211(5050):695–697.

Su, J. T., Sakurai, T., Suematsu, Y., Hagino, M., and Liu, Y. (2009). Local twist and current helicity distributions of active region noaa 10930. *The Astrophysical Journal*, 697:L103–L107.

Su, Y., Golub, L., Van Ballegooijen, A., DeLuca, E. E., Reeves, K. K., Sakao, T., Kano, R., Narukage, N., and Shibasaki, K. (2007). Evolution of the sheared magnetic fields of two x-class flares observed by hinode/xrt. *Publication of the Astronomical Society of Japan*, 59(sp3):S785–S791.

Su, Y., Veronig, A. M., Holman, G. D., Dennis, B. R., Wang, T., Temmer, M., and Gan, W. (2013). Imaging coronal magnetic-field reconnection in a solar flare. *Nature Physics*, 9:489–493.

Sui, L., Holman, G. D., and Dennis, B. R. (2004). Evidence for magnetic reconnection in three homologous solar flares observed by rhessi. *The Astrophysical Journal*, 612:546–556.

Sun, X., Hoeksema, J. T., Liu, Y., Aulanier, G., Su, Y., Hannah, I. G., and Hock, A. (2013). Hot spine loops and the nature of a late-phase solar flare. *The Astrophysical Journal*, 778(139):17pp.

Sun, X., Hoeksema, J. T., Liu, Y., Wiegelmann, T., Hayashi, K., Chen, Q., and Thalmann, J. (2012). Evolution of magnetic field and energy in major eruptive active region based on sdo/hmi observation. *The Astrophysical Journal*, 748(77):15pp.

Titov, V., Hornig, G., and Démoulin, P. (2002). Theory of magnetic connectivity in the solar corona. *Journal of Geophysical Research*, 107(A8):1164.

Titov, V. S. and Démoulin, P. (1999). Basic topology of twisted magnetic configurations in solar flares. *Astronomy and Astrophysics*, 351:707–720.

Toriumi, S., Iida, Y., Bamba, Y., Kusano, K., Imada, S., and Inoue, S. (2013). The magnetic systems triggering the m6.6 class solar flare in noaa active region 11158. *The Astrophysical Journal*, 773(128):10pp.

Toriumi, S., Iida, Y., Kusano, K., Bamba, Y., and Imada, S. (2014). Formation of a flare-productive active region: Observation and numerical simulation of noaa ar 11158. *Solar Physics*, 289:3351–3369.

Török, T. and Kliem, B. (2005). Confined and ejective eruptions of kink unstable flux rope. *The Astrophysical Journal*, 630:L97–L100.

Török, T., Kliem, B., and Titov, V. S. (2004). Ideal kink instability of a magnetic loop equilibrium. *Astronomy and Astrophysics*, 413:L27–L30.

Tsuneta, S. (1996). Structure and dynamics of magnetic reconnection in a solar flare. *The Astrophysical Journal*, 456:840–849.

Tsuneta, S., hara, H., Shimizu, T., Acton, L. W., Strong, K. T., Hudson, H. S., and Ogawara, Y. (1992). Observation of a solar flare at the limb with the yohkoh soft x-ray telescope. *Publication of the Astronomical Society of Japan*, 44(5):L63–L69.

Tsuneta, S., Ichimoto, K., Katsukawa, Y., Otsubo, M., Shimizu, T., Suematsu, Y., Nakagiri, M., Noguchi, M., Tarbell, T., Title, A., Shine, R., Rosenberg, W., Hoffman, C., Jurcevich, B., Kushner, G., Levay, M., Lites, B., Elmore, D., Matsushita, T., Kawaguchi, N., Saito, H., Mikami, I., Hill, I. D., and Owens, J. K. (2008). The solar optical telescope for the hinode mission: an overview. *Solar Physics*, 249:167–196.

Tziotziou, K., Georgoulis, M. K., and Liu, Y. (2013). Interpreting eruptive behavior in noaa ar 11158 via the region's magnetic energy and relative helicity budgets. *The Astrophysical Journal*, 772(115):18pp.

Valori, G., Kliem, B., and R, K. (2005). Extrapolation of a nonlinear force-free field containing a highly twisted magnetic loop. *Astronomy and Astrophysics*, 433:335–347.

van Ballegooijen, A. A. (2004). Observations and modeling of a filament on the sun. *The Astrophysical Journal*, 612(1):519–529.

van Ballegooijen, A. A. and Martens, P. C. H. (1989). Formation and eruption of solar prominences. *The Astrophysical Journal*, 343:971–984.

van Tend, W. and Kuperus, M. (1978). The development of coronal electric current systems in active regions and their relation to filaments and flares. *Solar Physics*, 59:115–127.

Verma, M. (2018). The origin of two x-class flares in active region noaa 12673. *Astronomy and Astrophysics*, 612:A101.

Veronig, A., Temmer, M., Hanslmeir, A., Otruba, W., and Messerotti, M. (2002). Temporal aspects and frequency distributions of solar soft x-ray flares. *Astronomy and Astrophysics*, 382:1070–1080.

Wang, H., Jing, J., Tan, C., Wiegelmann, T., and Kubo, M. (2008). Study of magnetic channel structure in active region 10930. *The Astrophysical Journal*, 687:658.

Wang, H., Liu, C., Ahn, K., Xu, Y., Jing, J., Deng, N., Huang, N., Liu, R., Kusano, K., Fleishman, G. D., Gary, D. E., and Cao, W. (2017). High-resolution observations of flare precursors in the low solar atmosphere. *Nature Astronomy*, 1(85).

Wang, J. and Shi, Z. (1993). The flare-associated magnetic changes in an active region. *Solar Physics*, 143:119–139.

Wang, S., Liu, C., Liu, R., Deng, N., Liu, Y., and Wang, H. (2012). Response of the photospheric magnetic field to the x2.2 flare on 2011 february 15. *The Astrophysical Journal Letters*, 745(L17):5pp.

Wang, T., Su, A., and Zhang, H. (1994). Evolution of vector magnetic fields and vertical currents and their relationship with solar flares in ar 5747. *Solar Physics*, 155:99–112.

Wang, T., Yan, Y., Wang, J., Kurokawa, H., and Shibata, K. (2002). The large-scale coronal field structure and source regon features for a halo coronal mass ejection. *The Astrophysical Journal*, 572:572–597.

Warwick, J. W. (1962). The source of solar flares. *Publications of the Astronomical Society of the Pacific*, 74(439):302.

Wheatland, M. S. and Melrose, D. B. (1995). Interpreting yohkoh hard and soft x-ray flare observations. *Solar Physics*, 158(2):283–299.

Wheatland, M. S. and Régnier, S. (2009). A self-consistent nonlinear force-free solution for a solar active region magnetic field. *The Astrophysical Journal*, 700:L88–L91.

Wheatland, M. S., Sturrock, P. A., and Roumeliotis, G. (2000). An optimization approach to reconstructing force-free fields. *The Astrophysical Journal*, 540:1150–1155.

Wiegelmann, T. and Inhester, B. (2010). How to deal with measurement errors and lacking data in nonlinear force-free coronal magnetic field modelling? *Astronomy and Astrophysics*, 516(A107):5pp.

Wiegelmann, T. and Sakurai, T. (2012). Solar force-free magnetic fields. *Living Reviews of Solar Physics*, 9(5).

Woods, M. M., Inoue, S., Harra, L. K., Mathews, S. A., Kusano, K., and Kalmoni, N. M. E. (2018). The triggering of the 2014 march 29 filament eruption. *The Astrophysical Journal*, 860(163):10pp.

Wu, S. T., Sun, M. T., Chang, H. M., Hagyard, M. J., and Gary, G. A. (1989). On the numerical computation of nonlinear force-free magnetic fields. *The Astrophysical Journal*, 362:698–708.

Wyper, P. F., Antiochos, S. K., and DeVore, C. R. (2017). A universal model for solar eruptions. *Nature*, 544:452–455.

Xue, Z., Yan, X., Yang, L., Wang, J., and Zhao, L. (2017). Observing formation of flux rope by tether-cutting reconnection in the sun. *The Astrophysical Journal Letters*, 840(L23):8pp.

Yan, X. L., Yang, L. H., Xue, Z. K., Mei, Z. X., Kong, D. F., Wang, J. C., and Li, Q. L. (2018). Simultaneous observation of a flux rope eruption and magnetic reconnection during an x-class solar flare. *The Astrophysical Journal Letters*, 853(L18):7pp.

Yang, S., Zhang, J., Zhu, X., and Song, Q. (2017). Block-induced complex structures building the flare-productive solar active region 12673. *The Astrophysical Journal Letters*, 849(L21):7pp.

Yang, W. H., Sturrock, P. A., and Antiochos, S. K. (1986). Force-free magnetic fields: The magneto-frictional method. *The Astroophysical Journal*, 309:383–391.

Yokoyama, T., Akita, K., Morimoto, T., Inoue, K., and Newmark, J. (2001). Clear evidence of reconnection inflow of a solar flare. *The Astrophysical Journal*, 546:L69–L72.

Yokoyama, T. and Shibata, K. (1998). A two-dimensional magnetohydrodynamic simulation of chromospheric evaporation in a solar flare based on a magnetic reconnection model. *The Astrophysical Journal*, 494:L113–L116.

Zhao, J., Li, H., Pariat, E., Schmieder, B., Guo, Y., and Wiegelmann, T. (2014). Temporal evolution of the magnetic topology of the noaa active region 11158. *The Astrophysical Journal*, 787(88):12pp.

Zuccarello, F. P., Aulanier, G., and Gilchrist, S. A. (2016). The apparent critical decay index at the onset of solar prominence eruptions. *The Astrophysical Journal Letters*, 821(L23):6pp.

Zuccarello, F. P., Seaton, D. B., Mierla, M., Poedts, S., Rachmeler, L. A., Romano, P., and Zuccarello, F. (2014). Observational evidence of torus instability as trigger mechanism for coronal mass ejections: The 2011 august 4 filament eruption. *The Astrophysical Journal*, 785(88):11pp.